University of Liège - School of Engineering and Computer Science

Simulation of the domain-wall structure in magnetic thin films with perpendicular anisotropy

Author:
Bob Vermeulen

Supervisors:
Dr. Ir. Cédric Gommes
Prof. Dr. Thomas Brückel

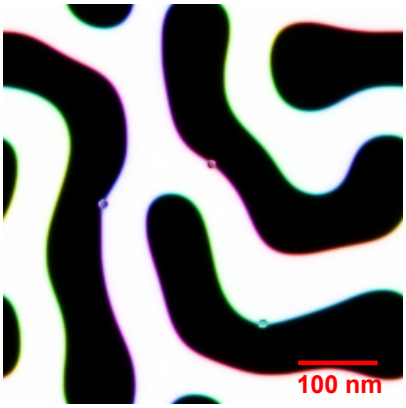

Master's thesis carried out to obtain the degree of
Master of Science in Engineering Physics by Vermeulen Bob

Academic year 2020 - 2021

Acknowledgments

This work would not have been possible without a number of people that contributed with their guidance, advice, knowledge and support.

First, I would like to thank **Prof. Dr. Thomas Brückel** for accepting me at the Jülich Center for Neutron Science 2 (JCNS-2) of the Forschungszentrum Jülich. In addition to enabling me to learn about magnetism and neutron scattering, it was an opportunity to gain insight into how research is performed in a large research center.

I would like to express my gratitude to **Dr. Cédric Gommes** and **Dr. Emmanuel Kentzinger** who supervised me during this semester. Your guidance and advice were of great help and both of you were perfectly complementary in this task. Even in these unusual times of Covid lockdown, I never felt alone during this project.

Next, I would like to thank the members of the Jury, **Prof. Dr. Thomas Brückel**, **Dr. Cédric Gommes**, **Prof. Dr. Benoît Vanderheyden** and **Prof. Dr. Alejandro Silhanek** for reviewing this thesis and showing interest in my work.

Special thanks go to **Dr. Annika Stellhorn** for your valuable advice, for the helpful explanations regarding your PhD thesis, for sharing the data of your measurements and for participating in the weekly meetings with Cédric and Emmanuel. I also thank the members of the **thin film group** of JCNS-2 for the interesting discussions every week about the research conducted in the institute.

Many thanks go to **Dr. Paul Baumeister** and **Alexander Clausen** for giving me access to the supercomputers JUSUF and JUWELS of the Jülich Supercomputing Center (JSC), and for your time when helping me to connect to the clusters. Not even a fraction of this work could have been done without such access. I also thank **Prof. Dr. Maarten Arnst** for giving me access to a GPU at the University of Liège.

Finally, to **my parents and brothers** for your support during this semester, during my studies and in my life in general.

Abstract

The emerging field of spintronics offers the prospect of lower power consumption and higher performances for future technologies. Materials with perpendicular magnetic anisotropy (PMA), like FePd, are promising candidates to be used in spintronic devices. Research on this type of materials includes the study of the magnetic configuration in thin films, how it can be controlled and how it switches. Micromagnetic simulations enable one to support experimental results and to understand the underlying physics. For these reasons, this thesis is a study of the domain-wall structure and the reversal mechanisms in FePd thin films, by means of micromagnetic simulations.

Above a certain critical thickness, the PMA induces the formation of out-of-plane-oriented magnetic domains, separated by domain walls (DWs). We show that the DWs are of Bloch type in the middle of the thickness, where the magnetization rotates in planes parallel to the plane of the DW. On the top and bottom surfaces, Néel closure domains are formed, where the magnetization rotates in a plane perpendicular to the wall.

The hysteresis and reversal mechanisms with an in-plane (IP) and an out-of-plane (OOP) applied field are then investigated. We show that defects are central in the reversal mechanisms and must therefore be included in the simulations. During the IP reversal, a stripe pattern is formed whereas, during the OOP reversal, reverse domains nucleate at the defects and grow to form a maze (or labyrinth-like) pattern. The obtained hysteresis curves are closed to experimental measurements.

Finally, the handedness (or chirality) of the Bloch walls is considered. Available neutron scattering measurements suggest a preferred handedness. A *Python* code is written to compute the neutron scattering patterns for the configurations obtained by micromagnetic simulations. It confirms the interpretation of the experimental measurements in terms of chirality. We show that the observed chirality is not likely to be the result of statistical fluctuations of a non-chiral system where left and right-handed DWs would have equal probabilities. We show that the handedness of the Bloch walls can be controlled with a weak chiral interaction like the Dzyaloshinskii-Moriya interaction (DMI). This is however not a proof that DMI exists in FePd thin films. The physical origin of the observed chirality suggests interesting research for the future.

Contents

Chapter 1

Introduction

1.1 Motivations

1.1.1 Spintronics

Magnetic materials for logic and memory applications have been studied since the 1950s [1]. The hard disk drive (HDD), using the direction of the magnetization to store information, was indeed invented in 1956 by IBM. The development of the transistor by the Bell laboratory in 1947 and the success of Si-based devices however prevented the further development of logic and memory devices based on magnetic materials. Nevertheless, the size scaling of electronic devices based on semiconductors is reaching its limits due to the fundamental limit of the atomic size. This leaves space for the development of devices based on other physical principles, and more precisely the field of spintronics. Spintronic devices use the spin of electrons and/or holes as additional degree of freedom. They have a promising future as they could reduce power consumption and increase memory and processing capabilities.

The discovery of tunneling magnetoresistance (TMR) in 1975 [2] enabled the development of magnetic tunnel junctions (MTJ) that act as a magnetic field sensor. TMR is observed when two ferromagnetic layers are separated by a thin insulating layer. Electrons can cross the insulating layer by tunneling, with a higher probability when the magnetization in the ferromagnetic layers is parallel than when it is antiparallel. In 1988, Albert Fert [3] and Peter Grünberg [4] discovered the giant magnetoresistance effect (GMR). It is observed when two ferromagnetic layers are separated by a non-magnetic, conducting layer. In this case also, the resistance is lower when the magnetization in both layers is parallel. By fixing the magnetization in one layer, and with the magnetization in the other layer that depends on the external magnetic field, TMR and GMR can be used as magnetic field sensor. Those effects have been used in several applications, like for example the read heads in HDDs.

Magnetic materials that possess perpendicular magnetic anisotropy (PMA) are essential for the development of MTJs [5]. A thin film with PMA presents an easy axis for the magnetization in the direction perpendicular to the film. The magnetization therefore lies either in the upward or downward direction. This enables one to store information in the direction of the magnetization and to perform logic operations. Those types of magnetic memories, like Magnetoresistive Random Access Memory (MRAM), have the advantage of being non-volatile and fast-switching.

Magnetic thin films with PMA usually exhibit magnetic domains with the magnetization either upwards or downwards. Those domains are separated by domain walls (DWs) where the magnetization gradually rotates from upwards to downwards and inversely. Those DWs have the property to scatter electrons, hence increasing the resistance in the plane of the film. This type of magnetoresistance is called domain-wall magnetoresistance (DWMR) [6]. Moreover, adding a superconducting layer on top of a magnetic layer with a domain pattern enables one to tailor the superconducting states due to the stray field of the magnetic layer [7].

FePd is a magnetic material exhibiting PMA and is a promising candidate for applications in spintronics. It is therefore important to study the precise structure of the domains and the domain walls in FePd thin films, which is the main focus of this thesis. Even though this thesis focuses on FePd thin films, the results can be extended to any magnetic thin film with PMA.

1.1.2 FePd thin films

FePd thin films with different degrees of perpendicular magnetic anisotropy (PMA) have been studied in the PhD thesis of Annika Stellhorn [8]. Depending on the strength of the PMA and the applied magnetic field, different patterns formed by the magnetic domains are observed. Typical patterns are the stripe pattern and the maze (or labyrinth) pattern, as shown in Fig. 1.1.

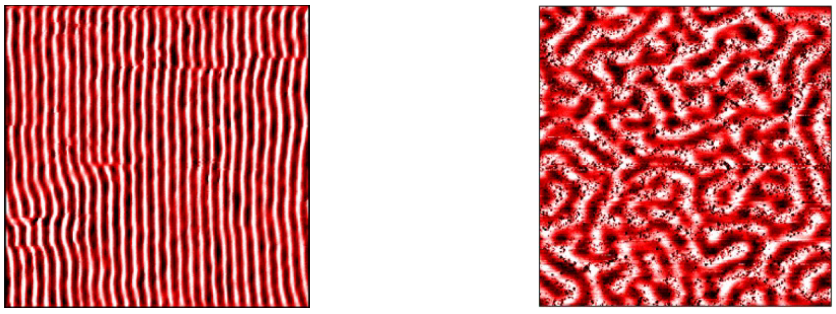

(a) Stripe pattern. **(b)** Maze pattern.

Figure 1.1: 3μm $\times$ 3μm Magnetic Force Microscopy (MFM) top view image of a sample with a stripe pattern (a) and a sample with a maze pattern (b). From A. Stellhorn [8].

A model for the structure of the domain walls separating the out-of-plane domains has been proposed in [8] and is sketched in Fig. 1.2. In the middle of the thickness, the magnetization rotates gradually between two adjacent domains, forming a Bloch-type wall. On the top and bottom surfaces, triangular domains are formed, called Néel closure domains.

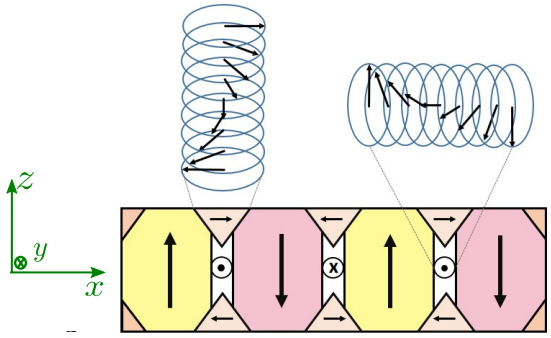

Figure 1.2: Sketch of a the cross section of a thin film with out-of-plane domains separated by Bloch domain walls and Néels closure domains at the surfaces. Figure adapted from [8].

Neutron scattering measurement performed in [8] suggest that there exists a preferred rotation direction for the magnetization in the Bloch walls. The origin of this preferred handedness, or chirality, is unclear yet.

Experimental research is crucial to observe how real magnetic materials behave. In parallel, micromagnetic simulations provide support to experimental measurements and enable one to understand the underlying physics. This thesis is therefore a study of the magnetic configuration in FePd thin films with PMA, by means of micromagnetic simulations, with 3 main goals formulated in the next section. Most of the results obtained by simulations are compared to experimental measurements to be validated.

1.2 Goals

This thesis has 3 main goals that are formulated as follows.

Goal 1: study the domain-wall structure.
The first goal is to perform an extensive study of the structure of the domain walls between the out-of-plane domains.

Goal 2: understand the hysteresis and reversal mechanisms.
The second goal is to determine and understand the mechanisms by which the magnetization switches from the saturated state in one direction to the saturated state in the other direction due to an external applied field, and how this is translated in hysteresis measurements. Understanding the reversal mechanisms is crucial since it determines the switching process in memory and logic applications. Both the case of an in-plane and an out-of-plane applied field are considered.

Goal 3: interpret neutron scattering measurements in terms of chirality of the domain walls.
The third goal is to understand how neutron scattering measurements can give information on the chirality of the domain walls and interpret correctly the existing measurements performed on FePd thin films.

1.3 Outline

The outline of this thesis addresses the 3 goals successively.

First, the main concepts and assumptions of magnetism and micromagnetic simulations are presented in **Chapter 2**.

Then, in **Chapter 3**, the magnetic and structural properties of FePd thin films are presented, as well as real measurements performed in the PhD thesis of Annika Stellhorn [8]. The parameters that will be used in all the simulations for FePd are given in this chapter.

In **Chapter 4**, the first goal is addressed. We start by determining the thickness below which the magnetization lies in the plane of the film, as a function of the strength of the PMA. Above this thickness, it is expected to observe out-of-plane magnetic domains. The structure of the domain walls is then studied in detail, depending on the thickness and the strength of the PMA.

Chapter 5 focuses on the second goal. The reversal mechanisms for an in-plane and out-of-plane applied field are determined, and the corresponding hysteresis curves are compared to experimental measurements to certify the results.

Finally, the third goal is addressed in **Chapter 6**. Experimental measurements of Grazing-Incidence Small-Angle Neutron Scattering (GISANS) are presented. A *Python* code is written to compute the Magnetic Small-Angle Neutron Scattering (MSANS) patterns for the configurations obtained by micromagnetic simulations. The results are qualitatively analyzed in terms of chirality of the domains walls.

The main conclusions of this thesis are given in **Chapter 7** as well as an outlook for future work.

Important remark
The input files for the simulations, the MSANS *Python* code and some animations are available on this clickable **link**. In Chapter 5, some figures have a clickable link in the caption to the corresponding animation. The links are always bold and in blue color, for example "**Vid01**". In case the links are broken, the following address may be copied in the browser:
https://iffcloud.fz-juelich.de/s/eyHJ72ta7w9Bbzw
The files can also be requested by email at:
b.vermeulen@fz-juelich.de

Chapter 2

Magnetism and micromagnetic simulations: main concepts and assumptions

2.1 Introduction

In this chapter, the important theoretical notions in magnetostatics and ferromagnetism used throughout the thesis are reminded. The micromagnetic theory is then introduced. Finally, the key concepts of micromagnetic simulations are presented and a simple example is studied.

2.2 Magnetostatics

2.2.1 Maxwell's equations

The fundamental equations of electromagnetism are Maxwell's equations, which can be written as

$$\nabla \times \mathbf{E} = -\frac{\partial \mathbf{B}}{\partial t}, \tag{2.1}$$

$$\nabla \times \mathbf{H} = \mathbf{j} + \frac{\partial \mathbf{D}}{\partial t}, \tag{2.2}$$

$$\nabla \cdot \mathbf{D} = \rho_{\mathrm{f}}, \tag{2.3}$$

$$\nabla \cdot \mathbf{B} = 0 \tag{2.4}$$

where

- $\mathbf{E}$ is the electric field in [V/m],
- $\mathbf{D}$ is the electric displacement in [C/m^2],

- $\mathbf{B}$ is the magnetic flux density or magnetic induction in [T],
- $\mathbf{H}$ is the magnetic field in [A/m],
- $\mathbf{j}$ is the current density in [A/m^2],
- and ρ_f is the free electric charge density in [C/m^3].

Magnetostatics correspond to the case where there is no time dependence. Using the equation of conservation of electric charge $\nabla \cdot \mathbf{j} = -\partial\rho_\mathrm{f}/\partial t$, the three equations left to describe magnetostatics are

$$\nabla \cdot \mathbf{j} = 0, \quad \nabla \cdot \mathbf{B} = 0 \quad \text{and} \quad \nabla \times \mathbf{H} = \mathbf{j}. \tag{2.5}$$

In order to solve physical problems, constitutive relations of the form $\mathbf{B} = \mathbf{B}(\mathbf{H})$ must be added to take into account the response of the materials to the fields and to close the set of equations. For ferromagnetic materials, the relation between $\mathbf{B}$ and $\mathbf{H}$ is not a one-to-one relation. It depends on the history of $\mathbf{H}$. This results in some hysteresis, as discussed in Section 2.4.3.

2.2.2 B, H and M

Writing Maxwell's equations in terms of the fundamental fields ($\mathbf{E}$ and $\mathbf{B}$) and the auxiliary fields ($\mathbf{D}$ and $\mathbf{H}$) enables one to have a set of equations valid for any medium, without introducing material properties or physical constants. The magnetic fields $\mathbf{B}$ and $\mathbf{H}$ are linked by

$$\mathbf{B} = \mu_0(\mathbf{H} + \mathbf{M}) \tag{2.6}$$

where the constant $\mu_0 = 4\pi\ 10^{-7}$ [T m A^{-1}] is the magnetic permeability of vacuum and $\mathbf{M}$ is the magnetization in [A/m].

The magnetization $\mathbf{M}$ is the magnetic moment $\boldsymbol{\mu}$ per unit volume. The magnetic moment of a free atom results from the spin of the electrons, the moment associated with their orbital angular momentum around the nucleus and possibly the spin of the nucleus itself. Nevertheless, the contribution from the nucleus can be neglected because it is three orders of magnitude smaller than the moment associated with the electrons [9]. A change of the orbital angular momentum of the electrons induced by an applied field can also result in an atomic magnetic moment (diamagnetic contribution).

In magnetostatics, the magnetization is defined as a mesoscopic average of the magnetic moment over a few nanometers (much larger than the inter-atomic distance) and a few microseconds (much larger than the fluctuations characteristic time), such that $\delta\boldsymbol{\mu} = \mathbf{M}\delta V$ with $\delta\boldsymbol{\mu}$ the time-averaged magnetic moment in a mesoscopic volume δV [10]. The magnetization $\mathbf{M}(\mathbf{r})$ is then a smoothly varying function. This is called

the continuous medium approximation.

The magnetic flux density $\mathbf{B}$ is a divergenceless (or solenoidal) field ($\nabla \cdot \mathbf{B} = 0$). This implies that the flux lines of $\mathbf{B}$ are closed loops and that we cannot associate $\mathbf{B}$ with a magnetic charge from where flux lines would diverge. On the contrary, the magnetic field $\mathbf{H}$ is not divergenceless. Indeed, from $\nabla \cdot \mathbf{B} = 0$ and Eq. 2.6, we can write

$$\nabla \cdot \mathbf{H} = -\nabla \cdot \mathbf{M}. \tag{2.7}$$

A non-uniform magnetization can therefore act as sources and sinks for $\mathbf{H}$, or positive and negative magnetic charges. One can define a magnetic charge density in the bulk as $\rho_{\mathrm{m}} = -\nabla \cdot \mathbf{M}$ and at the surface as $\sigma_{\mathrm{m}} = \mathbf{M} \cdot \mathbf{e}_{\mathrm{n}}$ with $\mathbf{e}_{\mathrm{n}}$ the outside normal [10]. In the static case, $\mathbf{H}$ can therefore result from a current density $\mathbf{j}$ and from the magnetization distribution in other magnets or in the magnet itself, so that

$$\mathbf{H} = \mathbf{H}_{\mathrm{c}} + \mathbf{H}_{\mathrm{m}}, \tag{2.8}$$

where the current contribution and the magnetization contribution are written $\mathbf{H}_{\mathrm{c}}$ and $\mathbf{H}_{\mathrm{m}}$ respectively. The part of $\mathbf{H}_{\mathrm{m}}$ which is due to the magnetization distribution of the considered magnet is denoted $\mathbf{H}_{\mathrm{d}}$ (called the stray field outside the magnet and the demagnetizing field inside the magnet). The fields $\mathbf{B}$, $\mathbf{H}$ and $\mathbf{M}$ for a uniformly magnetized material without external applied field are represented in Fig. 2.1. Magnetic charges are present at the top and bottom surfaces, producing an $\mathbf{H}$ field opposite to $\mathbf{M}$ inside the magnet, hence the name demagnetizing field. Outside the magnet, where $\mathbf{M} = 0$, the $\mathbf{B}$ field is simply $\mu_0 \mathbf{H}$.

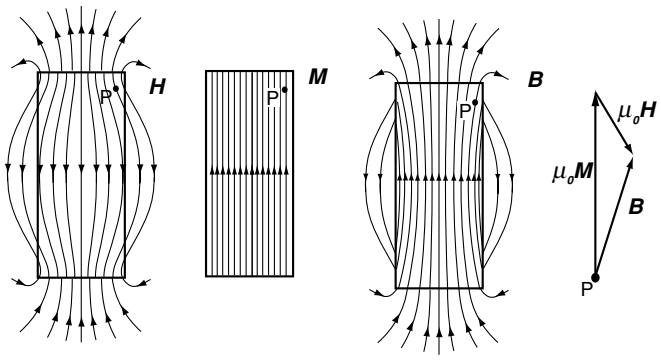

Figure 2.1: Illustration of the $\mathbf{H}$, $\mathbf{M}$ and $\mathbf{B}$ fields for a uniformly magnetized block without external applied field. The relation between them (Eq. 2.6) is sketched at a point P. Figure taken from [10].

In a uniformly magnetized sample having the form of an ellipsoid, the demagnetizing

field is also uniform and can be written as

$$\mathbf{H}_\mathrm{d} = -\boldsymbol{\mathcal{N}}\mathbf{M} \tag{2.9}$$

where $\boldsymbol{\mathcal{N}}$ is the demagnetizing tensor [10]. In the case of a thin film, denoting x and y the in-plane directions and z the out-of-plane direction, the demagnetizing tensor becomes diagonal with $\mathcal{N}_x = \mathcal{N}_y = 0$ and $\mathcal{N}_z = 1$. Indeed, when the magnetization lies in the out-of-plane direction, magnetic charges are created at the top and bottom surfaces, resulting in a demagnetizing field opposite to $\mathbf{M}$.

2.2.3 Internal and external fields

When an external field $\mathbf{H}_\mathrm{ext}$ produced by a magnet or an electric current is applied to a sample, the internal field $\mathbf{H}$ is given by

$$\mathbf{H} = \mathbf{H}_\mathrm{ext} + \mathbf{H}_\mathrm{d}, \tag{2.10}$$

i.e. the sum of the applied field $\mathbf{H}_\mathrm{ext}$ and the demagnetizing field $\mathbf{H}_\mathrm{d}$ produced by the magnetization distribution of the sample itself, which is unknown in general. When performing measurements to deduce $\mathbf{M}(\mathbf{H})$, one can approximate $\mathbf{H}$ using the demagnetizing tensor or use a geometry where there is no demagnetizing field like in a toroid. One can also plot the relation $\mathbf{M} = \mathbf{M}(\mathbf{H}_\mathrm{ext})$ without having to approximate $\mathbf{H}_\mathrm{d}$. In this case however, the result will not only depend on the material itself, but also on the geometry of the sample. When showing an hysteresis loop of $\mathbf{B}$ or $\mathbf{M}$ versus the $\mathbf{H}$ field, it is therefore important to clearly specify if the real $\mathbf{H}$ field is plotted or only the applied field $\mathbf{H}_\mathrm{ext}$.

2.2.4 Magnetostatic energy

As will be explained in Section 2.4 in the framework of the micromagnetic theory, the equilibrium magnetic configuration of a sample is given by the minimum of the total free energy. Let us therefore introduce here the energy contributions due to magnetostatic effects, namely the self-energy of a body (associated with its demagnetizing field) and the energy associated with an external field.

A magnetic dipole in a field $\mathbf{B}$ experiences a torque $\boldsymbol{\Gamma} = \boldsymbol{\mu} \times \mathbf{B}$ and one can define the Zeeman energy $E_\mathrm{m} = -\boldsymbol{\mu} \cdot \mathbf{B}$. If we consider two dipoles, this energy becomes $E_\mathrm{m} = -\boldsymbol{\mu}_1 \cdot \mathbf{B}_{21} = -\boldsymbol{\mu}_2 \cdot \mathbf{B}_{12} = -\frac{1}{2}(\boldsymbol{\mu}_1 \cdot \mathbf{B}_{21} + \boldsymbol{\mu}_2 \cdot \mathbf{B}_{12})$ where $\mathbf{B}_{12}$ is the field produced by the dipole 1 at the position of the dipole 2, and inversely for $\mathbf{B}_{21}$. This energy is the reason why free dipoles tend to aggregate in treads. This dipole-dipole interaction energy can be generalized to the case of a solid without external field to obtain the

self-energy energy E_d (also called demagnetizing energy or dipolar energy). One can show that it is given by [10]

$$E_\mathrm{d} = -\frac{1}{2}\int_V \mu_0 \mathbf{H}_\mathrm{d} \cdot \mathbf{M}\, \mathrm{d}^3 r \tag{2.11}$$

where V is the volume of the sample. Using $\mathbf{M} = \mathbf{B}/\mu_0 - \mathbf{H}_\mathrm{d}$ and the result $\int \mathbf{B} \cdot \mathbf{H}_\mathrm{d}\, \mathrm{d}^3 r = 0$ for a magnet in its own field without currents [10], we have

$$E_\mathrm{d} = \frac{1}{2}\int \mu_0 H_\mathrm{d}^2\, \mathrm{d}^3 r \tag{2.12}$$

where the integral is over all space. This expression of the self-energy shows that the magnetization tends to adopt a configuration that minimizes the demagnetization field. In the case of a thin film, the magnetization therefore tends to lie in the plane of the film.

Then, when an external field $\mathbf{H}_\mathrm{ext}$ is applied, one needs to add the Zeeman energy

$$E_\mathrm{Z} = -\int_V \mu_0 \mathbf{H}_\mathrm{ext} \cdot \mathbf{M}\, \mathrm{d}^3 r \tag{2.13}$$

to obtain the full magnetostatic energy $E_\mathrm{d} + E_\mathrm{Z}$.

2.2.5 System of units

In magnetism, two main systems of units are currently used: the centimeter-gram-second System of Units (CGS) and the International System of Units (SI) (meter-kg-second-Ampère). The first one is used a lot in textbooks and scientific literature because it simplifies the writing of the equations. However, only the SI will be used throughout this thesis for the two reasons given in Appendix A, together with a conversion table for the relevant physical quantities.

2.3 Ferromagnetism

2.3.1 Ferromagnetic order

As explained in Section 2.2, some atoms have a non-zero magnetic moment $\boldsymbol{\mu}$. A ferromagnet is a material that has a spontaneous average magnetic moment (*i.e.* even in zero applied field) resulting from the regular arrangement of the magnetic moments of the atoms the material is made of. Above the Curie temperature T_C, thermal agitation suppresses this ordering and the material has no net magnetic moment. This is the disordered paramagnetic phase. Below T_C, in the ordered ferromagnetic phase,

the atomic magnetic moments tend to align, giving rise to a spontaneous magnetization M_s. The interaction that tends to align the atomic moments is called the exchange interaction.

Ferromagnetism can be explained from the Pauli exclusion principle and the Coulomb interaction [11]. Ferromagnetic atoms have partially filled valence subshells. In these atoms, the spins of the electrons tend to be parallel, to the extent allowed by the Pauli principle. Indeed, when the spins are parallel, the electrons are farther apart due to the diplole-dipole interaction, which reduces the Coulomb energy. This results in a nonzero magnetic moment for the atom. When adjacent atoms are close enough, the wavefunctions of the electrons in the valence subshells overlap. The electrons of different atoms then also tend to align their spin, giving rise to the so-called exchange interaction. The interaction energy between two atoms i and j carrying electron spins $\mathbf{S}_i$ and $\mathbf{S}_j$ is represented by the Heisenberg Hamiltonian [9]

$$\mathcal{H}_{\text{Heisenberg}} = -2J_{ij}\mathbf{S}_i \cdot \mathbf{S}_j \tag{2.14}$$

where J_{ij} is the exchange integral and is linked to the overlap of the electronic distributions of the two atoms. For a ferromagnetic material, $J_{ij} > 0$ between two adjacent atoms such that the spins tend to align.

Some materials with a lack of inversion symmetry can exhibit a weak antisymmetric coupling called the Dzyaloshinskii-Moriya interaction (DMI) [12, 13]. This interaction is represented by the Hamiltonian [10]

$$\mathcal{H}_{\text{DMI}} = -\mathbf{D}_{ij} \cdot (\mathbf{S}_i \times \mathbf{S}_j) \tag{2.15}$$

where $\mathbf{D}_{ij}$ is a vector. This weak interaction tends to couple spins perpendicularly and can induce chiral magnetic structures such as skyrmions.

2.3.2 Anisotropy

Magnetic anisotropy refers to the case where there exists some preferred direction for the magnetization, colloquially referred to as an easy axis. The three main types of anisotropy are the shape anisotropy, the magnetocrytalline anisotropy and the induced anisotropy [10].

Shape anisotropy is caused by the demagnetizing energy E_d (Eq. 2.11) which is due to the interaction between the magnetization and the demagnetizing field resulting from the shape of the sample. The direction of magnetization that minimizes the demagnetizing field is favored. Magnetocrystalline anisotropy is an intrinsic property

(*i.e.* not related to the shape of the sample) originating from the crystal structure. Finally, induced anisotropy corresponds to the creation of an easy axis by applying a mechanical stress or by annealing an alloy under a magnetic field.

2.4 Micromagnetism

The main assumption of micromagnetism is the continuous medium approximation. The magnetization $\mathbf{M}(\mathbf{r})$ is considered as a mesoscopic average that varies smoothly in space, ignoring the atomic structures, and with a constant magnitude equal to the spontaneous magnetization M_s. This enables one to have a convenient framework to compute the total free energy and compute the magnetization configuration by energy minimization. Magnetization dynamics can also be described.

2.4.1 Micromagnetic energy

In micromagnetism, the total free energy is given by [10]

$$E_\mathrm{tot} = E_\mathrm{ex} + E_\mathrm{a} + E_\mathrm{d} + E_\mathrm{Z}. \tag{2.16}$$

The first term is the exchange energy given by

$$E_\mathrm{ex} = \int_V A \left(\frac{\nabla \mathbf{M}}{M_\mathrm{s}}\right)^2 \mathrm{d}^3 r = \int_V A \left[\left(\frac{\nabla M_x}{M_\mathrm{s}}\right)^2 + \left(\frac{\nabla M_y}{M_\mathrm{s}}\right)^2 + \left(\frac{\nabla M_z}{M_\mathrm{s}}\right)^2\right] \mathrm{d}^3 r \tag{2.17}$$

with A the exchange stiffness in [J/m]. This energy is minimized when the magnetization is uniform, corresponding to the case where all the spins are parallel. The second term is the magnetocrystalline anisotropy energy. In the case of uniaxial anisotropy, it is computed as

$$E_\mathrm{a} = \int_V K_\mathrm{u} \sin^2 \theta \, \mathrm{d}^3 r \tag{2.18}$$

with K_u the anisotropy constant in [J/m^3] and θ the angle between the magnetization $\mathbf{M}$ and the easy axis $\mathbf{e}_\mathrm{u}$. The third term is the demagnetizing energy given by Eq. 2.11 and accounts for the shape anisotropy. The fourth term is the Zeeman energy due to an applied field given by Eq. 2.13.

Writing the expressions of the four terms, Eq. 2.16 becomes

$$E_\mathrm{tot} = \int_V \left[A \left(\frac{\nabla \mathbf{M}}{M_\mathrm{s}}\right)^2 + K_\mathrm{u} \sin^2 \theta - \frac{1}{2}\mu_0 \mathbf{M} \cdot \mathbf{H}_\mathrm{d} - \mu_0 \mathbf{M} \cdot \mathbf{H}_\mathrm{ext}\right] \mathrm{d}^3 r. \tag{2.19}$$

2.4.2 Magnetic domains and domain walls

If only the exchange and anisotropy energies were present, the magnetization would be uniform and parallel to the easy axis $\mathbf{e}_\mathrm{u}$. If one considers also the demagnetizing energy E_d, the total energy is decreased by creating domains of uniform magnetization in different directions to decrease the demagnetizing field, as illustrated in Fig. 2.2. In (a), magnetic charges are formed at the top and bottom surfaces, producing a large demagnetizing or stray field. By creating domains in (b) and (c), the demagnetizing energy is reduced. In (d) and (e), the demagnetizing energy is reduced to zero by adding triangular closure domains to avoid any magnetization component normal to the surface. Note that the walls of the closure domains making a 45° angle with the magnetization do not produce any magnetic charges either.

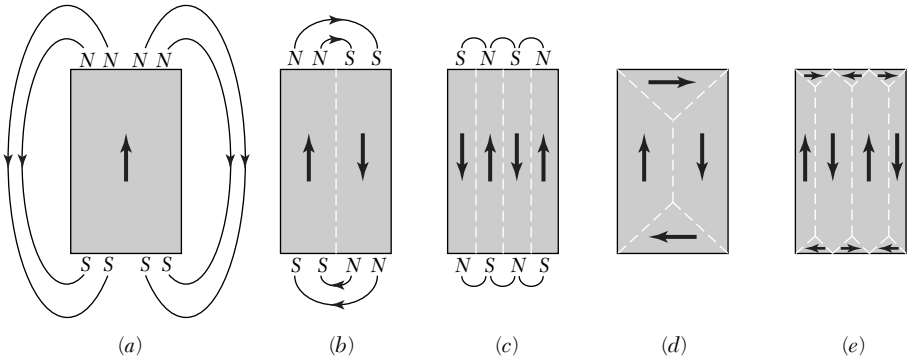

Figure 2.2: Illustration of the decrease of the demagnetizing energy by forming magnetic domains. Figure taken from [9].

Magnetic domains are separated by domain walls (DWs) in which the magnetization rotates. Two common types of domain walls are the Bloch wall and the Néel wall, illustrated in Fig. 2.3. In a Bloch wall, the magnetization rotates in planes parallel to the plane of the wall. This implies that $\nabla \cdot \mathbf{M} = 0$ and no magnetic charge is created in the bulk. In a Néel wall, the magnetization rotates in a plane perpendicular to the plane of the wall. In this case, $\nabla \cdot \mathbf{M} \neq 0$ and magnetic charges are created within the bulk.

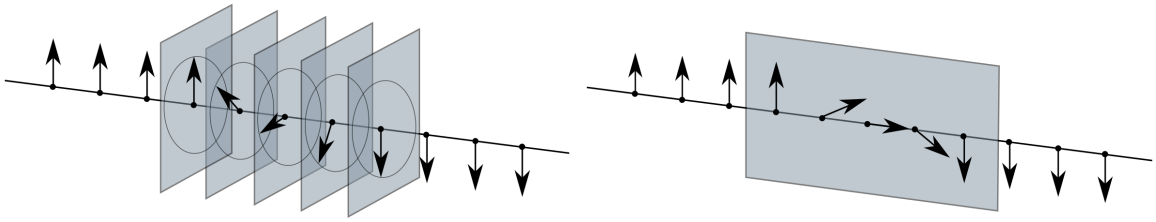

(a) Bloch wall. **(b)** Néel wall.

Figure 2.3: Illustration of the two main types of domain walls between domains with opposite magnetization. (a) In a Bloch wall, the magnetization rotates in planes parallel to the plane of the wall. (b) In a Néel wall, the magnetization rotates in a plane perpendicular to the plane of the wall.

When an external magnetic field $\mathbf{H}_{\text{ext}}$ is applied to a sample with magnetic domains, two main magnetization processes can be observed. The first one is domain wall motion resulting in the growth of the favorably-oriented domains at the expense of the unfavorably-oriented domains. The second one is magnetization rotation within a domain when it is not aligned with the applied field.

2.4.3 Reversal, pinning and nucleation

The hysteresis of $\mathbf{M}(\mathbf{H})$ that can be observed for ferromagnets depends on the reversal mechanisms to transit from the saturated configuration in one direction to the saturated configuration in the other direction. For single-domain particles, the three main mechanisms are coherent rotation of the magnetization, curling by passing through a vortex state or buckling which is a combination of the first two [10]. Reversal can also be achieved by the growth of reverse domains. Reverse domains can nucleate in the bulk at a defect or from spontaneous thermal fluctuations. They can also nucleate from surface asperities where there is a strong local demagnetizing field. Once a reverse domain has nucleated, it will grow through domain-wall motion. The propagation of the domain walls can be hindered by defects acting as pinning centers.

2.4.4 Coercivity and hysteresis

The hysteresis loops for ideal soft and hard spheres are shown in Fig. 2.4. Note that for a sphere, the demagnetizing tensor is $\boldsymbol{\mathcal{N}} = \frac{1}{3}\mathbf{I}$ with $\mathbf{I}$ the identity tensor. The curves for B instead of M can be retrieved using Eq. 2.6. For the ideal soft ferromagnet, there is no hysteresis whereas, for the ideal hard ferromagnet, the hysteresis is large. The value of H_{ext} at which $M = 0$ is called the coercivity H_{c}.
A general hysteresis loop is shown in Fig. 2.5, where the magnetization averaged over the sample is plotted. The nucleation field H_{n} is the field where the first deviation from

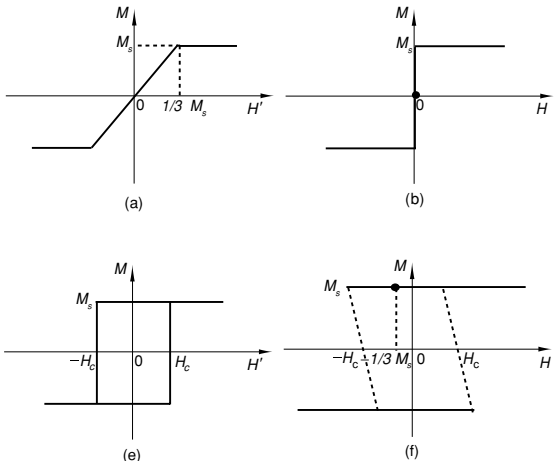

Figure 2.4: Hysteresis loops of the magnetization M versus the external field $H_{\text{ext}} = H'$ or the magnetic field H for ideal soft (a and b) and hard (e and f) ferromagnetic spheres. Figure taken from [10].

the saturation state is observed. The remanent magnetization M_{r} is the magnetization at zero applied field. For a macroscopic real sample, the hysteresis loop is made of a large number of discrete jumps, called Barkhausen jumps. These correspond to jumps of the domain walls in an energy landscape with multiple minimums shaped by the many defects that can act as pinning centers or nucleation centers.

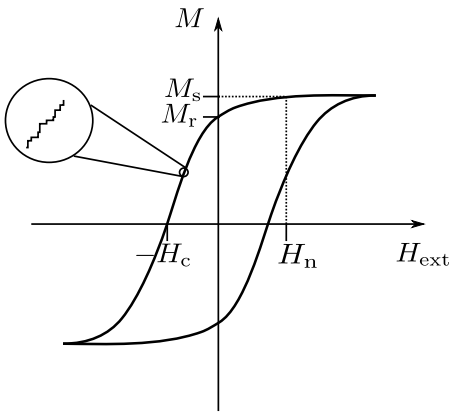

Figure 2.5: Illustration of a general M-H_{ext} hysteresis loop with the definitions of the remanent magnetization M_{r}, the coercive field H_{c} and the nucleation field H_{n}. The Barkhausen jumps are illustrated in the inset. Figure inspired from [10].

2.4.5 Dynamics

The micromagnetic energy enables one to compute equilibrium configurations by looking for local minimums without considering the dynamics. The dynamics of the

magnetization can be described by the Landau-Lifschitz-Gilbert equation [10]

$$\frac{\mathrm{d}\mathbf{M}}{\mathrm{d}t} = \gamma_0 \mu_0 \mathbf{M} \times \mathbf{H} - \frac{\alpha}{M_\mathrm{s}} \mathbf{M} \times \frac{\mathrm{d}\mathbf{M}}{\mathrm{d}t} \tag{2.20}$$

where γ_0 is the gyromagnetic ratio in $[\mathrm{T}^{-1}\,\mathrm{s}^{-1}]$ and α is a dimensionless damping coefficient. The first term accounts for the precession of the magnetization around the magnetic field and the second term accounts for the damping due to losses, enabling the magnetization to eventually align with the magnetic field.

2.5 Introduction to micromagnetic simulations

Micromagnetic simulations enable one to compute the equilibrium configurations of the magnetization as well as the dynamics. Several programs exist, differing by the discretization scheme, the numerical methods and the hardware. Space can be discretized using a finite-difference method or a finite-element method [14]. Finite-difference solvers compute average quantities in each cell and include *OOMMF* [15], *MuMax3* [16] and *FIDIMAG* [17]. Finite-element solvers, like *Magpar* [18], *Nmag* [19], *magnum.fe* [20] and *FastMag* [21], are based on the magnetic scalar potential (when $\nabla \times \mathbf{H} = 0$).

In this thesis, the GPU-accelerated finite-difference solver *MuMax3* is used. Let us therefore introduce the finite-difference method, compare *MuMax3* with the CPU-based software *OOMMF* and consider a first simple example.

2.5.1 Finite-difference method

In finite-difference micromagnetics, the simulation space is divided in a regular rectangular grid with N_x, N_y and N_z points in the x, y and z directions. The grid points correspond to the cell centers. The unknown is the dimensionless unit magnetization vector

$$\mathbf{m} = \frac{\mathbf{M}}{M_\mathrm{s}}, \quad \text{with } \|\mathbf{m}\| = 1, \tag{2.21}$$

at each grid point, indicating the direction of the magnetization. Volume quantities like the magnetization and the effective field are treated at the center of each cell (and considered constant within each cell). Coupling quantities like the exchange stiffness are considered at the faces between the cells [16].

The different energy terms of Eq. 2.19 can then be approximated by replacing the integral by a sum over all the grid points and by replacing the derivatives of $\mathbf{m}(\mathbf{r})$ with finite-difference quotients. The total energy can then be minimized using nu-

merical methods like the conjugate-gradient method or the steepest-descent method to obtain the equilibrium configuration.

When the dynamic response of a system is needed, the LLG equation under the form [22]

$$\frac{\partial \mathbf{m}}{\partial t} = -\frac{|\gamma_0|\mu_0}{1+\alpha^2}\left[\mathbf{m}\times\mathbf{H}_{\text{eff}} - \alpha\mathbf{m}\times(\mathbf{m}\times\mathbf{H}_{\text{eff}})\right] \tag{2.22}$$

can be used, with the effective field [22]

$$\mathbf{H}_{\text{eff}} = -\frac{1}{\mu_0 M_{\text{s}}}\frac{\delta E_{\text{tot}}}{\delta \mathbf{m}}. \tag{2.23}$$

The time integration of Eq. 2.22 can then be performed using a Runge-Kutta method.

The cell size should be chosen small enough to have an accurate numerical solution, but not too small to avoid excessively long computation times. To ensure accuracy, it is recommended to have a cell size smaller than the magnetostatic and the magnetocrystalline exchange lengths. The magnetostatic exchange length is defined by [23]

$$l_{\text{ex},M_{\text{s}}} = \sqrt{\frac{A}{\frac{1}{2}\mu_0 M_{\text{s}}^2}} \tag{2.24}$$

and characterizes the competition between the exchange energy E_{ex} and the dipolar energy E_{d}. The magnetocrystalline exchange length is defined by [23]

$$l_{\text{ex},K} = \sqrt{\frac{A}{K_{\text{u}}}} \tag{2.25}$$

and characterizes the competition between the exchange energy E_{ex} and the anisotropy energy E_{a}. The smallest of these two lengths gives a length scale on which the magnetization changes. The cell size should therefore be smaller than this length scale. Another good practice is to check the maximum angle between the magnetization of neighboring cells and make sure it is smaller than 30°.

2.5.2 Software and hardware used for this thesis

Two popular finite-difference micromagnetic simulation programs are *OOMMF* [15], developed at the National Institute of Standards and Technology (NIST) in the United States, and *MuMax3* [16], developed at Ghent University (Belgium). The main difference between the two is that *OOMMF* runs on one or multiple CPUs, whereas *MuMax3* is accelerated with a GPU. *MuMax3* has been chosen for all the simulations in this thesis because of its good performances and its ease of use.

Most of the simulations have been performed on two supercomputers from the Jülich Supercomputing Center (JSC). The first one, called JUSUF (Jülich Support for Fenix), contains 61 accelerated compute nodes, each equipped with an NVIDIA V100 GPU. The second one, called JUWELS (Jülich Wizard for European Leadership Science) [24], contains 936 nodes each equipped with 4 NVIDIA A100 GPUs. Some simulations have also been performed on a computer from the ULiège, called *treebeard*, equipped with an NVIDIA TITAN V GPU.

The solution in *MuMax3* can be computed with 3 different functions [16]. The *Minimize* function performs energy minimization using a steepest gradient algorithm. The *Run* function enables one to perform dynamic simulations by integrating the LLG equation. Finally, the *Relax* function is an alternative to *Minimize* to compute an equilibrium configuration. It integrates the LLG equation without the precession term, using only the damping term. This pseudo-dynamic algorithm is preferred for high-energy initial configurations, like a random magnetization, for which the energy minimization function may not converge. The pseudo-dynamic algorithm is therefore more robust, but it is considerably slower than energy minimization algorithm.

2.5.3 Dimensional analysis

Let us perform a brief dimensional analysis of the problem of interest of this thesis, in order to identify the key parameters to vary. The sample is considered to be a thin film with an infinite extension in the plane of the film. A length scale for this geometry is then simply given by the thickness d. Without an external applied field, the relevant energies are the exchange, the anisotropy and the demagnetizing energy. The total energy per unit volume is then given by

$$\frac{E_{\text{tot}}}{V} = \frac{1}{V}\int_V \left[A\left(\nabla \mathbf{m}\right)^2 + K_{\text{u}}\sin^2\theta - \frac{1}{2}\mu_0 M_{\text{s}}\mathbf{m}\cdot\mathbf{H}_{\text{d}}\right]\mathrm{d}^3 r \tag{2.26}$$

where $\mathbf{H}_{\text{d}}$ depends on the magnetization configuration and the geometry. The equilibrium configuration of $\mathbf{m}$ is found by minimizing this energy and therefore depends on the 5 independent variables listed in Table 2.1. Three independent units are involved: kg/s^2, m and A (or equivalently J, m, A). According to the Buckingham π theorem, the number of independent dimensionless groups that can be formed is $5 - 3 = 2$. A first dimensionless number can be given by the ratio of the thickness d over the magnetostatic exchange length

$$\frac{d}{l_{\text{ex},M_{\text{s}}}} = \frac{d}{\sqrt{\frac{A}{\frac{1}{2}\mu_0 M_{\text{s}}^2}}}. \tag{2.27}$$

A second dimensionless number can be given by the anisotropy quality factor [25]

$$Q = \frac{K_\mathrm{u}}{\frac{1}{2}\mu_0 M_\mathrm{s}^2} \tag{2.28}$$

characterizing the magnitude of E_a versus E_d. The only two interesting parameters to vary during the simulations are therefore $d/l_{\mathrm{ex},M_\mathrm{s}}$ (or $d/l_{\mathrm{ex},K}$) and Q. Applying an external magnetic field brings an additional parameter to vary.

Variables	**m**	A	K_u	μ_0	d	M_s
Units	1	$\frac{\mathrm{J}}{\mathrm{m}}$	$\frac{\mathrm{J}}{\mathrm{m}^3}$	$\frac{\mathrm{J}}{\mathrm{mA}^2}$	m	$\frac{\mathrm{A}}{\mathrm{m}}$
SI units	1	$\frac{\mathrm{kg}}{\mathrm{s}^2}\mathrm{m}$	$\frac{\mathrm{kg}}{\mathrm{s}^2\mathrm{m}}$	$\frac{\mathrm{kg}}{\mathrm{s}^2}\frac{\mathrm{m}}{\mathrm{A}^2}$	m	$\frac{\mathrm{A}}{\mathrm{m}}$

Table 2.1: Units of the different variables relevant for the magnetization configuration in a thin film.

The quality factor Q can be computed from the initial magnetization curves with an in-plane and an out-of-plane applied field using a basic thermodynamical reasoning [26, 27]. The work increment per unit volume to change the average magnetization by $\delta\mathbf{M}$ with an external field $\mathbf{H}_\mathrm{ext}$ is $\delta w = \mu_0 \mathbf{H}_\mathrm{ext} \cdot \delta\mathbf{M}$. The difference Δe in work per unit volume to magnetize the sample to saturation in-plane and out-of-plane is then given by

$$\Delta e = \int_0^{M_\mathrm{s}} \mu_0 H_\mathrm{ext}^\mathrm{ip} \mathrm{d}M^\mathrm{ip} - \int_0^{M_\mathrm{s}} \mu_0 H_\mathrm{ext}^\mathrm{oop} \mathrm{d}M^\mathrm{oop} = R \tag{2.29}$$

where R is used to denote the area between the in-plane (IP) and out-of-plane (OOP) magnetization curves. Assuming a reversible process, Δe also corresponds to the difference in energy between the IP and OOP saturated states. The energy density for the former is only due to the magnetocrystalline anisotropy since the demagnetizing field is zero in this case. It is therefore simply $e^\mathrm{ip} = K_\mathrm{u}$. The energy density for the OOP saturated state is only due to the demagnetizing field, which is equal to $H_\mathrm{d} = -M$ for a thin film. We therefore have $e^\mathrm{oop} = -\frac{1}{2}\mu_0 M H_\mathrm{d} = \frac{1}{2}\mu_0 M_\mathrm{s}^2$. Consequently, $\Delta e = e^\mathrm{ip} - e^\mathrm{oop} = K_\mathrm{u} - \frac{1}{2}\mu_0 M_\mathrm{s}^2$. Equating this to Eq. 2.29, we have

$$K_\mathrm{u} - \frac{1}{2}\mu_0 M_\mathrm{s}^2 = R \tag{2.30}$$

and the quality factor can be computed with

$$Q = \frac{K_\mathrm{u}}{\frac{1}{2}\mu_0 M_\mathrm{s}^2} = \frac{R}{\frac{1}{2}\mu_0 M_\mathrm{s}^2} + 1. \tag{2.31}$$

2.5.4 Simple case: the Bloch wall

Before performing complex simulations, let us first compute the magnetization configuration in a simple case for which an analytical solution is known. We consider a 180° Bloch wall between two domains with a magnetization in opposite directions. Denoting z the easy axis, assuming that the magnetization only depends on x and neglecting the demagnetizing field that could arise from the surface magnetic charges, the total energy (per unit surface) is

$$E_{\text{tot}} = E_{\text{ex}} + E_{\text{a}} = \int \left[A \left(\partial\theta/\partial x \right)^2 + K_{\text{u}} \sin^2 \theta \right] \mathrm{d}x \tag{2.32}$$

where θ is the angle between the magnetization and the easy axis z. The Bloch wall is between two domains with $\theta = 0$ and $\theta = \pi$. This energy is minimized for [10]

$$x = \sqrt{\frac{A}{K_{\text{u}}}} \ln \left[\tan(\theta/2) \right]. \tag{2.33}$$

Inverting this equation yields

$$\theta(x) = 2 \tan^{-1} \left[\exp \left(\frac{\pi x}{\delta_{\text{w}}} \right) \right] \tag{2.34}$$

where

$$\delta_{\text{w}} = \pi \sqrt{\frac{A}{K_{\text{u}}}}. \tag{2.35}$$

δ_{w} is the characteristic width of the Bloch wall, obtained from extrapolation of the tangent at the center of the wall. Replacing Eq. 2.34 into Eq. 2.32 yields the energy of a Bloch wall per unit area

$$\sigma_{\text{w}} = 4\sqrt{A K_{\text{u}}}. \tag{2.36}$$

This has been computed in *MuMax3* by considering only the exchange and anisotropy energies, with as initial configuration two domains with opposite magnetization. Since there is no demagnetizing energy, the only relevant exchange length here is the magnetocrystalline exchange length $l_{\text{ex},K}$. This is even more obvious when we look to Eq. 2.34 where we see that the profile only depends on $\delta_{\text{w}} = \pi\, l_{\text{ex},K}$. The equilibrium configuration is computed by energy minimization for several cell sizes Δx. The results for the total energy and the $\theta(x)$ profile are shown in Fig. 2.6. One can see that the simulated solution converges to the analytical solution for decreasing cell size Δx and that the solution is relatively accurate for $\Delta x < l_{\text{ex},K}$. For $\Delta x = 0.5\, l_{\text{ex},K}$, the maximum angle between neighboring cells is 30°.

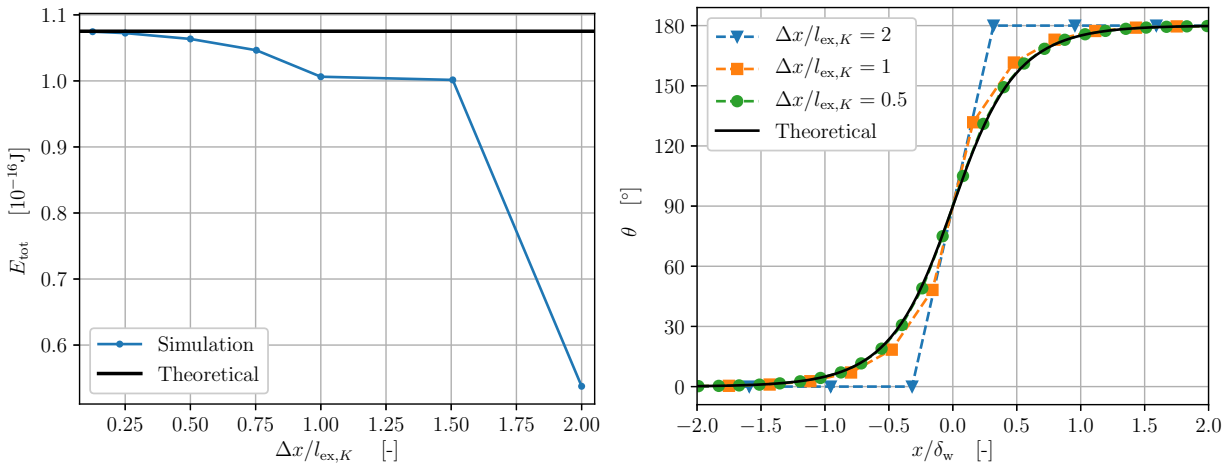

(a) **(b)**

Figure 2.6: Convergence of the numerical simulation for a Bloch wall: total energy (a) and $\theta(x)$ profile (b) for several values of the cell size Δx. Parameters of the simulation: $M_{\text{s}} = 10^6$ A/m, $A = 7\,10^{-12}$ J/m, $K_{\text{u}} = 1256637\,\text{J/m}^3$ with a $128 l_{\text{ex},K} \times 128 l_{\text{ex},K}$ simulation box of 30nm thickness.

2.6 Conclusion

This chapter gave the main concepts of magnetism used throughout this thesis. Two important remarks should be kept in mind. First, the demagnetizing field has a central role in the formation of domains. Second, micromagnetic simulations enable one to compute simple magnetic configurations provided that the cell size is smaller than the exchange lengths.

Chapter 3

FePd thin films: growth and characterization

3.1 Introduction

The simulations performed in this thesis aim to determine the structure of the domains and the domain walls in FePd thin films, and understand the underlying physics. Before that, let us give in this chapter a short introduction on FePd thin films. We first present the crystallographic phase that gives rise to perpendicular magnetic anisotropy (PMA) in FePd. We then show how FePd can be grown with various degrees of PMA. Finally, some magnetic and structural measurements performed on real samples by A. Stellhorn [8] are presented.

3.2 FePd in the $L1_0$ ordered phase

Depending on the growth method, FePd can be in different crystallographic phases [28]. The disordered phase is face-centered cubic (FCC) with disordered atom sites and a lattice parameter of 3.8 Å. The $L1_0$ ordered phase is a tetragonal derivative of the FCC phase with alternating planes of Fe and Pd, as depicted in Fig. 3.1. The lattice parameters of the 2-atom unit cell are $a = b = 2.7$ Å and $c = 3.7$ Å. An alternative 4-atom unit cell can be obtained with a 45° rotation, with the lattice parameters $a' = b' = \sqrt{2}a$ and $c' = c$. The symmetry breaking in the $L1_0$ phase results in a magnetocrystalline anisotropy with an easy axis along the [001] direction. The values of the Curie temperature, saturation magnetization and exchange constant for FePd in the $L1_0$ phase are given in Table 3.1. These values will be used for all the simulations in this thesis, unless stated otherwise. The value of the magnetocrystalline anisotropy constant K_u will be chosen depending on the quality factor Q (Eq. 2.28).

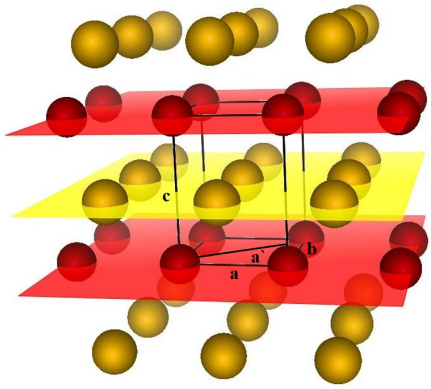

Figure 3.1: Structure of the $L1_0$ phase for FePd, made of alternating planes of Fe and Pd. The 2-atom unit cell is drawn with black lines, with the lattice parameters a, b and c. Figure taken from [8].

Property	**Symbol**	**Value**
Curie temperature	T_C	723 K
Saturation magnetization	M_s	10^6 A/m
Exchange constant	A	$7\,10^{-12}$ J/m

Table 3.1: Magnetic properties of FePd in the $L1_0$ ordered phase. Values from [29] and [30].

3.3 Growth of FePd with various PMA

FePd thin films can be grown by Molecular Beam Epitaxy (MBE), a deposition technique by which oriented growth of a deposit onto a substrate is achieved with atomic or molecular beams. The beam is produced by evaporation through heating in Knudsen effusion cells or with an electron beam in Electron Beam Evaporators (EBVs). Each cell can be closed or opened with a shutter.

The strength of the anisotropy is directly linked to the chemical ordering in the $L1_0$ phase. With MBE, the long-range order and therefore the degree of PMA can be tuned by changing the growth mode and the substrate temperature T_s [26, 8]. The co-deposition growth mode corresponds to evaporating simultaneously the Fe and the Pd. At elevated substrate temperatures ($T_s \sim 600$ K), the diffusion rates are high enough to produce an ordered $L1_0$ phase with high chemical ordering and high PMA. At room temperature, a disordered FCC structure without PMA is obtained. In the shuttered growth mode, the Fe and the Pd are evaporated alternatively by closing

and opening the corresponding shutters. At room temperature (to avoid high diffusion rates), the film can then be grown monolayer by monolayer to obtain low or intermediate chemical ordering.

The samples in A. Stellhorn's work are heterostructure stacks grown by MBE on a MgO substrate. The thickness of the FePd layer range from 30 to 70 nm. In addition to the FePd layer, Cr and Pd layers are used for lattice matching and protection. Some samples also had a superconducting layer of Nb to study the proximity effects between superconductors and ferromagnets.

3.4 Characterization of the FePd thin films

3.4.1 Magnetic characterization

A. Stellhorn measured the surface domain pattern at room temperature by Magnetic Force Microscopy (MFM), as well as the magnetic hysteresis loops in an in-plane (IP) and out-of-plane (OOP) applied field. Since the Curie temperature for FePd is $T_C = 723$ K, FePd is ferromagnetic at room temperature. Moreover, it has been shown that the Nb layer at room temperature has no influence on the magnetic structure in the FePd. MFM images in the as-grown state and hysteresis loop measurements for three samples with different degrees of PMA are shown in Fig. 3.2. Samples high PMA show out-of-plane magnetic domains with a complex maze-like (or labyrinth-like) pattern. The slope in the OOP hysteresis loop is higher than for the IP, indicating an easy axis in the OOP direction. On the contrary, sample with lower PMA present elongated out-of-plane domains with a stripe pattern. The sample with low PMA has an easy axis in the IP direction. An in-depth analysis of such hysteresis curves will be performed in Chapter 5, where the measured hysteresis curves will be compared with those obtained by simulation.

3.4.2 Surface analysis

The surface of the samples was analyzed by Atomic Force Microscopy (AFM). The root mean square surface roughness σ_{rms} of the FePd layers directly after growth is as small as $\sigma_{\text{rms}} < 4$ Å. The samples with high PMA show surface terraces, corresponding to planar defects along the FePd {111} planes. Plane defects inside the FePd layers are also observed for lower anisotropies. Finally, the samples with a Nb layer exhibit 20 to 30 nm deep voids in the FePd layer, which are filled with Nb and MgO. The void to surface ratio is about 1%.

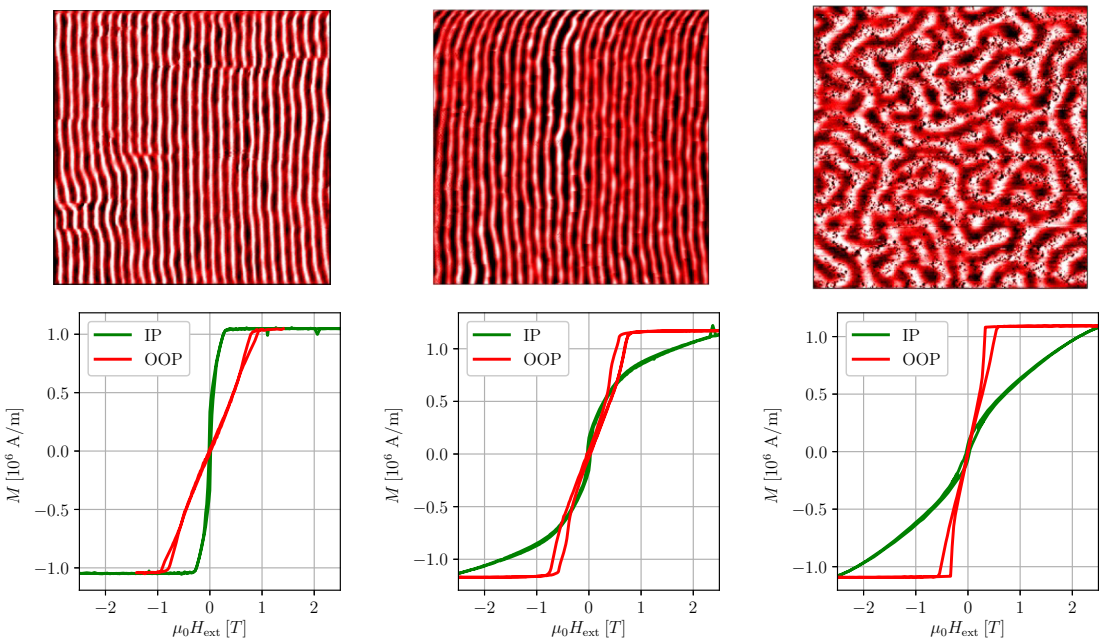

(a) Q=0.47 (low), d=37 nm **(b)** Q=1.46 (mid), d=70 nm **(c)** Q=2 (high), d=44 nm

Figure 3.2: 3μm×3μm MFM top view image in the as-grown state (top) and hysteresis loops with in-plane (IP) and out-of-plane (OOP) applied field (bottom) for three samples with low (a), medium (b) and high (c) PMA. The computed Q values and the thickness d of FePd is specified for each sample. MFM images taken from [8]. Hysteresis loop measurements kindly shared by A. Stellhorn [8].

3.5 Conclusion

The structure of the $L1_0$ phase gives rise to perpendicular magnetic anisotropy (PMA) in FePd thin films. Depending on the growth method, different degrees of PMA can be obtained. This results in very different hysteresis loops. Real samples present a number of defects. As will be shown in Chapter 5, it is crucial to introduce some defects in the simulation of hysteresis curves.

Chapter 4

Critical thickness and domain-wall structure

4.1 Introduction

This chapter addresses the first goal of the thesis, namely the study of the domain-wall structure. In order to observe domain walls, it is first needed to determine the values of thicknesses and anisotropies for which out-of-plane domains are present. Indeed, below a certain critical thickness, the magnetization is forced to be in the plane of the film. The first part of this chapter therefore determines the critical thickness depending on the anisotropy quality factor Q, through simulations with *MuMax3*. In the second part, the precise structure of the domain walls is studied as a function of the thickness d and the quality factor Q. In particular, the size of the Bloch walls and the Néel closure domains are compared for different values of $d/l_{\mathrm{ex},M_\mathrm{s}}$ and Q.

4.2 Critical thickness

Let us consider a thin film with perpendicular magnetic anisotropy (PMA) and no external applied field. In this case, the micromagnetic energy is given by $E_\mathrm{tot} = E_\mathrm{ex} + E_\mathrm{a} + E_\mathrm{d}$, *i.e.* the sum of the exchange energy, the anisotropy energy and the magnetostatic (or demagnetizing) energy. For samples with high PMA ($Q > 1$), the equilibrium magnetic configuration is always composed of alternating out-of-plane (OOP) domains [31]. On the contrary, for samples with low PMA ($Q < 1$), if the thickness d of the film is small enough, the magnetostatic interaction between the surfaces would be large if there were OOP domains and the magnetization is therefore forced to lie in the plane of the film. The thickness below which the magnetization is forced into the plane is called the critical thickness d_c. The critical thickness has been studied in detail in the literature with simplified analytical models for the magnetization profile. However, there are no analytical results for a completely free

magnetization profile in 3 dimensions.

4.2.1 Analytical results

Muller [32] studied the exact solution for the nucleation of a stripe pattern resulting from an instability of the in-plane magnetization. A modern presentation of the work is available in the book of Hubert and Schäfer [25]. The work is limited to a two-dimensional pattern, independent of the coordinate y along the direction of the stripes. The magnetization then only depends on the coordinates in the cross section, namely x and z. Initially, the magnetization lies in-plane such that $m_x = m_z = 0$ and $m_y = 1$. The thickness $d_{c,1}$ above which the in-plane magnetization profile becomes unstable is then computed and corresponds to the solid line in Fig. 4.3a.

Virot *et al.* [31] computed a limit between a strong and a weak stripe pattern characterized by the thickness $d_{c,2}$. In their work, they consider a one-dimensional magnetization profile $m_z(x)$ and $m_y(x)$ with $m_x = 0$. In the so-called Kittel's model, which is used to model thin films with high PMA, the magnetization profile consists of alternating out-of-plane domains with $m_z = \pm 1$ of width w and the width of the Bloch walls is neglected. Virot *et al.* proposed a model for a stripe structure, with again a half-period denoted w, but including the width of the Bloch walls δ, as illustrated in Fig. 4.1. In this model, the inner domains with constant magnetization $m_z = \pm 1$ have a width $w - \delta$ and the Bloch walls in-between are assumed to exhibit a linear variation of the angle $\theta(x)$ between the magnetization direction and the y-axis. This results in a sinewave profile for $m_z(x)$ within the walls, hence the name Sinewave Wall Model (SWM). The micromagnetic energy is then computed and the equilibrium configuration deduced from energy minimization. When the thickness decreases, the domain width w decreases and the wall width δ increases. Just above the second critical thickness $d_{c,2}$, we have $\delta = w$ corresponding to a pure sinewave profile between $+1$ and -1 for m_z. Moreover, at $d_{c,2}$, the total energy of the stripe structure and the in-plane configuration are the same. It is then assumed that for thicknesses smaller than $d_{c,2}$, the configuration becomes a stripe pattern with weak PMA in which $\theta(x)$ alternates between θ_0 and $-\theta_0$ with $\theta_0 < \pi/2$ (whereas θ_0 would be $\pi/2$ for the strong stripe pattern in the SWM). The critical thickness $d_{c,2}$ corresponds to the dashed line in Fig. 4.3a. The first critical thickness $d_{c,1}$ found by Muller then corresponds to the limit between the in-plane magnetization and the weak stripe pattern.

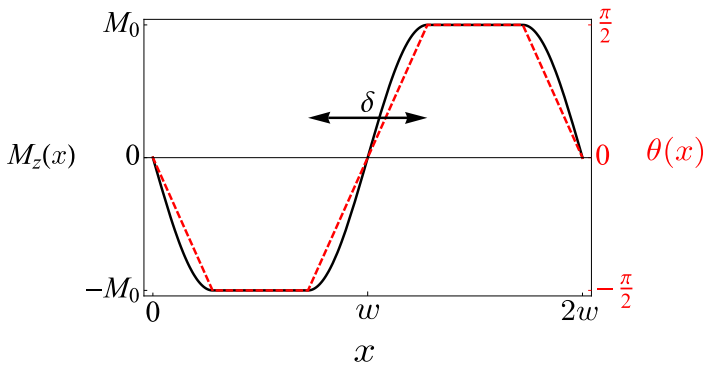

Figure 4.1: Sinewave Wall Model used to compute the second critical thickness $d_{c,2}$. The solid black line corresponds to the z component of the magnetization and the dashed red line to the angle θ with the y axis. Figure modified from [31].

4.2.2 Simulation results

Whereas the critical thicknesses $d_{c,1}$ and $d_{c,2}$ computed by Muller and Virot assume a stripe pattern (magnetization independent of y), we will now look for the critical thickness for a free 3-dimensional profile through micromagnetic simulations. The procedure is the following. For Q values ranging from 0.1 to 1, the equilibrium configuration is computed for different thicknesses d (more precisely, different values of $d/l_{ex,M_s}$). The initial magnetic configuration is a random unit vector for each cell. This corresponds to the paramagnetic state when the sample is heated above the Curie temperature T_C. The total energy comprises the exchange, the demagnetizing and the anisotropy energies. The pseudo-dynamic function is then used, followed by the energy-minimization function to be sure to have a local energy minimum. The simulation box has in-plane dimensions of 500nm×500nm and periodic boundary conditions are imposed in the x and y directions. This enables one to model a thin film with infinite In-Plane dimensions. The values for the material parameters are those given in Table 3.1, which yield a magnetostatic exchange length equal to $l_{ex,M_s} = 3.34$ nm. Since we only consider low anisotropies ($Q \leq 1$), the magnetocrystalline length $l_{ex,K} = l_{ex,M_s}/\sqrt{Q}$ is always larger than l_{ex,M_s}. For the x and y directions, we use $N_x = N_y = 256$ cells giving cells sizes $\Delta x = \Delta y = 1.95$ nm that are smaller than the exchange lengths. In the z direction, 16, 32 or 64 cells are used depending on the thickness in order to have Δz much smaller than the exchange lengths in all cases.

The three types of equilibrium configuration that were obtained are illustrated in Fig. 4.2. The first one is a homogeneous in-plane (IP) configuration. The second one is an intermediate configuration, where the magnetization is mainly IP, but some regions with an out-of-plane (OOP) component start to nucleate. The last one is a maze domain structure, where the OOP component of the magnetization (m_z) alternates between positive and negative values. A stripe pattern was never obtained. We

will see in Chapter 5 that stripe patterns can be obtained after a magnetic field has been applied.

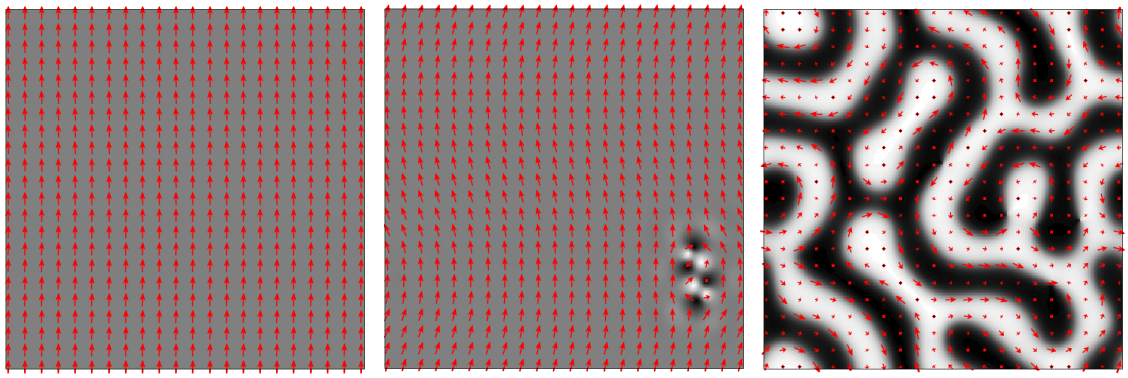

(a) In-plane (IP). **(b)** Intermediate. **(c)** OOP domains.

Figure 4.2: Top view at mid-thickness for the 3 types of equilibrium configurations obtained after energy minimization with a random initial configuration. The OOP component m_z is represented with a black-gray-white color scale in the $[-1, 1]$ range. The IP components are represented with red arrows. (a) $Q = 0.4$, $d/l_{\mathrm{ex},M_\mathrm{s}} = 3.33$. (b) $Q = 0.6$, $d/l_{\mathrm{ex},M_\mathrm{s}} = 3.67$. (c) $Q = 0.4$, $d/l_{\mathrm{ex},M_\mathrm{s}} = 10.67$.

The results of the simulations are summarized in Fig. 4.3a where the three types of configurations are distinguished depending on Q and the thickness d. The critical thickness $d_{\mathrm{c},1}$ from Muller between the IP phase and the weak stripe pattern, and the critical thickness $d_{\mathrm{c},2}$ from Virot between the weak and the strong stripe patterns are also represented in the figure. One can see that the transition from the intermediate state to the OOP-domains state is very close to the first critical thickness $d_{\mathrm{c},1}$, which will from now be referred to as the critical thickness d_c. This indicates that the stripe model from Muller is very good to compute d_c, even in the 3-dimensional case. It is also important to note that in Fig. 4.3a, the thickness is normalized with the magnetocrystalline exchange length $l_{\mathrm{ex},K} = \sqrt{A/K_\mathrm{u}}$, which diverges when $Q = K_\mathrm{u}/(\frac{1}{2}\mu_0 M_\mathrm{s}^2)$ tends to zero. Therefore, for $Q = 0$, the magnetization is in-plane for any thickness. The critical thickness d_c normalized by $l_{\mathrm{ex},M_\mathrm{s}} = \sqrt{\frac{A}{\frac{1}{2}\mu_0 M_\mathrm{s}^2}}$ is given in Fig. 4.3b.

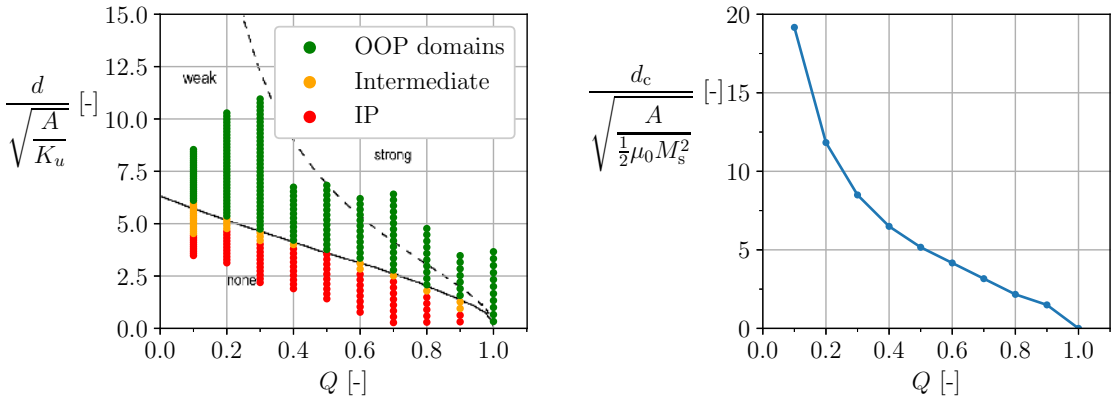

(a) **(b)**

Figure 4.3: Critical thickness of a thin magnetic film as a function of the anisotropy quality factor Q. (a) Figure adapted from [31]. The solid line is the thickness $d_{c,1}$ obtained by Muller [32, 25] between the in-plane phase and the weak stripe phase. The dashed line is the thickness $d_{c,2}$ obtained with the SWM by Virot *et al.* [31] between the weak and the strong stripe phases. The results of the simulations are plotted on the same figure, distinguishing the IP phase, the intermediate phase and the phase with OOP domains. (b) Critical thickness $d_c = d_{c,1}$ normalized by $l_{ex,M_s} = \sqrt{\frac{A}{\frac{1}{2}\mu_0 M_s^2}}$.

4.3 Domain-wall structure

In this section, the structure of the domain walls is investigated for thicknesses above d_c and Q values between 0.5 and 2. The thickness d is chosen to range from $10l_{ex,M_s}$ (= 33.4 nm) to $25l_{ex,M_s}$ (= 83.4 nm). The magnetocrystalline exchange length $l_{ex,K} = l_{ex,M_s}/\sqrt{Q}$ then ranges from 4.72 nm to 2.36 nm. The simulation box has again in-plane dimensions of 500nm×500nm with periodic boundary conditions in the x and y directions. In order to have an accurate description of the domain wall structure, we use $N_x = N_y = 384$ cells in the IP directions and $N_z = 64$ cells in the z direction. The procedure is then the same as in Section 4.2.2: the total energy comprises the exchange, the demagnetizing and the anisotropy energies, and the equilibrium configuration is computed with the pseudo-dynamic and the energy-minimization functions starting with a random initial configuration. It is repeated for the different thicknesses and Q values represented in Fig. 4.4.

In thin films with PMA, the domain walls between the OOP domains are typically of Bloch type in the middle of the thickness, with Néel closure domains (or Néel "caps") at the top and bottom surfaces [33, 34]. A simple model is illustrated in Fig. 4.5, where w is the characteristic size of the domains. In this model, the domain walls are characterized by three values: the width δ_B of the Bloch wall at the center of the thickness, the height t_B of the Bloch wall and the width δ_N of the Néel caps at the top and bottom.

The domain width w is computed by performing several cuts in the maze pattern, as illustrated in Fig. 4.6, and taking the average of the domain widths. To compute the Bloch wall width, we define the angle $\theta(x) = \arctan(m_y/m_z)$ at mid-thickness of the film, with x the direction perpendicular to the wall plane. The width δ_B is then computed by linear extrapolation of the tangent $\mathrm{d}\theta/\mathrm{d}x$ at the center. The Néel wall width δ_N is also computed by extrapolation of the tangent, with the angle $\phi(x) = \arctan(m_x/m_z)$ at the top and bottom surfaces. Finally, the thickness of the Bloch wall t_B is defined as the thickness for which 50% of the rotation of the magnetization is completed, using the angle $\gamma(z) = \arctan(m_y/m_x)$. The procedure to compute the domain wall parameters is illustrated in Fig. 4.7.

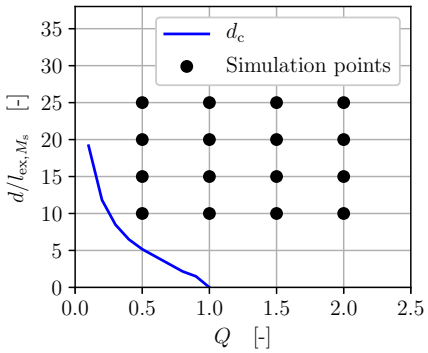

Figure 4.4: Points in the thickness-Q plane for which the domain-wall structure is studied. The blue line corresponds to the critical thickness d_c.

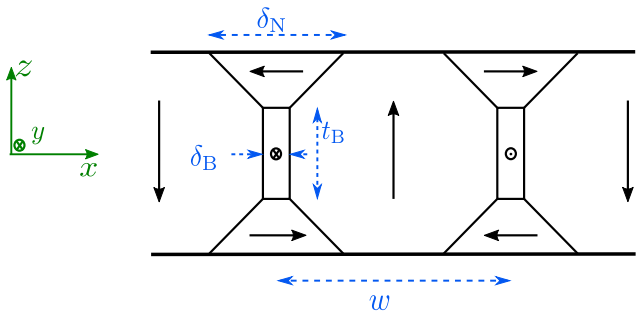

Figure 4.5: Simple model for the domain-wall structure between alternating OOP domains. The black arrows indicate the direction of the magnetization. The domain walls are composed of a Bloch wall at the center, with closure domains at the surfaces. The domain wall dimensions δ_B, δ_N, t_B and the domain width w are shown with dashed blue arrows. The coordinate system is shown in green.

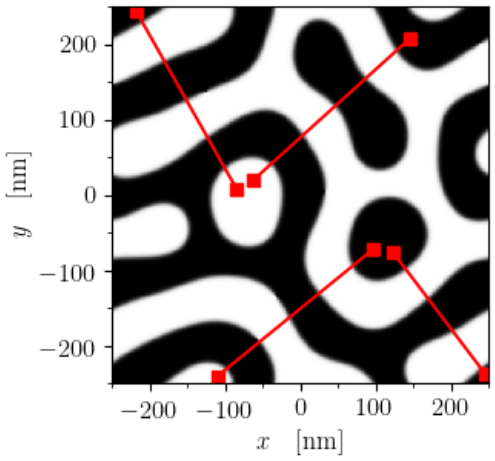

Figure 4.6: Illustration of the procedure used to compute the domain width w. The image is a top view at mid-thickness of a simulation with $Q = 1$ and $d/l_{ex,M_s} = 15$. The OOP component m_z is represented with the black-gray-white color scale. The red lines are the cuts used to compute the average domain width w.

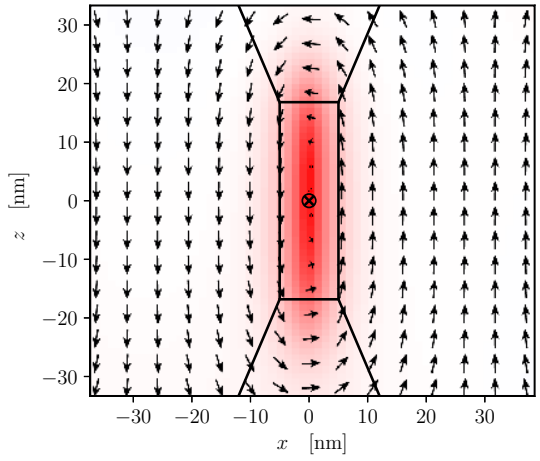

(a) Simple model drawn on a simulation results.

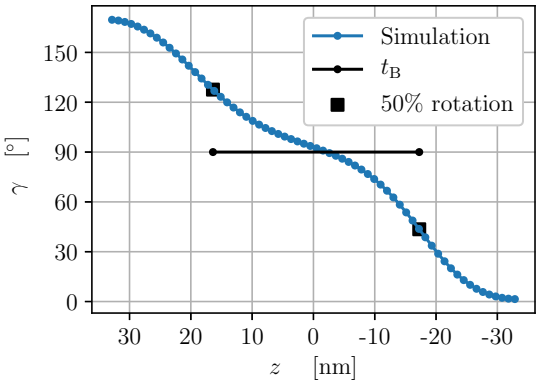

(b) $\gamma(z) = \arctan(m_y/m_x)$ at $x = 0$ nm to compute t_B.

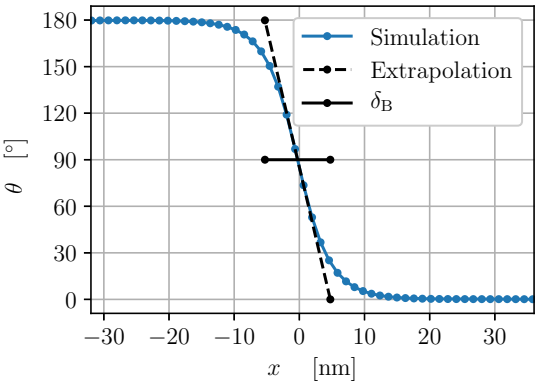

(c) $\theta(x) = \arctan(m_y/m_z)$ at $z = 0$ nm to compute δ_B.

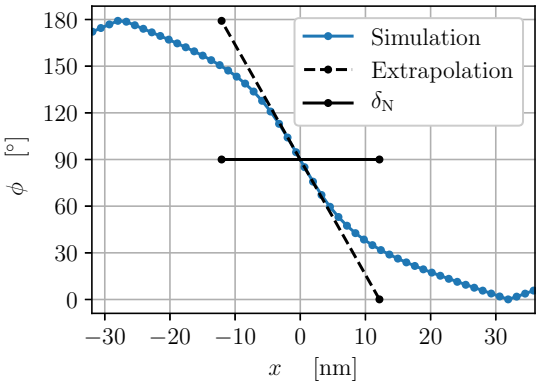

(d) $\phi(x) = \arctan(m_x/m_z)$ at the top surface to compute δ_N.

Figure 4.7: Illustration of the procedure used to compute the domain wall parameters δ_B, δ_N and t_B. (a) Domain wall (DW) example for a simulation with $Q = 1$ and $d/l_{ex,M_s} = 20$. The black arrows indicate the direction of the magnetization in the xz-plane. The red color represents the component m_y. The simple model of a DW is drawn on top, with the values obtained in the other graphs. (b) Computation of the Bloch thickness t_B for which 50% of the γ-rotation is completed. (c) Computation of the Bloch width δ_B by linear extrapolation of θ. (d) Computation of the Néel cap width δ_N by linear extrapolation of ϕ.

The results of the DW structure analysis are summarized in Fig. 4.8. In Fig. 4.8a, one can see that for a fixed Q, the domain width w increases with the film thickness d. This is in accordance with the result of Gehanno [26]. Gehanno showed with the Kooy and Enz model [35] (equivalent to Kittel's model, with widths w_1 and w_2 for the domains pointing up and down) that for high Q, the size of the domains increases as $\sqrt{d}$. For $Q < 1$, Murayama also showed that the domain width increases as $\sqrt{d}$ [36]. We can also see that for $Q > 1$, at constant thickness, the width w increases when Q increases. For the thicknesses well above d_c that we are considering here, the increase of w with d and Q can be explained by considering the energy of the domain walls. Indeed, the energy of the domain walls increases with d and with Q (see Eq. 2.36). Increasing the domain width w results in a decrease in the number of domain walls and therefore a decrease in the total energy. For thicknesses closer to d_c, the magnetostatic interaction (demagnetizing energy) between the two surfaces is larger and the behavior can therefore be different.

In Fig. 4.8b, the ratio t_B/d of the Bloch thickness over the film thickness is presented. The Bloch thickness represents 30 to 60% of the film thickness. For a fixed thickness, the ratio only slightly increases when Q increases, whereas for a fixed value of Q, the ratio significantly increases with the film thickness d. One must understand that the Néel caps are a consequence of the demagnetizing field. An upward domain creates positive magnetic charges at the top surface and negative charges at the bottom surface, and the inverse is true for downward domains. A demagnetizing field is therefore produced in the direction opposite to the magnetization in the domains. On the top or bottom surface at a domain wall, the region with positive charges (*e.g.* on the left) is adjacent to a region with negative charges (*e.g.* on the right). This gives rise to a demagnetizing field from the left to the right. The magnetization in this region rotates to align with the demagnetizing field, forming Néel caps. When d increases, the thickness of the Néel caps increases, but not as fast as d. As a results, the ratio t_B/d increases with d. For $d/l_{ex,M_s} = 10$, we have $t_B/d \simeq 30\%$ whereas for $d/l_{ex,M_s} = 25$, $t_B/d \simeq 55\%$.

In Fig. 4.8c, one can see that the Bloch width δ_B is nearly independent of the thickness. Moreover, it is close but slightly smaller than the width $\delta_w = \pi\sqrt{\frac{A}{K_u}}$ computed in Section 2.5.4 where only the exchange and anisotropy energies are considered.

Finally, in Fig. 4.8d, one can see that the Néel caps width δ_N decreases when Q increases. This enables to decrease the high anisotropy energy, while increasing the exchange and demagnetizing energy. At $Q = 0.5$, δ_N corresponds to 80 to 100% of the domain width w. At $Q = 2$, it corresponds to only about 20% of the domain width.

Those results are illustrated in Fig. 4.9 by drawing the DW model on top of a cross section for four different simulations. Let us first compare the bottom and top images for a constant Q. One can see that the domain width w and the ratio t_B/d increases when the thickness increases, while the Bloch and the Néel widths δ_B and δ_N are almost unchanged. Comparing now the left and right images for a constant thickness, one can see that the domain width w increases when Q increases, while δ_B and δ_N drastically decrease.

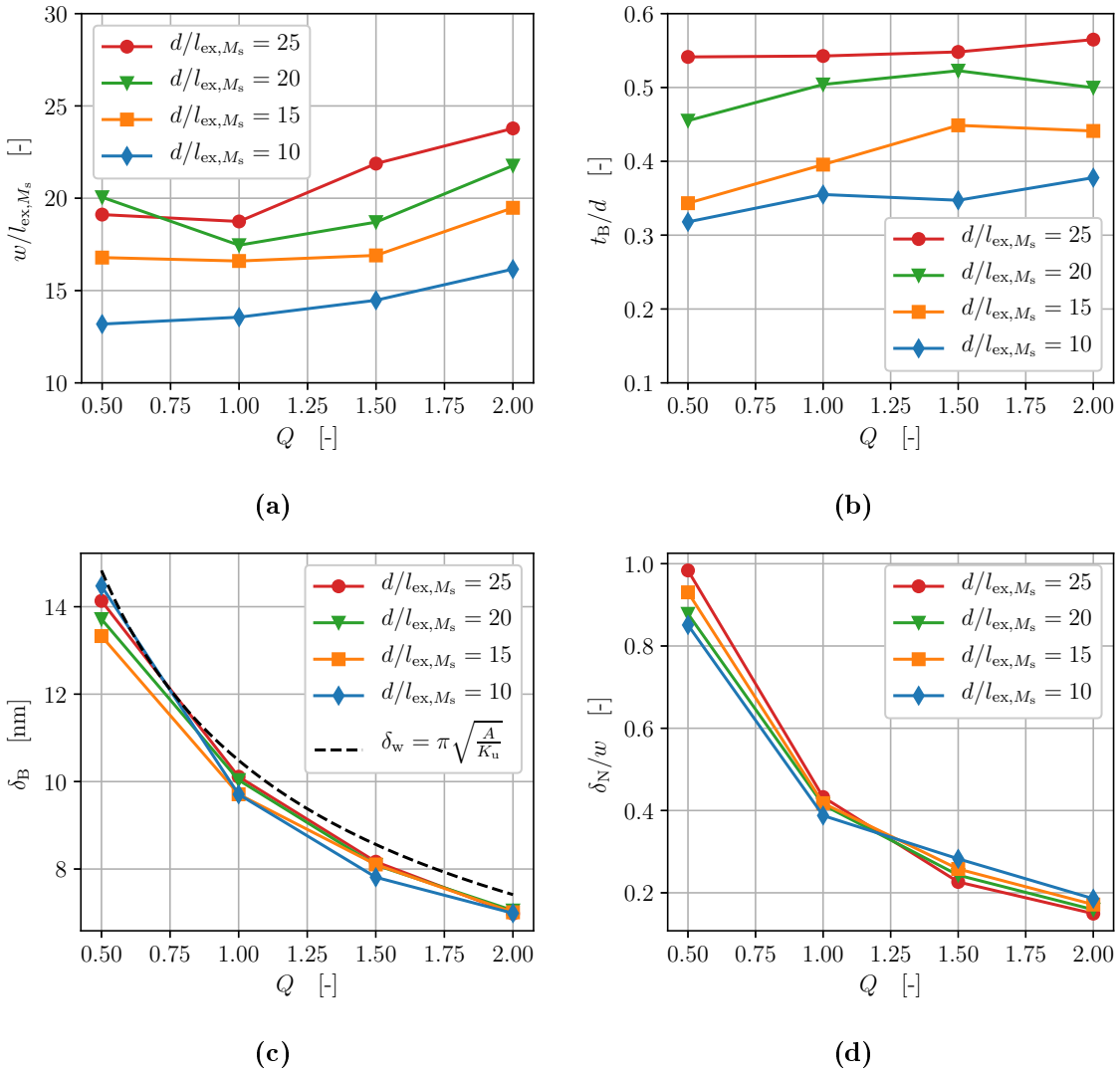

Figure 4.8: Results of the domain wall analysis for simulations with the different thicknesses d and Q values of Fig. 4.4. (a) Domain width w over exchange length l_{ex,M_s}. (b) Bloch thickness over sample thickness t_B/d. (c) Bloch width δ_B. The dashed line represents the result δ_w obtained without demagnetizing field (Eq. 2.35). (d) Néel cap width over domain width δ_N/w.

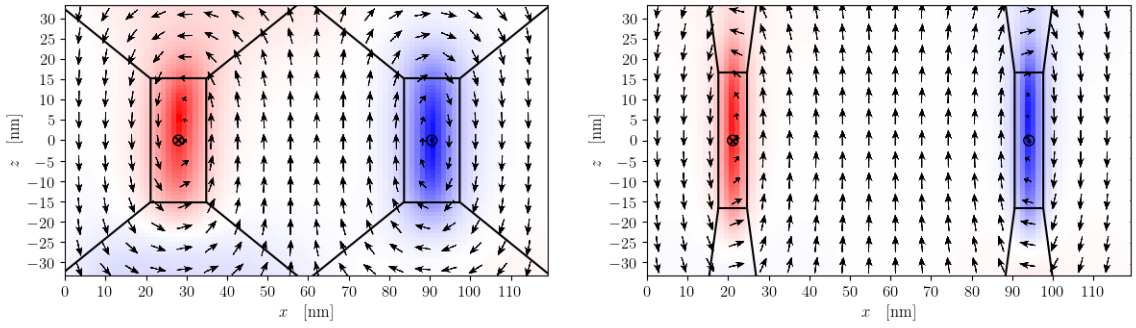

(a) $Q = 0.5$, $d/l_{\mathrm{ex},M_\mathrm{s}} = 20$

(b) $Q = 2$, $d/l_{\mathrm{ex},M_\mathrm{s}} = 20$

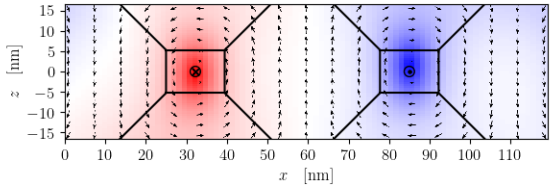

(c) $Q = 0.5$, $d/l_{\mathrm{ex},M_\mathrm{s}} = 10$

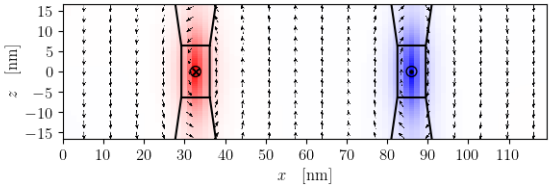

(d) $Q = 2$, $d/l_{\mathrm{ex},M_\mathrm{s}} = 10$

Figure 4.9: Cross section with 2 DWs for four different simulations. The blue-white-red color scale represents the m_y component in the $[-1, 1]$ range. The simple model of a DW is drawn on top with the values obtained in Fig. 4.8.

4.4 Conclusion

Below the critical thickness d_c, the equilibrium magnetization is forced in the plane of the film due to the magnetostatic interaction between the two surfaces. The critical thickness diverges to infinity when the anisotropy factor Q tends towards zero. When Q increases, d_c decreases until zero at $Q = 1$. For $Q > 1$, the equilibrium configuration is therefore made of out-of-plane domains for any thickness.

The domain walls (DWs) between the out-of-plane domains are of Bloch-type at the middle of the thickness. On the top and bottom surfaces, Néel closure domains are formed. The width of the DWs is nearly independent of the thickness, and decreases when the anisotropy factor Q increases. When the thickness increases, the ratio of Bloch thickness over film thickness t_B/d increases. Finally, the width of the domains w increases with the thickness and with Q.

Chapter 5

Magnetization, hysteresis and reversal mechanisms

5.1 Introduction

Due to its perpendicular magnetic anisotropy (PMA), FePd is a promising material for applications in spintronics, like for example Magnetoresistive Random Acces Memories (MRAMs) [5]. In order to use this material in applications, it is important to understand the reversal mechanisms when the magnetization switches from the saturated state in one direction to the saturated state in the opposite direction. The reversal mechanisms and the patterns formed by the out-of-plane domains determine the shape of the hysteresis curves obtained with an in-plane (IP) and an out-of-plane (OOP) applied field.

Hysteresis loop measurements performed by A. Stellhorn (A.S.) on three samples with different degrees of PMA are shown in Fig. 5.1. For the in-plane (IP) curve, the in-plane components of the magnetization and the applied field are displayed in the graph, whereas for the out-of-plane (OOP) curve, the out-of-plane components are displayed. One observes that the lower the anisotropy quality factor Q, the steeper the IP curve. Moreover, the IP curves exhibit some hysteresis around zero applied field, whereas the OOP curves have hysteresis at the extremities.

In this chapter, the hysteresis curves are reproduced by micromagnetic simulations using *MuMax3* and the reversal mechanisms are analyzed. The method and the parameters used for the simulations are explained in Section 5.2. The hysteresis curves and reversal mechanisms are investigated for low and high PMA for an in-plane applied field in Section 5.3 and an out-of-plane applied field in Section 5.4. Conclusions are then drawn in Section 5.5.

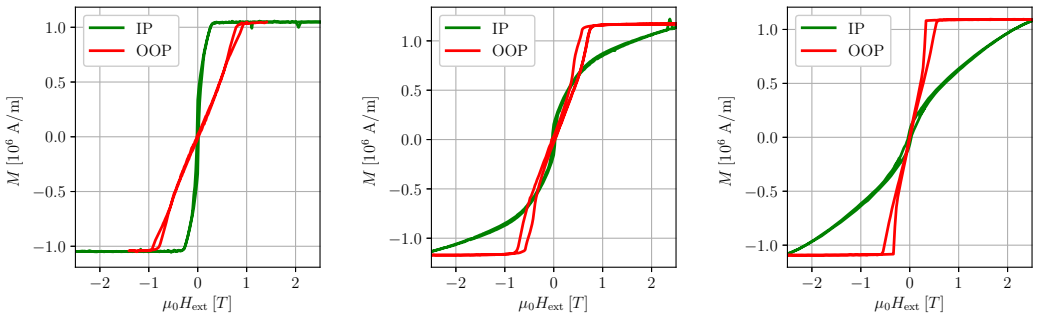

(a) Q=0.47 (low), d=37 nm **(b)** Q=1.46 (mid), d=70 nm **(c)** Q=2 (high), d=44 nm

Figure 5.1: Hysteresis loops with an in-plane (IP) and out-of-plane (OOP) applied field for three samples with low (a), medium (b) and high (c) PMA. The computed Q values and the thickness d of FePd layer is specified for each sample. Data shared by A.S. [8].

5.2 Simulation methodology

To compute the initial magnetization curve and the hysteresis curve, the equilibrium configuration is first computed using the pseudo-dynamic algorithm (*i.e.* only the damping term of the LLG equation) starting from a random configuration. An increasing external field is then applied with small steps, and the magnetic configuration is computed at each step with the pseudo-dynamic algorithm, until complete saturation. The hysteresis loop is then computed by varying the applied field with small steps from the saturated state in one direction to the saturated state in the other direction. The energy minimization algorithm is not used in these simulations because it does not converge efficiently enough in some of these complex configurations.

In a simulation geometry with high symmetry like a thin film, one should avoid applying the field in a direction of symmetry. Indeed, if the simulation is perfectly symmetrical, the solution can be stuck in an unstable, non-physical state. It is therefore advised to always tilt the applied field with a small angle from the symmetry axis. In the simulations of this chapter, the in-plane field is applied mainly along the y direction, but with a small tilt of 0.5° in the x and z directions. Similarly, for the out-of-plane case, the field is applied mainly along the z direction, with a small tilt of 0.5° in the y direction.

In all the simulations, a box of 500nm×500nm is used with periodic boundary conditions in the in-plane directions (x and y). The domain is discretized with a regular mesh of 256×256×32 cells in order to have cells smaller than the exchange lengths in all cases.

As mentioned in Section 2.4.3, the hysteresis curves depend on defects in the bulk or at the surface of the sample [10]. To obtain hysteresis curves close to experimental measurements, it is therefore mandatory to introduce some defects. The specific role of those defects is discussed in the following sections. The two types of defects used in this work are a distribution of the anisotropy, as suggested by Fallarino *et al.* [37], and holes through the sample.

The anisotropy distribution is directly linked to the chemical ordering in the crystal. For a crystal with low order, the intensity and the axis of the anisotropy is expected to vary within the sample whereas for a crystal with high order, it is expected to be almost constant. It can also be seen as a way to model the planar defects observed along the FePd {111} planes in real samples [8, 26] (see Section 3.4.2). The anisotropy distribution is modeled by defining grains of characteristic size r_g using a Voronoi tesselation [38, 39]. The anisotropy constant K_u in the grains follows a normal distribution around its mean value with a standard deviation σ_{K_u}. The anisotropy axis deviates from the z direction by an angle η that follows a normal distribution around 0 with a standard deviation $\sigma_{\mathbf{e}_\mathrm{u}}$. For the sample with low PMA, it is chosen to use grains of size $r_g = 25$ nm with $\sigma_{K_\mathrm{u}} = 5\%$ and $\sigma_{\mathbf{e}_\mathrm{u}} = 5°$. For the sample with high PMA, we use larger grains of size $r_g = 50$ nm with much smaller standard deviations $\sigma_{K_\mathrm{u}} = 0.1\%$ and $\sigma_{\mathbf{e}_\mathrm{u}} = 0.1°$.

In order to enable the nucleation of reversal domains for the sample with high PMA during the OOP hysteresis loop, 3 holes through the thickness of the sample with diameter $D_\mathrm{holes} = 10$ nm are added. Holes can easily be modeled by defining regions with a zero saturation magnetization ($M_\mathrm{s} = 0$ A/m). These holes can be seen as a way to model the 20-to-30nm-deep voids observed in the FePd layer in [8] (see Section 3.4.2).

Other types of defects could also be used, like surface roughness, thermal fluctuations or dynamic effects. Surface roughness can easily be modeled by defining grains with different thicknesses. Thermal fluctuations and dynamic effects can be modeled in *MuMax3* by adding thermal noise and integrating the LLG equation (Eq. 2.22). Thermal fluctuations can indeed trigger nucleation by enabling the magnetization to jump over energy barriers. However, for the sake of simplicity, it is chosen to only use holes and anisotropy distribution as defects. These two types of defect are sufficient to enable reversal, to understand the reversal mechanisms and to show the role of each defect. Adding other types of defects would only make the simulations more complex, and would not contribute to the understanding of the mechanisms.

The parameters used for the two main simulation samples of this chapter are summarized in Table 5.1 and the defects are illustrated in Fig. 5.2.

	Low PMA sample	**High PMA sample**
Width	$W = 500$ nm	$W = 500$ nm
Thickness	$\frac{d}{l_{\mathrm{ex},M_\mathrm{s}}} = 11.53$	$\frac{d}{l_{\mathrm{ex},M_\mathrm{s}}} = 13.71$
Quality factor	$Q = 0.47$	$Q = 2.0$
Saturation magnetization	$M_\mathrm{s} = 10^6$ A/m	$M_\mathrm{s} = 10^6$ A/m
Exchange constant	$A = 7\ 10^{-12}$ J/m	$A = 7\ 10^{-12}$ J/m
Anisotropy distribution: - grain size - intensity standard deviation - axis standard deviation	 $r_g = 25$ nm $\sigma_{K_\mathrm{u}} = 5\%$ $\sigma_{\mathbf{e}_\mathrm{u}} = 5°$	 $r_g = 50$ nm $\sigma_{K_\mathrm{u}} = 0.1\%$ $\sigma_{\mathbf{e}_\mathrm{u}} = 0.1°$
Holes: - number - diameter	 / /	 $n_\mathrm{holes} = 3$ $D_\mathrm{holes} = 10$ nm
Discretization	$256 \times 256 \times 32$	$256 \times 256 \times 32$

Table 5.1: Parameters chosen for the two main simulation samples.

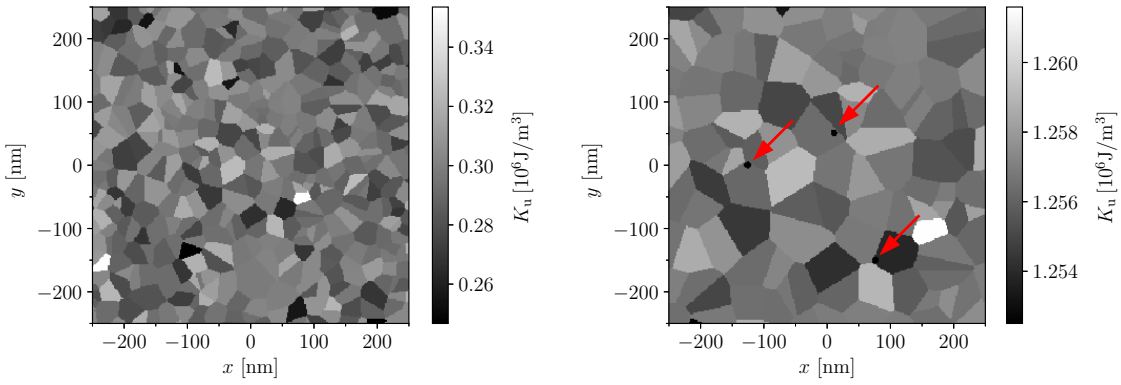

(a) Low PMA sample.

(b) High PMA sample.

Figure 5.2: Illustration of the defects chosen for the simulations of the samples with (a) low and (b) high PMA. The anisotropy constant K_u in the grains is represented with a gray color scale. The three holes for the sample with high PMA are indicated with red arrows.

5.3 In-plane magnetic field

5.3.1 Low PMA sample

In order to model the reversal during the IP hysteresis curve, it is needed to introduce some defects such as an anisotropy distribution. Indeed, one can see in Fig. 5.3a that without anisotropy distribution, the magnetization is stuck in the saturated state until it switches to the saturated state in the other direction in one single jump. By introducing 25nm-large grains with an anisotropy distribution, the hysteresis is reduced and the reversal occurs smoothly. Indeed, introducing defects produces multiple minimums in the energy landscape, enabling the magnetization configuration to jump from minimum to minimum during the reversal. This is analogous to the Barkhausen jumps observed in real samples (see Section 2.4.4). Increasing the standard deviations up to $\sigma_{K_u} = 5\%$ and $\sigma_{\mathbf{e}_u} = 5°$ enables one to obtain a curve close to the experiment. Increasing further the standard deviations would make the magnetic configuration very complex, hiding the main reversal mechanisms. Starting from the equilibrium configuration, the initial magnetization curve and the hysteresis loop are shown in Fig. 5.3b.

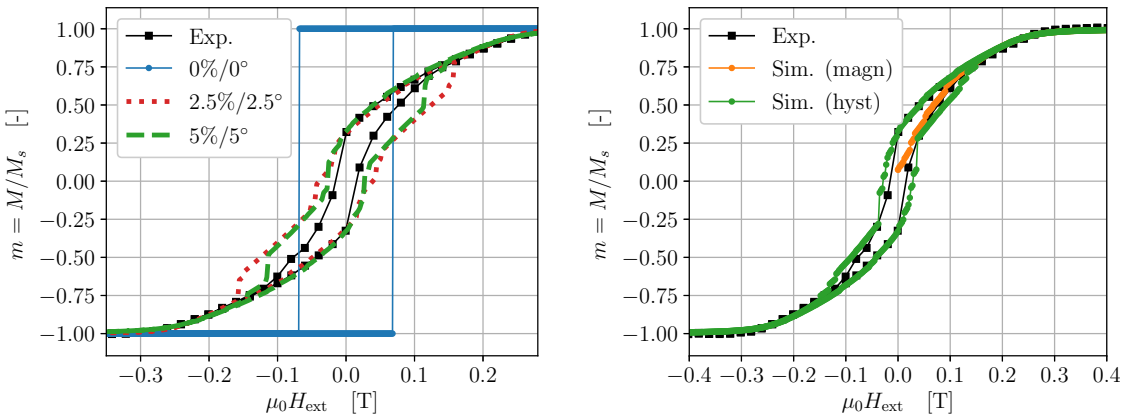

(a) **(b)**

Figure 5.3: (a) Comparison of the in-plane (IP) hysteresis loop for multiple anisotropy distributions (σ_{K_u} / $\sigma_{\mathbf{e}_u}$) with experimental measurements (Exp.). (b) In-plane initial magnetization (magn.) and hysteresis curves (hyst.) for $\sigma_{K_u} = 5\%$ and $\sigma_{\mathbf{e}_u} = 5°$ compared to the experimental curve. Experimental data shared by A.S. [8].

The IP magnetization mechanism for the sample with low PMA is shown in Fig. 5.4. Starting from a maze pattern at $\mu_0 H_{ext} = 0$ mT, the pattern gradually changes into a stripe pattern as the IP applied field increases. At $\mu_0 H_{ext} = 150$ mT, the IP component is aligned with the applied field in the y direction, and the OOP component alternates between positive and negative values forming a stripe pattern. Increasing

further the field, the IP component increases and the OOP component decrease, until full IP saturation is reached.

The IP reversal mechanism for the sample with low PMA is illustrated in Figs. 5.5 and 5.6. Starting from the saturated state at 750 mT, the IP component gradually decreases and the OOP component increases to form a stripe pattern at 150 mT. The stripes are not perfectly straight and parallel. They indeed exhibit some branching and oscillations due to the grains used to model the defects. If one uses smaller standard deviations for the defects, the stripe pattern will be cleaner, but the hysteresis curve will be further from the experiments. At remanence (0 mT), one observes OOP stripe domains, with the IP component of all the Bloch walls in the direction of the initial saturated state. This is illustrated in Fig. 5.6a where all the walls have a positive y component. These Bloch walls are the origin of the remanent magnetization $M_\mathrm{r} \simeq 0.33 M_\mathrm{s}$. Increasing the field in the reverse direction, the IP component of the Bloch walls flips for one wall after another, as can be seen in Figs. 5.6b and 5.6c. This gives rise to the rapid decrease of the IP magnetization visible in Fig. 5.3b. When half of the walls have flipped, the average IP magnetization is zero. This is obtained for the coercive field $\mu_0 H_\mathrm{c} = 28$ mT (slightly overestimating the experimental value of 15 mT). The order in which the walls flip depends on the defects that can lower the energy barrier for certain walls more than for the others. For this reason, it is difficult to obtain results very close to the measurements for this part of the curve. Once all the walls have flipped, when further increasing the field in the reverse direction, the IP component gradually increases and the OOP component decreases until saturation, with good agreement with the measurements.

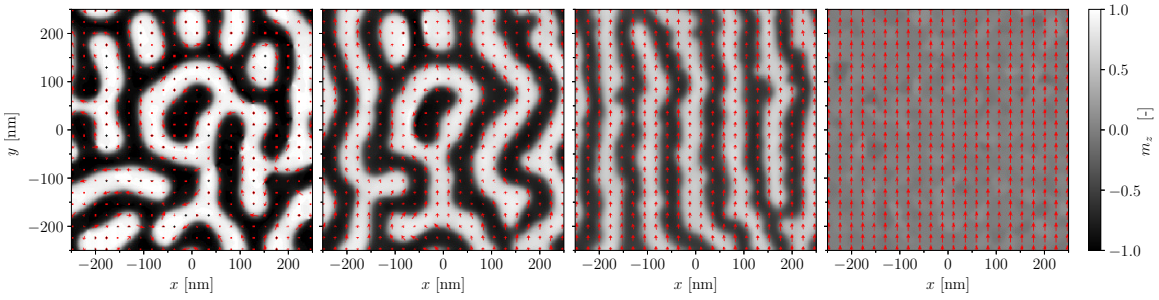

(a) $\mu_0 H_\mathrm{ext} = 0\mathrm{mT}$ **(b)** $\mu_0 H_\mathrm{ext} = 75\mathrm{mT}$ **(c)** $\mu_0 H_\mathrm{ext} = 150\mathrm{mT}$ **(d)** $\mu_0 H_\mathrm{ext} = 750\mathrm{mT}$

Figure 5.4: Magnetization mechanism from the equilibrium configuration to IP saturation for the sample with low PMA. Top view at mid-thickness for different values of the external applied field H_ext. Gray color scale: OOP component m_z. Red arrows: IP components. (See **Vid01**).

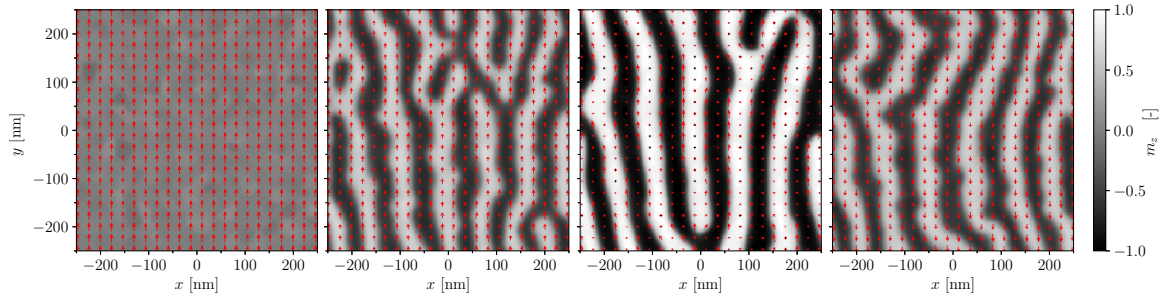

(a) $\mu_0 H_{\text{ext}} = 750\text{mT}$ **(b)** $\mu_0 H_{\text{ext}} = 150\text{mT}$ **(c)** $\mu_0 H_{\text{ext}} = 0\text{mT}$ **(d)** $\mu_0 H_{\text{ext}} = -150\text{mT}$

Figure 5.5: IP reversal mechanism for the sample with low PMA. Top view at mid-thickness for different values of the external applied field H_{ext}. Gray color scale: OOP component m_z. Red arrows: IP components. (See **Vid02**).

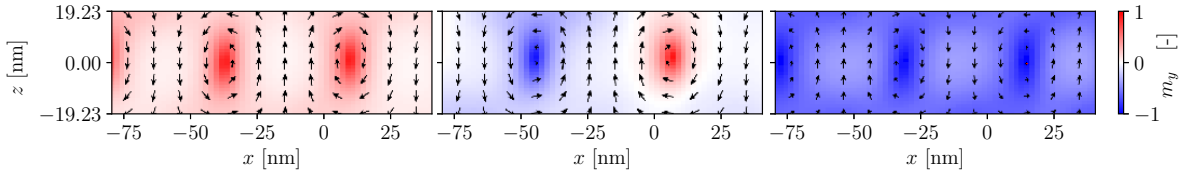

(a) $\mu_0 H_{\text{ext}} = 0\text{mT}$ **(b)** $\mu_0 H_{\text{ext}} = -30\text{mT}$ **(c)** $\mu_0 H_{\text{ext}} = -150\text{mT}$

Figure 5.6: IP reversal mechanism for the sample with low PMA. Cross section for different values of the external applied field H_{ext}. Blue-white-red color scale: m_y component. (See **Vid03**).

5.3.2 High PMA sample

The IP magnetization and hysteresis curves for the sample with high PMA are shown in Fig. 5.7, for which much smaller standard deviations are used ($\sigma_{K_u} = 0.1\%$ and $\sigma_{\mathbf{e}_u} = 0.1°$) to represent the high chemical ordering. The curves are in good agreement with the measurements, except again during the switching near coercivity, and also near saturation. The deviation near saturation results from the difference in slope of the two curves. This could probably be fixed by adjusting the value of Q in order to have exactly the same slope.

The IP magnetization mechanism for the sample with high PMA is shown in Fig. 5.8. Starting from a maze pattern at 0 mT, it gradually elongates in the y direction as the field increases. The IP component increases until full saturation is reached. Since the PMA is high, a large in-plane field is needed to saturate the sample. This explains why the IP curve for high PMA is less steep than for low PMA.

The IP reversal mechanism is illustrated in Figs. 5.9 and 5.10. The mechanism is comparable to the one for the sample with low PMA, with a few differences. A stripe pattern is also obtained, exhibiting branches and with pinning at the 3 holes. At remanence, as illustrated in Fig. 5.10b, all the Bloch walls have their IP component in the direction of the previous saturated state, yielding a remanent magnetization $M_\mathrm{r} \simeq 0.086 M_\mathrm{s}$. The main difference is for the switching around coercivity. Due to the narrow anisotropy distribution in this simulation, the Bloch walls do not switch one after another as it was the case for the sample with low PMA with a lot of defects. On the contrary, as can be seen in Fig. 5.10c, the magnetization gradually rotates, alternatively at the top and bottom surfaces. This gives rise to the gradual decrease of the IP magnetization after remanence in Fig. 5.7, before the Bloch walls start to flip at the coercive field $\mu_0 H_\mathrm{c} = 100$ mT (highly overestimating the experimental value of 31 mT). Since the difference with the measurements is high, the real sample probably contains more defects than what was used in the simulation, with a reversal mechanism closer to the one described for low PMA.

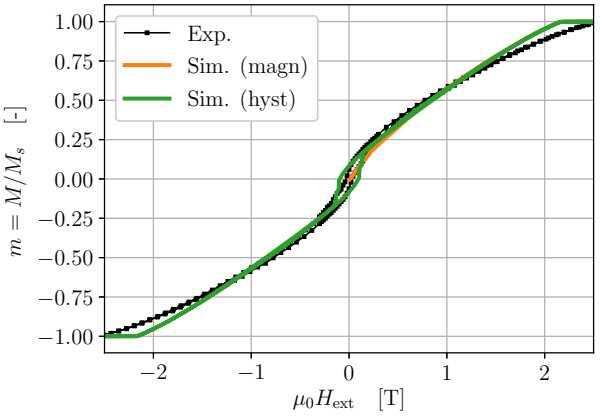

Figure 5.7: In-plane magnetization and hysteresis curves for the sample with high PMA with $\sigma_{K_\mathrm{u}} = 0.1\%$ and $\sigma_{\mathbf{e}_\mathrm{u}} = 0.1^\circ$ compared to the experimental curve. Experimental data shared by A.S. [8].

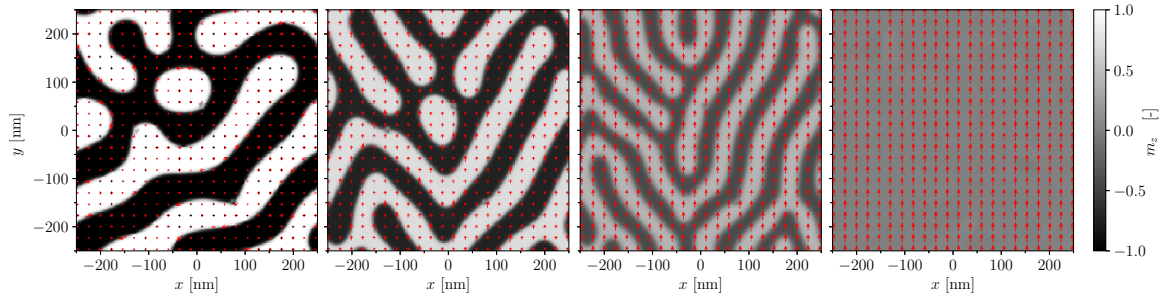

(a) $\mu_0 H_{\text{ext}} = 0\text{T}$ **(b)** $\mu_0 H_{\text{ext}} = 0.9\text{T}$ **(c)** $\mu_0 H_{\text{ext}} = 1.8\text{T}$ **(d)** $\mu_0 H_{\text{ext}} = 2.3\text{T}$

Figure 5.8: Magnetization mechanism from the equilibrium configuration to IP saturation for the sample with high PMA. Top view at mid-thickness for different values of the external applied field H_{ext}. Gray color scale: OOP component m_z. Red arrows: IP components. (See **Vid04**).

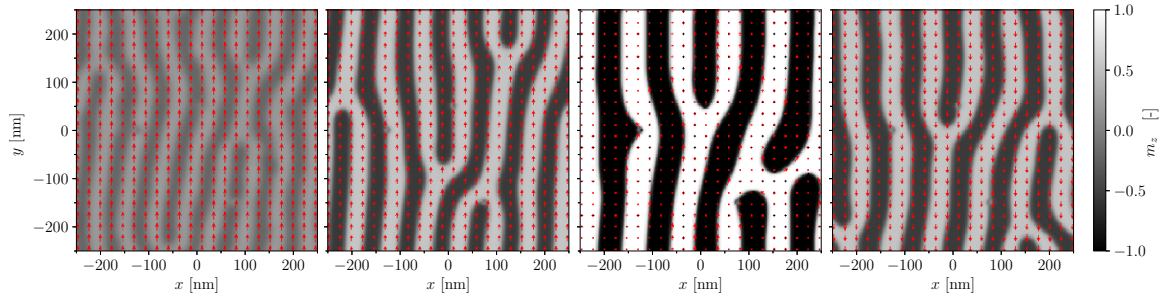

(a) $\mu_0 H_{\text{ext}} = 2.1\text{T}$ **(b)** $\mu_0 H_{\text{ext}} = 1.5\text{T}$ **(c)** $\mu_0 H_{\text{ext}} = 0\text{T}$ **(d)** $\mu_0 H_{\text{ext}} = -1.5\text{T}$

Figure 5.9: IP reversal mechanism for the sample with high PMA. Top view at mid-thickness for different values of the external applied field H_{ext}. Gray color scale: OOP component m_z. Red arrows: IP components. (See **Vid05**).

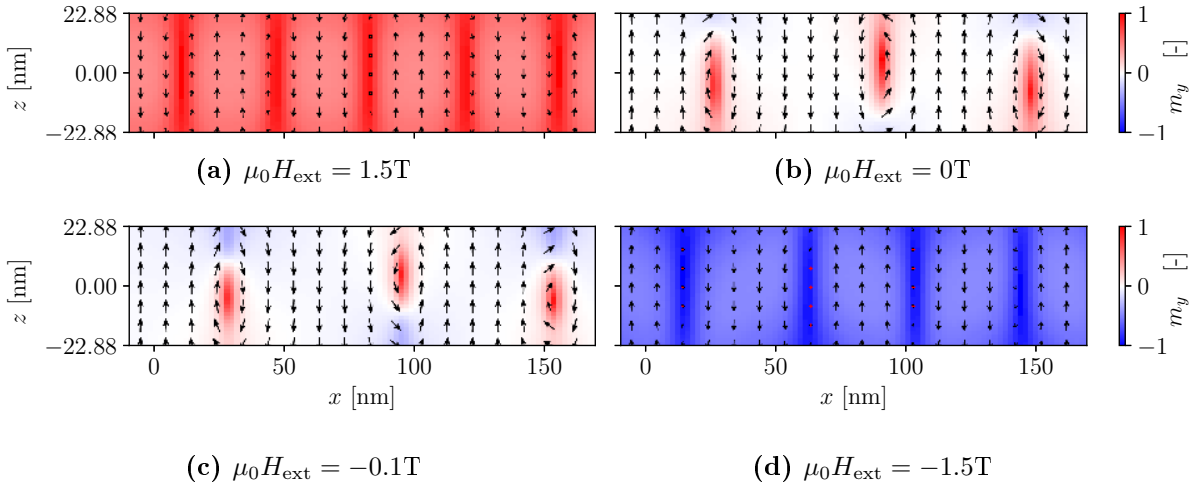

(a) $\mu_0 H_{\text{ext}} = 1.5\text{T}$ **(b)** $\mu_0 H_{\text{ext}} = 0\text{T}$

(c) $\mu_0 H_{\text{ext}} = -0.1\text{T}$ **(d)** $\mu_0 H_{\text{ext}} = -1.5\text{T}$

Figure 5.10: IP reversal mechanism for the sample with high PMA. Cross section for different values of the external applied field H_{ext}. Blue-white-red color scale: m_y component. (See **Vid06**).

5.4 Out-of-plane magnetic field

5.4.1 Low PMA sample

The OOP magnetization and hysteresis curves for the sample with low PMA are given in Fig. 5.11. The agreement with the experimental measurements is not perfect and could be enhanced by adjusting some parameters like the thickness or the Q value. However, the shape is precisely the same as in the measurements, which indicates that the reversal mechanism is correctly modeled. The curve for the initial magnetization is not visible because it coincides with the straight hysteresis curve.

The OOP magnetization mechanism for the sample with low PMA is illustrated in Fig. 5.12. Starting from a maze pattern at 0 T, when the applied field increases, the domains with a magnetization in the direction of the applied field expand, at the expense of the domains in the reverse direction. The domains in the reverse direction then start to divide into cylindrical domains (or "bubble domains") [25]. Those cylindrical domains then decrease in size until they completely disappear at saturation at $\mu_0 H_{\text{sat}} = 0.86$ T.

The OOP reversal mechanism is presented in Fig. 5.13. Starting from saturation at 1 T, reverse cylindrical domains start to nucleate at the nucleation field $\mu_0 H_{\text{n}} \simeq 0.69$ T. The reverse domains do not nucleate at $\mu_0 H_{\text{sat}} = 0.86$ T because of a potential barrier that prevents the nucleation. Nucleation is only possible when the field is decreased until 0.69 T. This is the origin of the hysteresis at the two extremities of the loop.

The nucleation of the reverse domains induces some little jumps in the curve. When a certain amount of domains have nucleated, no more domains nucleate and the existing domains start to grow, which results in a straight line in the hysteresis loop. The growth of the reverse domains gives rise to a maze patter around 0 T. When the field is increased in the reverse direction, the domains in the direction of the previous saturated state decrease in size, then divide in bubbles and disappear, resulting in a linear variation of the magnetization until saturation in the reverse direction [25, 26].

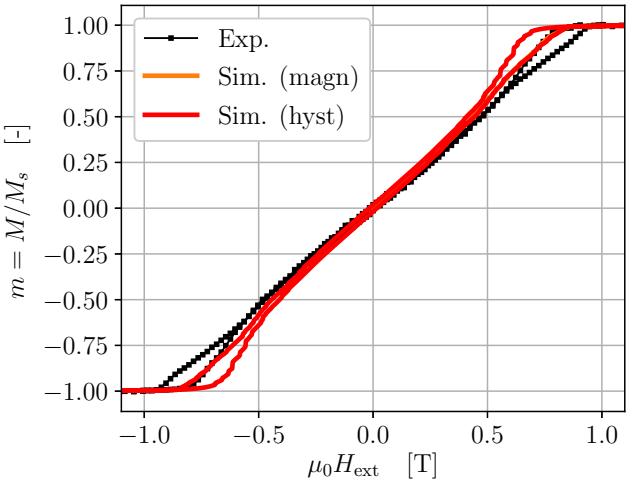

Figure 5.11: Out-of-plane magnetization and hysteresis curves for the sample with low PMA with $\sigma_{K_u} = 5\%$ and $\sigma_{\mathbf{e}_u} = 5°$ compared to the experimental curve. Experimental data shared by A.S. [8].

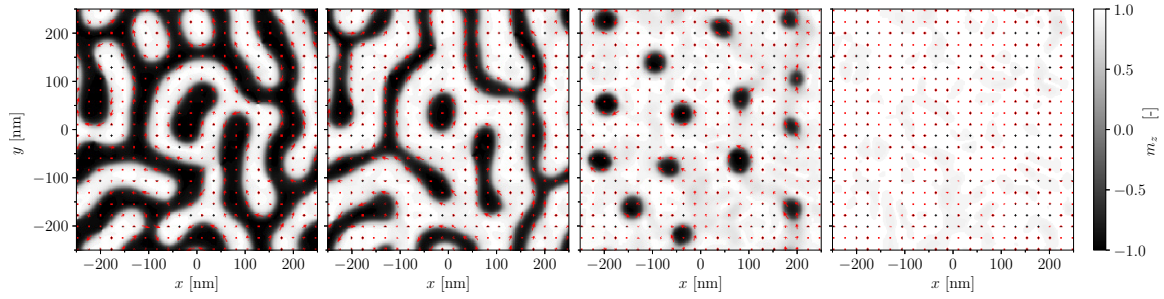

(a) $\mu_0 H_{\text{ext}} = 0\text{T}$ **(b)** $\mu_0 H_{\text{ext}} = 0.333\text{T}$ **(c)** $\mu_0 H_{\text{ext}} = 0.666\text{T}$ **(d)** $\mu_0 H_{\text{ext}} = 1\text{T}$

Figure 5.12: Magnetization mechanism from the equilibrium configuration to OOP saturation for the sample with low PMA. Top view at mid-thickness for different values of the external applied field H_{ext}. Gray color scale: OOP component m_z. Red arrows: IP components. (See **Vid07**).

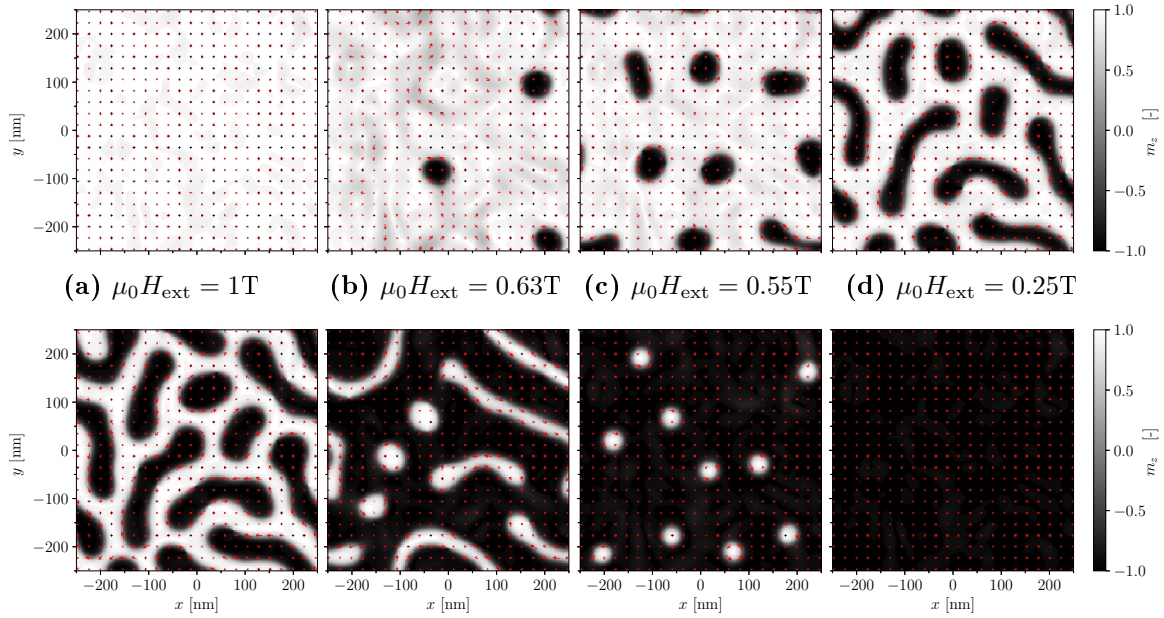

(a) $\mu_0 H_{\text{ext}} = 1\text{T}$ **(b)** $\mu_0 H_{\text{ext}} = 0.63\text{T}$ **(c)** $\mu_0 H_{\text{ext}} = 0.55\text{T}$ **(d)** $\mu_0 H_{\text{ext}} = 0.25\text{T}$

(e) $\mu_0 H_{\text{ext}} = 0\text{T}$ **(f)** $\mu_0 H_{\text{ext}} = -0.5\text{T}$ **(g)** $\mu_0 H_{\text{ext}} = -0.75\text{T}$ **(h)** $\mu_0 H_{\text{ext}} = -1\text{T}$

Figure 5.13: OOP reversal mechanism for the sample with low PMA. Top view at mid-thickness for different values of the external applied field H_{ext}. Gray color scale: OOP component m_z. Red arrows: IP components. (See **Vid08**).

5.4.2 High PMA sample

In the case of high PMA, a distribution of anisotropy even as high as $\sigma_{K_\text{u}} = 5\%$ and $\sigma_{\mathbf{e}_\text{u}} = 5°$ is not enough to enable the nucleation of reverse domains. Due to the high anisotropy energy, the potential barrier for the nucleation is too high, and the configuration stays stuck in the saturated state until it switches to the saturated state in the reverse direction. Another type of defect is therefore needed for this simulation. Since holes have been observed in the samples of A. Stellhorn [8], it is chosen to introduce holes in the simulation, which will act as nucleation points.

The first part of the OOP reversal curve is given in Fig. 5.14 with 3 holes for different hole diameters D_{holes}. Diameters below 6 nm are too small to enable nucleation. One can also see that when increasing D_{holes} from 6 to 12 nm, the nucleation field increases. Indeed, the larger the holes, the smaller the potential barrier for nucleation, which results in a larger nucleation field. It is chosen to use holes with $D_{\text{holes}} = 10$ nm because the nucleation field does not increase drastically for higher diameters. Even though after the nucleation the curve from the simulations coincides with the measurements, one observes that during the nucleation, the agreement is not perfect. The nucleation mechanism is therefore not exactly modeled, but the growth of the reverse domains once nucleated is close to the experiments.

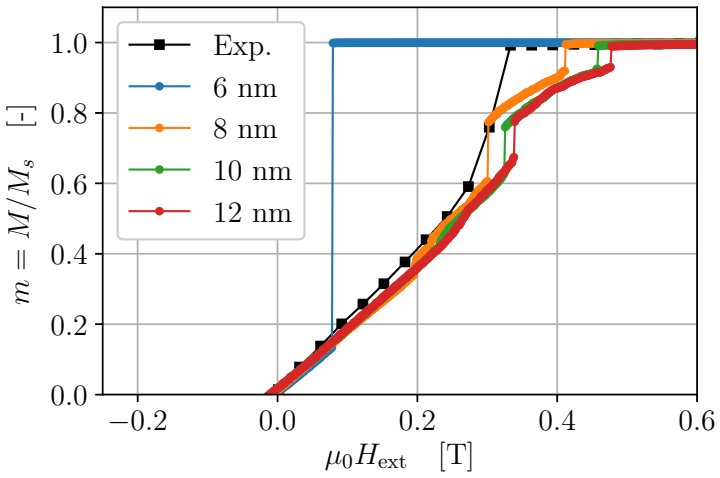

Figure 5.14: OOP reversal curves for the sample with high PMA with 3 holes for different hole diameters D_{holes}. Experimental data shared by A.S. [8].

The OOP reversal for different numbers of 10nm-diameter holes is illustrated in Fig. 5.15. The holes are positioned with a uniform probability in the simulation domain using a random-number generator. The top view is given at $\mu_0 H_{\text{ext}} = 0.34$ T and $\mu_0 H_{\text{ext}} = 0$ T for 1 to 50 holes. At 0.34 T, for 1 to 5 holes, one can see that reverse domains have nucleated at each defect. By increasing the number of reverse domains, the total energy of the domain walls increases, but the demagnetizing energy can be reduced over the whole sample. For a higher number of holes, one can see that reverse domains do not grow from all the defects, with approximately the same number for 20 and 50 holes. Increasing the number of reverse domains would decrease the demagnetizing energy more uniformly over the sample, but the increase of domain wall energy would be too high.

At remanence (0 T), for 1 hole, one can see that multiple concentric domains have grown from the same defect. This behavior is due to the high symmetry resulting from the unique hole with periodic boundary conditions in the IP directions. For 3 and 5 holes, the reverse domains grow, first in a cylindrical shape, then in elongated shapes when they come closer to each other. The elongated shapes enable to obtain domains with widths roughly uniform over the whole sample, giving rise to a maze pattern close to the one observed in the experiments. For 20 to 50 holes, the reverse domains grow in a more "bubble-like" shape, less elongated. This results from the larger number of reverse domains that already cover the sample in a uniform way, and the pinning from the defects where no reverse domains have grown.

Half of the OOP hysteresis curve for different numbers of holes is shown in Fig. 5.16. For 0 holes, the behavior corresponds to a hard ferromagnet, where the magnetization

is stuck in the saturated state until it switches directly to the saturated state in the reverse direction. Adding one hole is sufficient to drastically decrease the hysteresis by enabling the nucleation of a reverse domain. Increasing the number of holes to 50 changes the shape of the curve. For 50 holes, the nucleation field is the highest, and the curve is made of a large number of small jumps corresponding to the nucleation of multiple reverse domains. Once the nucleated domains start to grow, the curve is roughly the same in all the cases, but the remanence and coercivity are slightly larger for a large number of holes. This is probably due to the number of reverse domains and the pinning at the defects that hardens the magnet compared to the maze pattern. Finally, at the end of the reversal, close to saturation, the curve for 50 holes is once again made of a large number of small jumps resulting in a roughly linear curve. On the contrary, for a smaller number of holes, the curve deviates from the linear behavior and is made of a few large jumps. This is due to the pinning of the domains in the direction of the previous saturated state, as can be seen in Fig. 5.19f. The pinning at the small number of defects produces elongated domains, that will disappear in several jumps. This behavior is different from the one observed for the sample with low PMA, where the cylindrical domains gradually decrease in size, resulting in a linear behavior of the magnetization. When the elongated domains are pinned between a larger number of holes, they can disappear fragment by fragment, resulting in a large number of small jumps and a close to linear behavior in the hysteresis curve.

The initial OOP magnetization curve and the complete hysteresis for 3 holes are compared to the experimental measurements in Fig. 5.17. The agreement is not perfect, but the mechanisms taking place in the real sample can be understood considering the previous discussion. First, the large hysteresis at the two extremities of the curve is due to the energy barrier for the nucleation of reverse domains. Then, the linear behavior until saturation in the reverse direction is due to, first, the growth of reverse domains towards a maze pattern, and then to the shrinking of the remaining domains in the direction of the previous saturated state. The deviation in the simulation is due to the pinning at the small number of defects. Finally, the hysteresis near 0 T is very small, with $M_\mathrm{r} \simeq 0.012 M_\mathrm{s}$ ($0.019 M_\mathrm{s}$ in the experiment) and $\mu_0 H_\mathrm{c} \simeq 10$ mT (6 mT in the experiment).

The initial magnetization and reversal mechanisms for the sample with 3 holes are illustrated in Figs. 5.18 and 5.19.

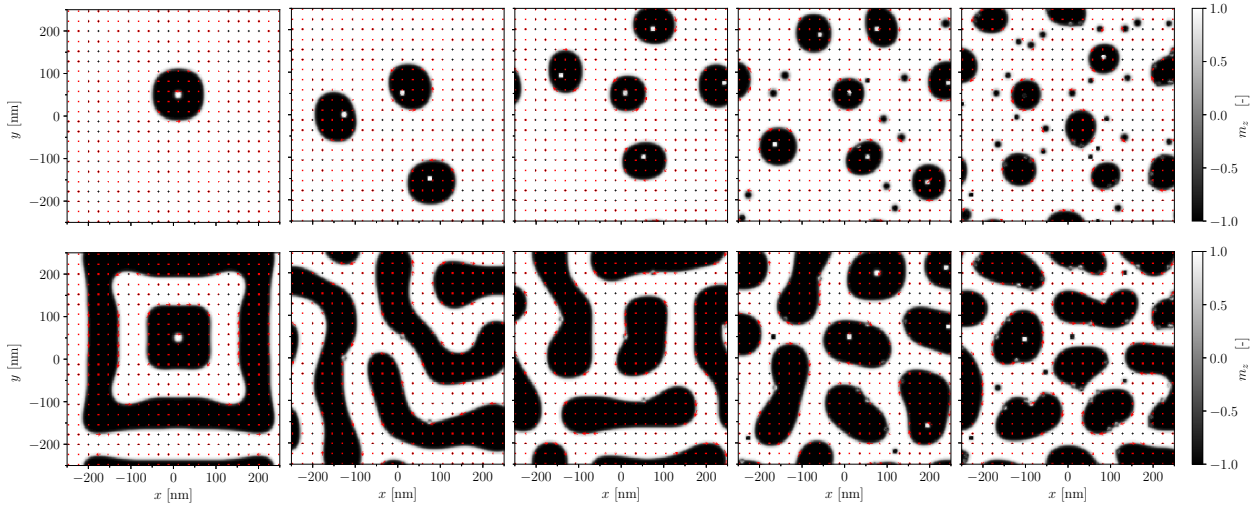

(a) 1 hole **(b)** 3 holes **(c)** 5 holes **(d)** 20 holes **(e)** 50 holes

Figure 5.15: Top view at mid-thickness during the OOP reversal at $\mu_0 H_{\text{ext}} = 0.34$ T (top) and $\mu_0 H_{\text{ext}} = 0$ T for different numbers of holes. All the holes have a diameter $D_{\text{holes}} = 10$ nm. Gray color scale: OOP component m_z. Red arrows: IP components.

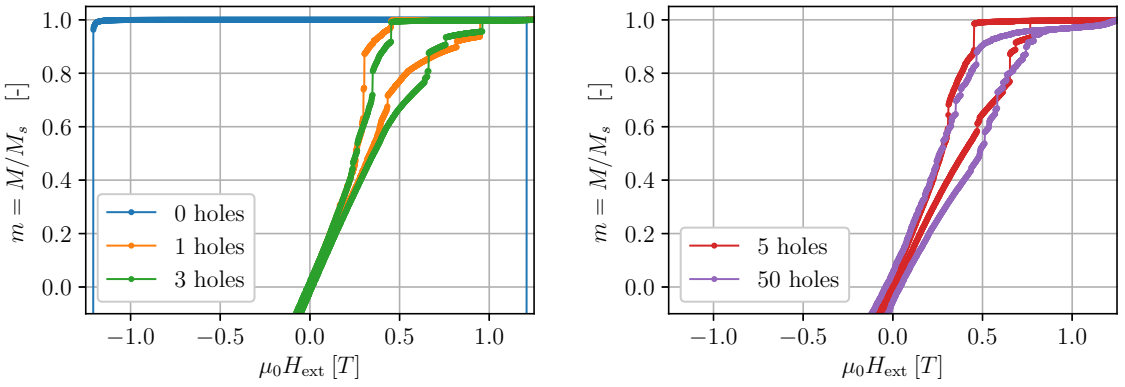

(a) **(b)**

Figure 5.16: OOP hysteresis curves for the sample with high PMA with different numbers of holes. All the holes have a diameter $D_{\text{holes}} = 10$ nm.

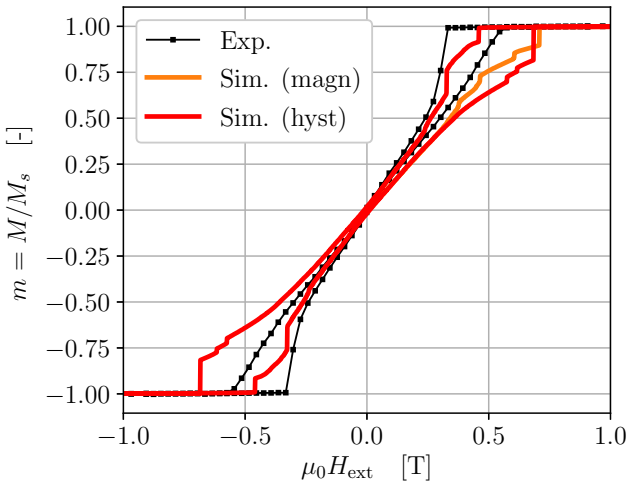

Figure 5.17: Out-of-plane magnetization and hysteresis curves for the sample with high PMA with $\sigma_{K_u} = 0.1\%$ and $\sigma_{\mathbf{e}_u} = 0.1°$ and 3 holes of 10 nm diameter compared to the experimental curve. Experimental data shared by A.S. [8].

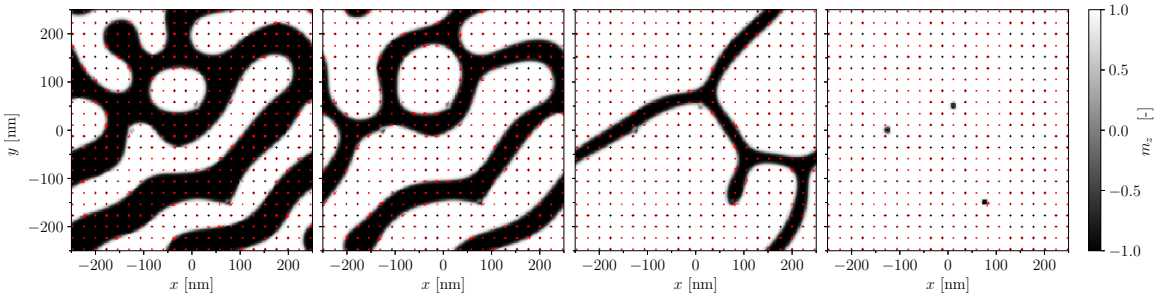

(a) $\mu_0 H_{\text{ext}} = 0\text{T}$ **(b)** $\mu_0 H_{\text{ext}} = 0.250\text{T}$ **(c)** $\mu_0 H_{\text{ext}} = 0.500\text{T}$ **(d)** $\mu_0 H_{\text{ext}} = 1\text{T}$

Figure 5.18: Magnetization mechanism from the equilibrium configuration to OOP saturation for the sample with high PMA. Top view at mid-thickness for different values of the external applied field H_{ext}. Gray color scale: OOP component m_z. Red arrows: IP components. (See **Vid09**).

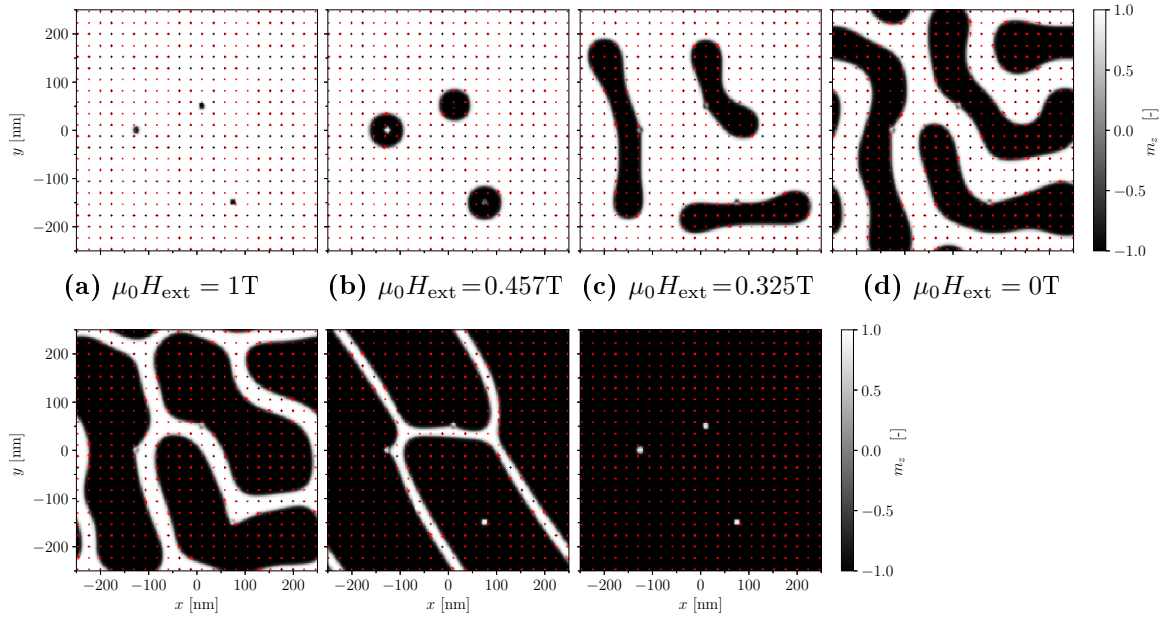

(a) $\mu_0 H_{\text{ext}} = 1\text{T}$ **(b)** $\mu_0 H_{\text{ext}} = 0.457\text{T}$ **(c)** $\mu_0 H_{\text{ext}} = 0.325\text{T}$ **(d)** $\mu_0 H_{\text{ext}} = 0\text{T}$

(e) $\mu_0 H_{\text{ext}} = -0.325\text{T}$ **(f)** $\mu_0 H_{\text{ext}} = -0.650\text{T}$ **(g)** $\mu_0 H_{\text{ext}} = -1\text{T}$

Figure 5.19: OOP reversal mechanism for the sample with high PMA. Top view at mid-thickness for different values of the external applied field H_{ext}. Gray color scale: OOP component m_z. Red arrows: IP components. (See **Vid10**).

5.5 Conclusion

The discussions in this Chapter provide explanations for the available hysteresis measurements on FePd thin films. Most importantly, defects are crucial for the reversal. The main results are reminded below.

The final hysteresis curves obtained by simulation for low and high PMA with the parameters of Table 5.1 are shown in Fig. 5.20. The agreement between the simulations and the measurements is not perfect, but good enough to understand the reversal mechanisms taking place in the real sample, as well as the origin of the hysteresis.

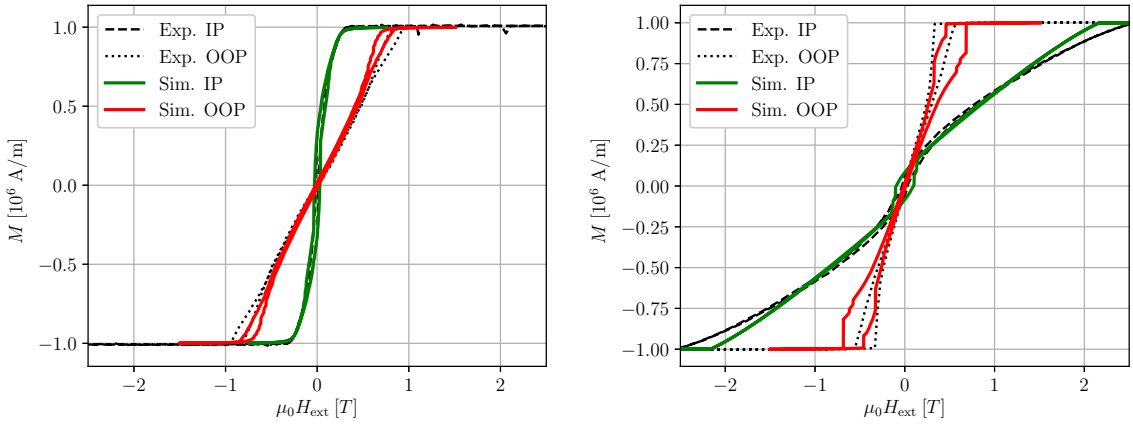

(a) Q=0.47 **(b)** Q=2.0

Figure 5.20: Final in-plane (IP) and out-of-plane (OOP) hysteresis loops for the sample with (a) low PMA and (b) high PMA, and comparison with experimental measurements. Experimental data from A.S. [8].

For both samples, the IP reversal mechanism is roughly the same, except that the curve is much steeper for low PMA. Starting from saturation in one direction, stripes with alternating OOP components gradually appear when the field decreases. This enables to decreases the anisotropy energy by increasing the OOP component at the expense of the IP component. Instead of changing uniformly within the sample, the OOP component oscillates between positive and negative values to decrease the demagnetizing energy, giving rise to the stripe pattern. At remanence, the OOP domains are separated by domain walls with an IP component in the direction of the previous saturated state, giving rise to a remanent magnetization and some hysteresis. When increasing the field in the reverse direction, the domain walls flip depending on the defects. Once all the walls have flipped, the stripe pattern gradually changes toward full saturation as the field is increased.

The OOP reversal mechanism is also comparable for the low and high PMA. Starting from saturation, when the field is decreased, domains nucleate at a field smaller than the field needed to saturate the sample, because of the energy barrier for the nucleation. For the sample of low PMA, the energy barrier is smaller and grains with an anisotropy distribution are enough to enable nucleation. For the sample with high PMA, the barrier is higher and holes are needed to enable nucleation. Once multiple reverse domains have nucleated, they grow and become elongated until they form a maze pattern at remanence. This results in a linear variation of the magnetization. Increasing the field in the reverse direction, the domains in the direction of the previous saturated state shrink and separate into cylindrical domains. Those cylindrical domains then shrink until they completely disappear, resulting in a linear variation

until saturation in the reverse direction.

The hysteresis is therefore due to the presence of energy barriers during the reversal mechanism. For the IP loop, the switching of the domain walls gives rise to some hysteresis around zero field. On the contrary, for the OOP loop, the energy barrier for the nucleation of reverse domains gives rise to some hysteresis at the extremities of the curve.

The exact choice of defects will affect the hysteresis curve by modifying the energy landscape. Adding some thermal fluctuations may help to jump over the energy barriers, but the mechanisms should remain the same.

Chapter 6

Chirality and link to neutron scattering

6.1 Introduction

In Chapter 4, the structure of the domain walls (DWs) between the out-of-plane (OOP) magnetic domains in thin films with perpendicular anisotropy has been studied. The domain walls have a Bloch structure in the middle of the thickness, where the magnetization rotates in planes parallel to the plane of the wall. Néel closure domains are formed at the top and bottom surfaces, where the magnetization rotates in a plane perpendicular to the plane of the wall. The direction of the magnetization in the Néel closure domains (or "Néel caps") is imposed by the demagnetizing field. It is oriented such that it closes the loop between the OOP domains, reducing the demagnetizing energy. On the contrary, the orientation of the magnetization in the Bloch part depends on the magnetic history and the domain pattern, as explained in Chapter 5. During the in-plane reversal, stripes are formed and the magnetization in all the Bloch walls is in the direction of the previous in-plane saturated state, before they switch when the applied field increases in the reverse direction. During the out-of-plane reversal, after cylindrical domains have nucleated and grown, a maze pattern is formed. The direction of the magnetization in the Bloch walls has not been analyzed in this case and is the topic of this chapter.

As illustrated in Fig. 5.19, when a domain nucleates at a defect, the magnetization in the Bloch wall forms a closed loop around the reverse domain, either in the clockwise (CW) or the counterclockwise (CCW) direction. Since all the energy terms are symmetric (exchange, anisotropy, demagnetizing energy), it is expected that none of those two directions is preferred, leaving them equiprobable.

The clockwise or counterclockwise direction of the domain walls is directly linked to

the chirality of the Bloch wall. Chirality refers here to the handedness of the helix formed by the Bloch wall and it should be noted that the handedness of the helix does not depend on the direction in which one looks at it. A right-handed helix is right-handed independently of the position of the observer. While one would expect that the CW and CCW direction are equiprobable, and that therefore the number of right and left-handed DWs should be equal, it seems that this is not the case in experimental observations. More precisely, neutron scattering measurements performed in [8] suggest that the average chirality of the domain walls is not zero. This chapter aims to understand how this can be deduced from neutron scattering measurements, as well as the possible origins of those observations.

In Section 6.2, the Grazing-Incidence Small-Angle Neutron Scattering (GISANS) measurement technique is presented. Results from [8] are shown and we explain how one can deduce from them information on the chirality of the domain walls. In Section. 6.3, another scattering technique, namely Magnetic Small-Angle Neutron Scattering (MSANS) is presented. A simple *Python* code has been written to compute the results of MSANS for the magnetic configurations obtained with *MuMax3*. The results for a stripe and a maze configuration are then analyzed. In Sections 6.4 and 6.5, two hypotheses to explain the experimental observations are investigated. The first one is that they result from statistical fluctuations of a non-chiral system. The second one is that there exists a chiral interaction.

6.2 GISANS measurements

6.2.1 Unpolarized GISANS

Grazing-Incidence Small-Angle Neutron Scattering (GISANS) is a measurement technique where a neutron beam, well collimated in both directions perpendicular to the beam, impinges the surface of the sample with a very small angle and is scattered to be collected on a two-dimensional detector. The small incidence angle α_i enables one to be close to the total reflection and therefore increases the sensitivity to the layer. By using a beam well-collimated in both directions perpendicular to the incident wavevector $\mathbf{k}_i$, depth-resolved information on the lateral magnetic profiles can be retrieved. The typical geometry of a GISANS measurement is depicted in Fig. 6.1 (in reality, this figure illustrates the geometry for Grazing-Incidence Small-Angle X-ray Scattering, or GISAXS, but the principle is the same). The incident wave vector $\mathbf{k}_i$ impinges the surface at an angle α_i. The X direction coincides with the projection of $\mathbf{k}_i$ on the surface of the sample. The Y direction is the in-plane direction perpendicular to X, and Z is the out-of-plane direction. The reflected neutrons have a wavevector $\mathbf{k}_f$, which direction is defined by the angles α_f and θ. With the assump-

tion that the angles α_i, α_f and θ are small, the scattering wavevector $\mathbf{q} = \mathbf{k}_f - \mathbf{k}_i$ is given by

$$q_X = k(\alpha_i^2 - \alpha_f^2 - \theta^2)/2, \quad q_Y = k\theta, \quad q_Z = k(\alpha_i + \alpha_f), \quad \text{with } k = \frac{2\pi}{\lambda} \tag{6.1}$$

where λ is the wavelength of the neutron. Each pixel on the detector is defined by the values of α_f and θ, or equivalently by q_Y and q_Z. A map of the scattered neutron intensity as a function of q_Y and q_Z can therefore be drawn. On this map, the line for which $\alpha_f = \alpha_i$ is called the GISANS line and corresponds to the neutrons reflected in a specular manner. Any domain pattern with a periodicity in the y direction gives rise to scattering intensities in q_Y along the GISANS line. The intensities above or below this line correspond to off-specular scattering.

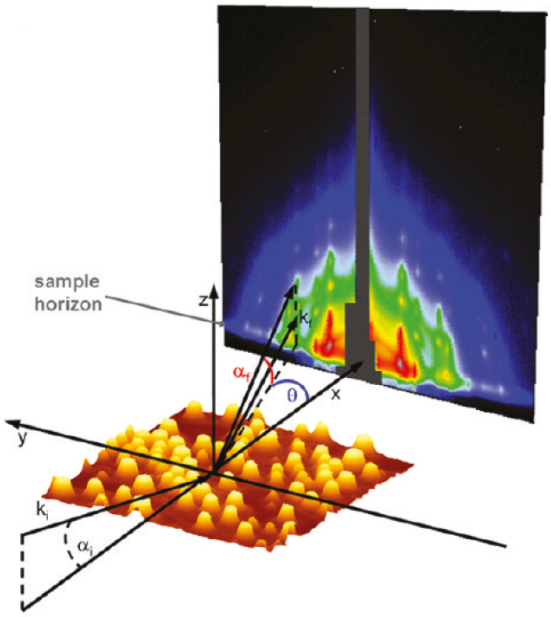

Figure 6.1: Geometry of a GISAXS experiment (similar to a GISANS experiment). Figure taken from [40].

An example of GISANS measurements for a sample with a stripe pattern is shown in Fig. 6.2. The direct beam produces a spot at $q_Y = q_Z = 0$ nm^{-1} whose intensity is reduced with a beam stop. On the GISANS line (at $q_Z = 0.165$ nm^{-1}), spots can be observed for $q_Y \neq 0$ nm^{-1} when the sample is oriented with the stripes along X, yielding a finite period of the pattern in the Y direction. On the contrary, no spots for $q_Y \neq 0$ nm^{-1} are observed when the stripes are aligned with Y because it yields an infinite period in the Y direction. A specular spot at $q_Y = 0\,\text{nm}^{-1}$, $q_Z = 0.165$ nm^{-1} is present in both cases.

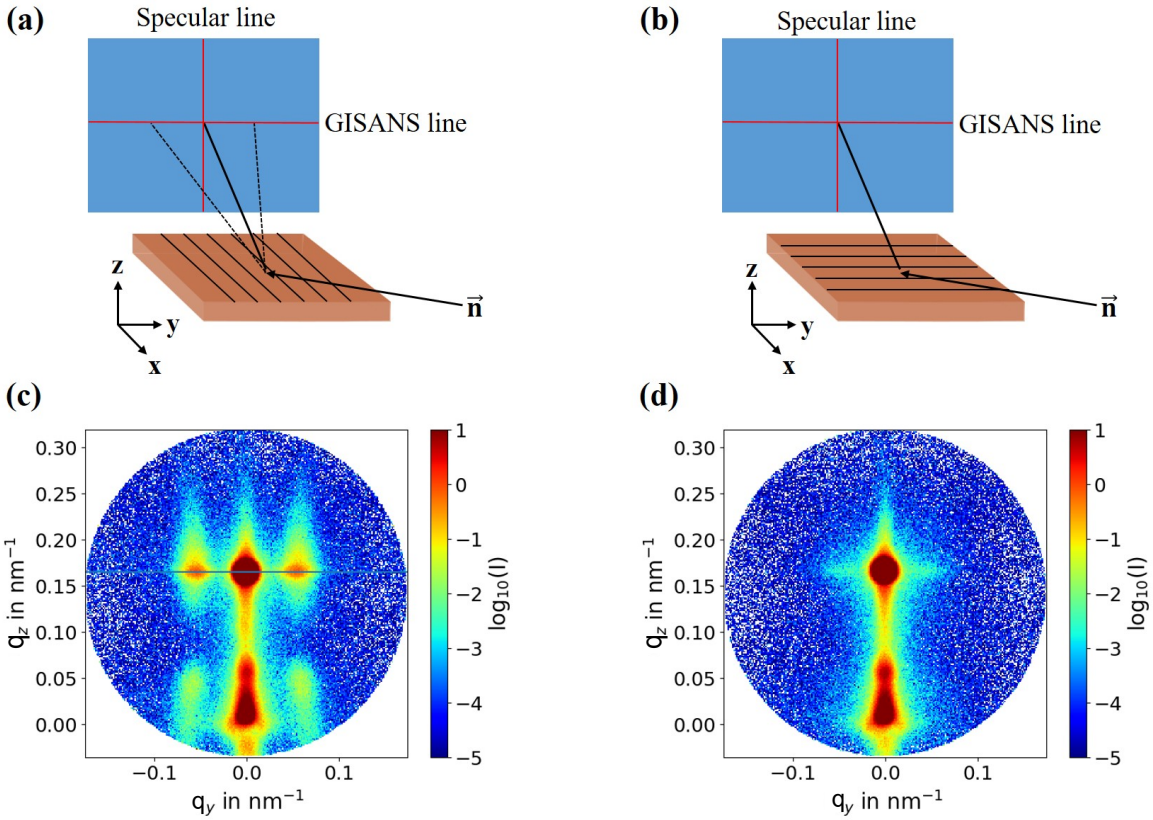

Figure 6.2: Schematic of a sample with magnetic stripes aligned along X (a) or along Y (b). (c,d) $q_Y - q_Z$ maps of a GISANS measurement corresponding to the geometry (a) and (b) respectively. The horizontal line at $q_Z = 0.165$ nm^{-1} is the GISANS line. Figure adapted from [8].

6.2.2 Polarized GISANS

GISANS measurement can also be combined with polarization analysis. Since neutrons are fermions, they have a spin $s = 1/2$ and only 2 spin states are possible ($2s+1 = 2$), either up (+) or down (-) relative to a guide field $\mathbf{H}_0$. By using a polarizer and a spin flipper before the sample, as well as a spin analyzer after the sample, 4 channels can be distinguished: the Non-Spin-Flip (NSF) channels I^{++} and I^{--}, and the Spin-Flip (SF) channels I^{+-} and I^{-+}, where the exponents correspond to the spin state of the incident neutrons and the scattered neutrons, respectively. The polarization axis $\mathbf{P}$ is always parallel to the guide field $\mathbf{H}_0$ which is used to maintain the direction of the spin and the polarization of the neutron beam. It can be shown that the NSF channels are sensitive to the nuclear fluctuations and the magnetization $\mathbf{M}^{//}$ parallel to the guide field $\mathbf{H}_0$ whereas the SF channels are sensitive to the magnetization $\mathbf{M}^{\perp}$ perpendicular to $\mathbf{H}_0$. Note that the intensity (or cross section) for unpolarized GISANS simply corresponds to $I = I^{++} + I^{--} + I^{+-} + I^{-+}$.

Polarized GISANS measurements have been performed in A. Stellhorn's thesis. The sample exhibited high PMA, had been saturated with an OOP field and then the field was ramped down to 2.6 mT and used as guide field. By using a polarization guide field perpendicular to the sample surface, the NSF channels are sensitive to the OOP domains whereas the SF channels are sensitive to the IP components, namely the closure domains and the Bloch walls. Note however that in reality, the polarization was not perfectly perpendicular to the sample, making a certain angle α with the normal to the surface. The results for the 4 channels are shown in Fig. 6.3. In the NSF channels, the GISANS peaks are hidden due to surface and interface roughness whereas in the SF channels, they can be clearly distinguished. Moreover, there is an asymmetry between the intensity of the right and the left peak, termed spin-flip splitting (SFS). For I^{+-} the right peak is more intense than the left, and the opposite behavior is observed for I^{-+}.

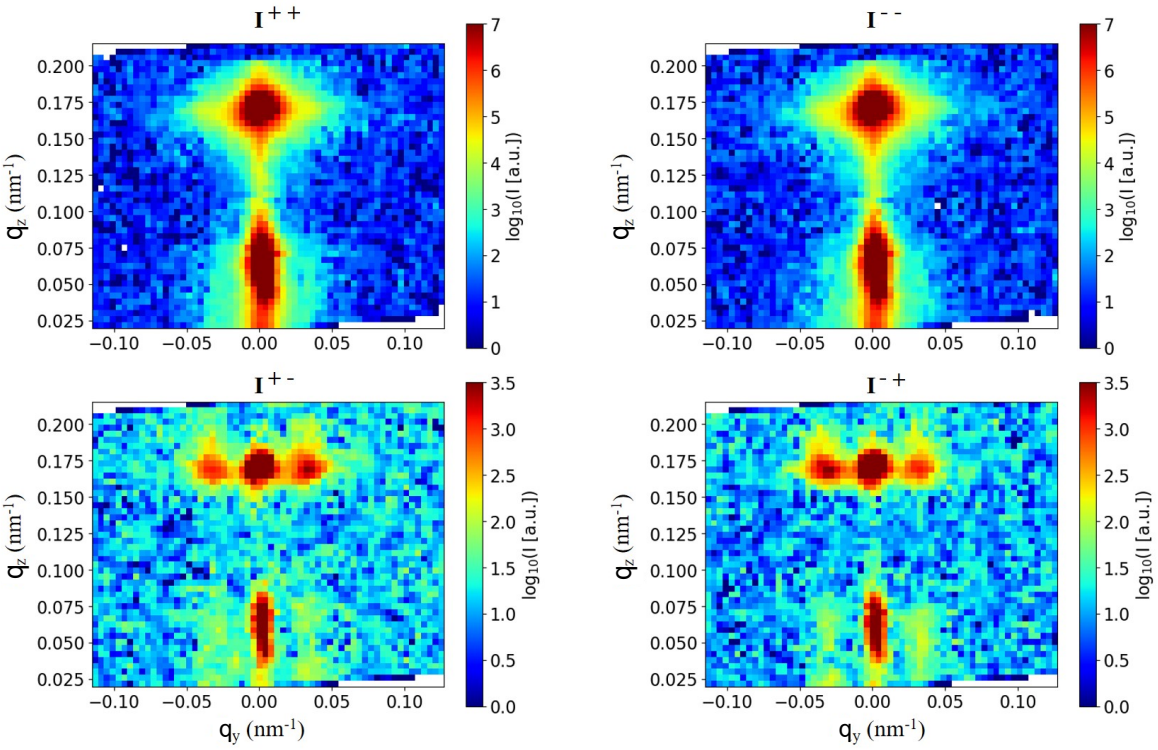

Figure 6.3: $q_Y - q_Z$ maps of the four channels of a polarized GISANS measurement for a sample with high PMA, exhibiting a maze pattern at nearly zero field after having been saturated out-of-plane. Figure adapted from [8].

6.2.3 Spin-flip splitting and chirality

The spin-flip splitting (SFS) in the polarized neutron scattering measurement is linked to the chirality of the magnetic configuration in the sample. In magnetism, chirality is linked to the cross product $\mathbf{S}_1 \times \mathbf{S}_2$ between two adjacent spins $\mathbf{S}_1$ and $\mathbf{S}_2$. The chirality vector is defined as $\mathbf{c} = \frac{\mathbf{S}_1 \times \mathbf{S}_2}{\|\mathbf{u}_{12}\|}$ where $\mathbf{u}_{12}$ is the vector between the lattice sites 1 and 2. In the case of the helix structure, taking $\mathbf{u}_{12}$ in the propagation direction of the helix, we define the helicity $p = \frac{\mathbf{S}_1 \times \mathbf{S}_2}{\|\mathbf{u}_{12}\|} \cdot \frac{\mathbf{u}_{12}}{\|\mathbf{u}_{12}\|}$. The helix is right-handed for $p > 0$ and left-handed for $p < 0$, and $\|p\|$ corresponds to the frequency of the helix. In the case of a planar Bloch wall, the structure is not exactly a helix since the rotation angle does not vary linearly. The value of p therefore changes through the Bloch wall, but its sign still indicates the handedness.

It is shown in [41] and [42] that an asymmetric contribution to the cross section is induced by the helix structure if $\mathbf{c}$ (the chirality vector in the direction of the helix propagation direction) has a component in the direction of the polarization axis $\mathbf{P}$. More precisely, when $\mathbf{q} \parallel \mathbf{c}$, the contribution is of the form

$$(\hat{\mathbf{q}} \cdot \mathbf{P})(n_L - n_R) \tag{6.2}$$

with $\hat{\mathbf{q}}$ the unit scattering vector, and n_L and n_R the population numbers of the left and right-handed helices. For a sample with Bloch walls between the out-of-plane domains, $\mathbf{c}$ is in the plane of the sample. On the GISANS line, $\mathbf{q}$ is also in the plane, and spin-flip splitting will be observed only if the $\mathbf{P}$ has a component in the plane of the sample (i.e. the direction of propagation vector of the helix of the Bloch walls). This was indeed the case in the measurements of Fig. 6.3, where $\mathbf{P}$ was not perfectly in the Z direction, having a tilt α in the Y direction.

The spin-flip splitting observed in Fig. 6.3 was reproduced in [8] by simulations of GISANS measurements using the Distorted Wave Born Approximation (DWBA) [43]. The simulations were based on a simplified model for the domains and domain walls structure, with only right-handed Bloch walls. SFS was then observed only if $\mathbf{P}$ was tilted in the Y direction.

In order to better understand the origin of the spin-flip splitting, a *Python* code has been written to obtain the cross section by Magnetic Small-Angle Neutron Scattering (MSANS) for the magnetic configurations obtained by micromagnetic simulations. This is discussed in the next section.

6.3 MSANS simulations

The formalism of the DWBA based on quantum mechanical perturbation theory for simulations of GISANS is complicated to implement. On the contrary, the cross section for Magnetic Small-Angle Neutron Scattering (MSANS), *i.e.* transmission neutron scattering, is much easier to compute since it is a combination of the Fourier transforms (FT) of the 3 components of the magnetization. The typical MSANS geometry corresponds to a neutron beam directed perpendicular to the sample surface (normal incidence), with a 2-dimensional detector after the sample. The polarization axis is either perpendicular or parallel to the neutron beam. In order to obtain results comparable to the profile on the GISANS line, the MSANS cross section will be computed with an in-plane neutron beam in the X direction, with a polarization axis perpendicular to the beam. Performing transmission neutron scattering in the plane of a thin film is not realistic. It is indeed unlikely that neutrons can transmit through the whole width of the sample together with a small scattering angle. It is however still interesting because it will give results comparable to those of Fig. 6.3. The formalism used to compute the MSANS cross section is explained in Section 6.3.1. The *Python* code is described in Section 6.3.2 and the results are presented in Sections 6.3.3 and 6.3.4.

6.3.1 Formalism for MSANS

The formalism used to compute the MSANS cross section is the one reviewed by Mühlbauer *et al.* [44] with a guide field for the polarization perpendicular to the neutron beam ($\mathbf{H}_0 \perp \mathbf{k}_i$). This formalism is adapted here to take into account a tilt of the polarization axis.

Three systems of coordinates are defined in Fig. 6.4. (x, y, z) are the axes linked to the sample, with x and y the in-plane directions and z the out-of-plane direction. (X, Y, Z) are axes parallel to (x, y, z), but where X is the direction of the neutron beam, which can be along any of the 3 principal axis of the sample. In order to enable a tilt of the polarization axis with respect to Z, a third system of axes (x', y', z') is defined by a rotation of an angle α around the X axis.

The Fourier transform $\tilde{\mathbf{M}}(q_X, q_Y, q_Z)$ of the magnetization $\mathbf{M}(X, Y, Z)$ (from which the mean value has been subtracted) is computed in the axes (X, Y, Z) and defined as

$$\tilde{\mathbf{M}}(q_X, q_Y, q_Z) = \frac{1}{(2\pi)^{3/2}} \int\int\int \mathbf{M}(X, Y, Z) \exp\left[-i(q_X X + q_Y Y + q_Z Z)\right] \mathrm{d}X \mathrm{d}Y \mathrm{d}Z. \tag{6.3}$$

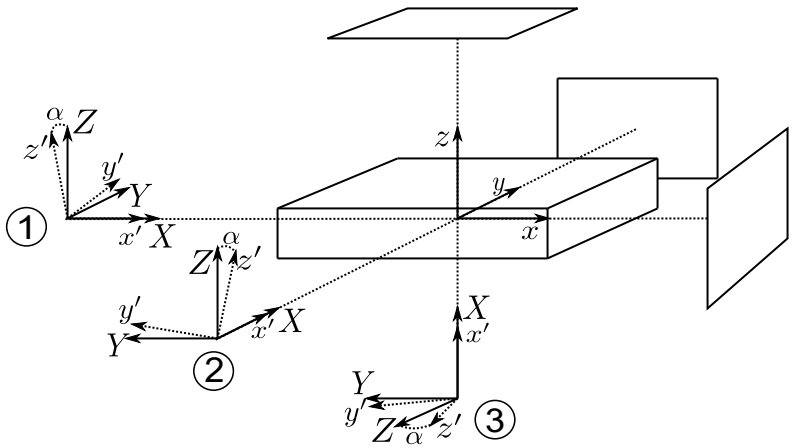

Figure 6.4: Geometry for the MSANS formalism. (x, y, z) are the principal axes of the sample. The neutron beam (doted lines) is either in the x (1), y (2) or the z-direction (3). (X, Y, Z) are parallel to (x, y, z) but with X aligned with the neutron beam. (x', y', z') are obtained by a rotation of an angle α about X. The polarization axis is along z'. The three rectangles represent the 2D detectors.

The components of $\mathbf{M}$ in the (x', y', z') axes are obtained from the components in the (X, Y, Z) axes with

$$\begin{aligned} M_{x'} &= M_X, \\ M_{y'} &= M_Y \cos\alpha + M_Z \sin\alpha, \\ M_{z'} &= -M_Y \sin\alpha + M_Z \cos\alpha \end{aligned} \tag{6.4}$$

and the same holds for the components of the Fourier transform $\tilde{\mathbf{M}}$.

In small-angle scattering, the component of $\mathbf{q}$ along the incident neutron beam is neglected, *i.e.* $q_X = q_{x'} = 0$. The scattering vector is then defined by its norm q and the angle θ it makes with the z' axis, such that

$$\mathbf{q} = \begin{bmatrix} q_{x'} \\ q_{y'} \\ q_{z'} \end{bmatrix} = q \begin{bmatrix} 0 \\ \sin\theta \\ \cos\theta \end{bmatrix}. \tag{6.5}$$

The cross section depends only on the component of the magnetization that is perpendicular to $\mathbf{q}$. It is therefore useful to define the magnetic-interaction vector [44]

$$\mathbf{Q} = \hat{\mathbf{q}} \left[\hat{\mathbf{q}} \cdot \tilde{\mathbf{M}}(\mathbf{q}) \right] - \tilde{\mathbf{M}}(\mathbf{q}) = \begin{bmatrix} Q_{x'} \\ Q_{y'} \\ Q_{z'} \end{bmatrix} = \begin{bmatrix} -\tilde{M}_{x'} \\ -\tilde{M}_{y'} \cos^2\theta + \tilde{M}_{z'} \sin\theta\cos\theta \\ \tilde{M}_{y'} \sin\theta\cos\theta - \tilde{M}_{z'} \sin^2\theta \end{bmatrix}. \tag{6.6}$$

Neglecting the nuclear scattering, the non-spin-flip (NSF) cross sections $\frac{\mathrm{d}\Sigma^{++}}{\mathrm{d}\Omega}$ and $\frac{\mathrm{d}\Sigma^{--}}{\mathrm{d}\Omega}$ are given by [44]

$$\frac{\mathrm{d}\Sigma^{\pm\pm}}{\mathrm{d}\Omega} \sim |Q_{z'}|^2 \tag{6.7}$$

whereas the spin-flip (SF) cross section $\frac{\mathrm{d}\Sigma^{+-}}{\mathrm{d}\Omega}$ and $\frac{\mathrm{d}\Sigma^{-+}}{\mathrm{d}\Omega}$ are

$$\frac{\mathrm{d}\Sigma^{\pm\mp}}{\mathrm{d}\Omega} \sim |Q_{x'}|^2 + |Q_{y'}|^2 \pm 2\Im\left\{Q_{x'}Q_{y'}^*\right\} \tag{6.8}$$

where $\Im\{\cdot\}$ denotes the imaginary part and $(\cdot)^*$ the complex conjugate. One can see that the component $Q_{z'}$ gives rise to NSF scattering whereas the components $Q_{x'}$ and $Q_{y'}$ give SF scattering.

6.3.2 Python code for MSANS

The *Python* code *msans.py* computes the MSANS cross section for the configurations obtained by micromagnetic simulations with *MuMax3*. It is available on the following **link** by downloading the entire "msans" folder. The cross section for different simulations and different parameters can then be computed by changing the values in the "User choices" part.

The beam axis can be chosen to be in either the x, y or z direction. The α angle can also be varied. The polarization is along the Z axis for $\alpha = 0$, along the Y axis for $\alpha = \pi/2$ and tilted for any intermediate value. For the computation of the 3D Fourier transforms, it can be chosen, for each direction x, y and z, to either consider a periodic signal (which corresponds to repeating the simulation box in that direction), or to consider a signal on a compact domain given by the simulation box. The second option is implemented using zero-padding. The periodic condition seems a good choice for the x and y directions, whereas the compact domain seems appropriate for the z direction (finite thickness). Note however that performing MSANS in the plane of a thin film is not realistic. The results obtained in this case will therefore only be a mean to understand the GISANS measurements, and the two options for the Fourier transforms in the z direction must be tested.

Finally, it can be chosen to compute the cross sections for the 3-dimensional sample (in the $q_Y - q_Z$ plane) or for a z-slice of the sample (as a function of q_Y only). The second option enables one to select one slice along the thickness of the sample and to consider that the configuration is independent of z in order to ignore the effect of the fluctuations in that direction.

6.3.3 Results for a stripe pattern

Let us first analyze the results in the case of a simple stripe pattern as shown in Fig. 6.5. This pattern is obtained for a sample with $Q = 2.17$ and $d = 54$ nm during the in-plane reversal at remanence ($\mu_0 H_{\text{ext}} = 0$ T). The stripes are nearly perfect in this case, contrary to the simulations of Chapter 5, because only 3 holes are used as defects, without any anisotropy distribution. The pattern has a period $P = 2w \simeq 71.4$ nm in the x direction (where w is the domain width). As can be seen in Fig. 6.5b, the magnetization in all the Bloch walls is in the same direction. This results in a succession of left and right-handed walls, with the same amount of each. Since adjacent walls have always opposite chiralities, they are said to be heterochiral and the average chirality is exactly zero.

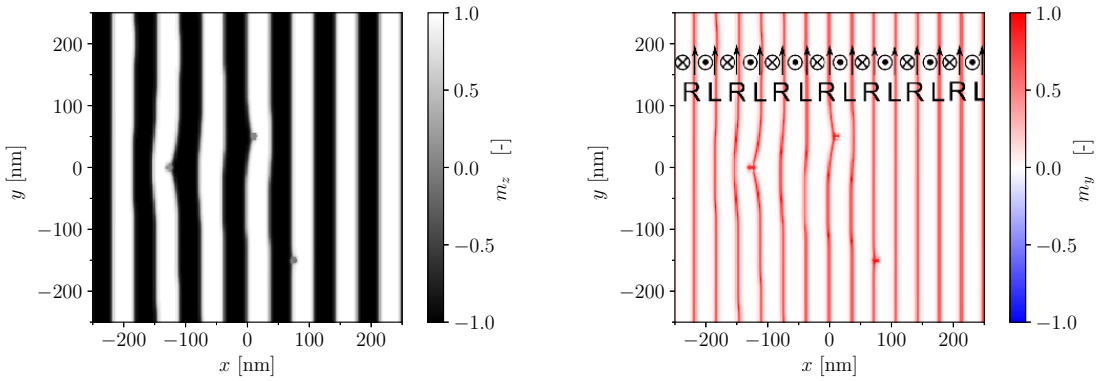

(a) m_z **(b)** m_y

Figure 6.5: Top view at mid-thickness of a sample with $Q = 2.17$ and $d = 54$ nm during the in-plane reversal, at remanence. The only defects are three holes of 10 nm in diameter. (a) OOP component m_z with a gray color scale revealing the domains. (b) IP component m_y with a blue-white-red color scale revealing the domain walls (DWs). The direction of the magnetization in the domains and the walls is indicated in black. R, L: right and left-handed DWs.

The MSANS cross section for a neutron beam in the z direction with $\alpha = 0$ (*i.e.* $\mathbf{P} \parallel \hat{\mathbf{Z}} = -\hat{\mathbf{y}}$) are shown in Fig. 6.6. The NSF channel is only sensitive to the magnetization with a component parallel to the polarization. It corresponds to the magnetization into the plane of the sample in this case. Since the domain walls are all in the same direction, the m_y component has a period $P/2 = w \simeq 35.7$ nm in the direction perpendicular to the polarization $\mathbf{P}$ (q_Y). This gives rise to two peaks at $q_Y = \pm 2\pi/35.7 \simeq 0.18$ nm^{-1} for the NSF channel. On the contrary, the SF channels are sensitive to the magnetization perpendicular to the polarization. The OOP domains, with a period $P = 2w \simeq 71.4$ nm in the q_Y direction, give rise to peaks at $q_Y = \pm 2\pi/71.4 \simeq 0.09$ nm^{-1}.

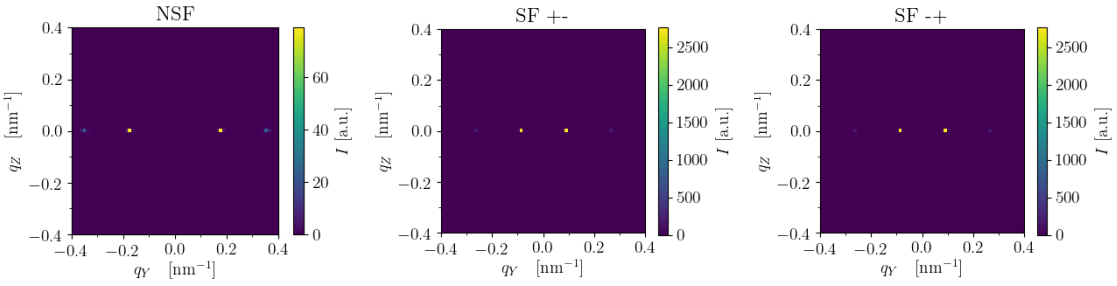

(a) **(b)** **(c)**

Figure 6.6: MSANS cross sections for the sample of Fig. 6.5 with a stripe pattern for a beam in the z direction with $\alpha = 0$. (a) $\frac{d\Sigma^{\pm\pm}}{d\Omega}$, (b) $\frac{d\Sigma^{+-}}{d\Omega}$, (c) $\frac{d\Sigma^{-+}}{d\Omega}$.

The cross sections for a neutron beam in the x direction with $\alpha = 0$ (*i.e.* $\mathbf{P} \parallel \hat{\mathbf{Z}} = \hat{\mathbf{z}}$) are shown in Fig. 6.7, where the profile is assumed to be repeated periodically in the z direction. The NSF channel is now sensitive to the OOP domains. However, since the stripes are aligned with the Y direction, there is no periodicity in that direction. The intensity for the NSF channel is therefore nearly zero, with remaining peaks at $q_Y = \pm 2\pi/500 \simeq \pm 0.013$ nm^{-1} resulting from the periodicity of the simulation box. The SF channels, sensitive to the in-plane magnetization, exhibit no peaks in the q_Y direction. The periodic repetition of the profile along the z direction gives rise to peaks at $q_Z = \pm 2\pi/d \simeq \pm 0.12$ nm^{-1}. This is however not physical since in reality, the profile is not repeated along z.

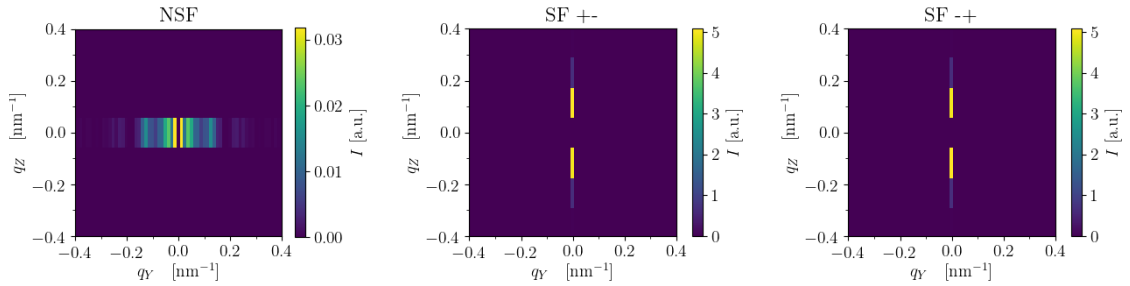

(a) **(b)** **(c)**

Figure 6.7: MSANS cross sections for the sample of Fig. 6.5 with a stripe pattern for a beam in the x direction with $\alpha = 0$. (a) $\frac{d\Sigma^{\pm\pm}}{d\Omega}$, (b) $\frac{d\Sigma^{+-}}{d\Omega}$, (c) $\frac{d\Sigma^{-+}}{d\Omega}$.

In order to be sensitive to the periodicity of the stripes, it is needed to align the beam in the y direction. The results with $\alpha = 0$ (*i.e.* $\mathbf{P} \parallel \hat{\mathbf{Z}} = \hat{\mathbf{z}}$) are shown in Fig. 6.8, where the periodic and compact domain options for the z direction are compared. In both cases, the NSF channels, sensitive to the OOP domains, have peaks at $q_Y = \pm 2\pi/71.4 \simeq \pm 0.09$ nm^{-1}. The SF channels, along the line $q_Z = 0$ nm^{-1}, are sensitive to m_y and therefore exhibit peaks at $q_Y = \pm 2\pi/35.7 \simeq \pm 0.18$

nm^{-1}. For $q_Y \neq 0$ and $q_Z \neq 0$, the SF channels are sensitive are also sensitive to m_x and m_z. Additional stripes are therefore visible at $q_Y = \pm 2\pi/71.4 \simeq \pm 0.09$ nm^{-1}. By comparing the results for a periodic profile along z and a compact domain along z, one can see that the zero-padding increases the q_Z resolution. The peaks along q_Z are also higher and at lower q_Z values. This can be explained by comparing the Fourier transforms for a signal repeated periodically and for the signal on a compact domain. This is illustrated for m_x along the thickness for a domain wall in Fig. 6.9.

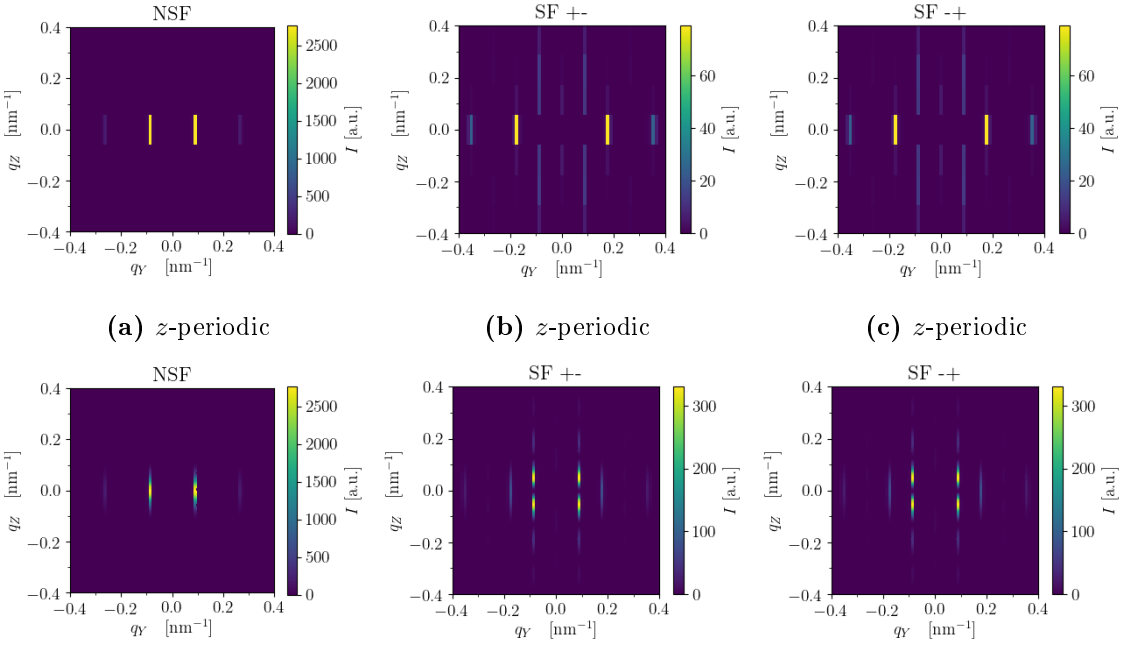

(a) z-periodic **(b)** z-periodic **(c)** z-periodic

(d) z-compact **(e)** z-compact **(f)** z-compact

Figure 6.8: MSANS cross sections for the sample of Fig. 6.5 with a stripe pattern for a beam in the y direction with $\alpha = 0$. Top row: profile repeated along z. Bottom row: compact domain along z (zero-padding). (a,d) $\frac{\mathrm{d}\Sigma^{\pm\pm}}{\mathrm{d}\Omega}$, (b,e) $\frac{\mathrm{d}\Sigma^{+-}}{\mathrm{d}\Omega}$, (c,f) $\frac{\mathrm{d}\Sigma^{-+}}{\mathrm{d}\Omega}$.

Let us now consider the effect of a tilt of the polarization axis. The results with $\alpha = 15°$ are shown in Fig. 6.10. By tilting the polarization in the Y direction, the NSF cross sections barely change. On the contrary, the SF channels become now sensitive to the OOP component m_z, which has a period of 71.4 nm, giving rise to peaks at $q_Y \simeq \pm 0.09$ nm^{-1}. Finally, the peaks in the case of a z-compact domain are on a line tilted by an angle α w.r.t. the $q_Z = 0$ line.

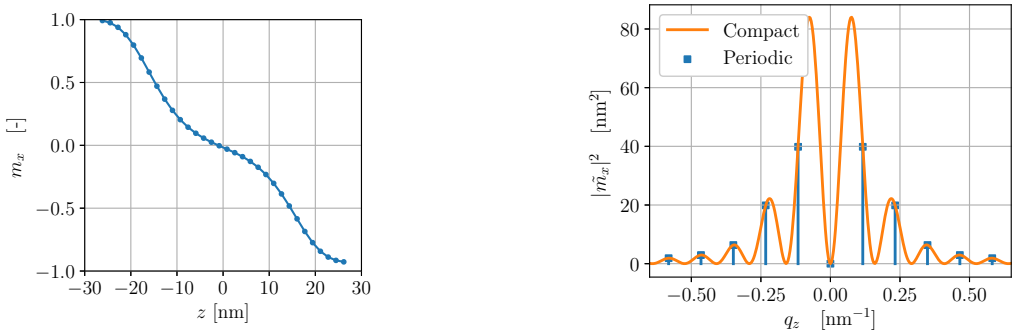

(a) **(b)**

Figure 6.9: $m_x(z)$ profile along the thickness for a domain wall (a) and its Fourier transform $\tilde{m_x}(q_z)$ (b) when the signal is repeated periodically or when the domain is compact.

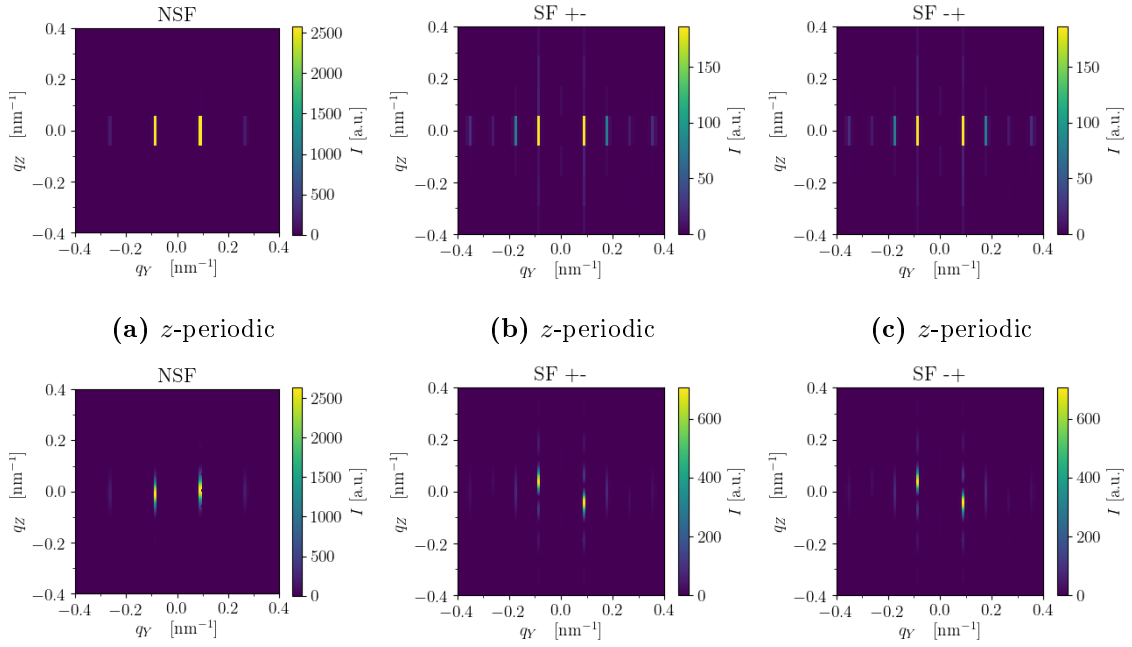

(a) z-periodic **(b)** z-periodic **(c)** z-periodic

(d) z-compact **(e)** z-compact **(f)** z-compact

Figure 6.10: MSANS cross sections for the sample of Fig. 6.5 with a stripe pattern for a beam in the y direction with $\alpha = 15°$. Top row: profile repeated along z. Bottom row: compact domain along z (zero-padding). (a,d) $\frac{d\Sigma^{\pm\pm}}{d\Omega}$, (b,e) $\frac{d\Sigma^{+-}}{d\Omega}$, (c,f) $\frac{d\Sigma^{-+}}{d\Omega}$.

6.3.4 Results for a maze pattern

Let us now analyze the results in the case of the maze pattern obtained in Chapter 5 for the sample with high PMA ($Q = 2.0$ and $d = 44$ nm) during the OOP reversal of Fig. 5.19. The pattern at remanence is given in Fig. 6.11. Since 3 reverse domains have nucleated from the 3 holes, and since periodic boundary conditions are applied in the x and y directions, the period is actually fixed by these simulation parameters at $P_x = P_y = 2w = 500/3 \simeq 166.7$ nm. When the reverse domains nucleate around each hole, the Bloch component of the wall forms a loop either in the clockwise (CW) or the counterclockwise (CCW) direction. This property is conserved during the growth of the reversal domains and determines the chirality (left or right-handed) of the domain walls (DWs) for each reverse domain. Since only symmetric energy terms have been included in the simulations so far, it is expected to have equal probabilities of 1/2 for CW and CCW reverse domains. In the present simulation, as can be seen in Fig. 6.11b, two reverse domains are counterclockwise and the third one is clockwise. This implies that two domain walls are right-handed and the third one is left-handed. The population of left and right-handed domain walls being unequal, it is expected to observe spin-flip splitting for this simulation. Note that since only three reverse domains have nucleated, it is impossible to have the same amount of CW and CCW reverse domains.

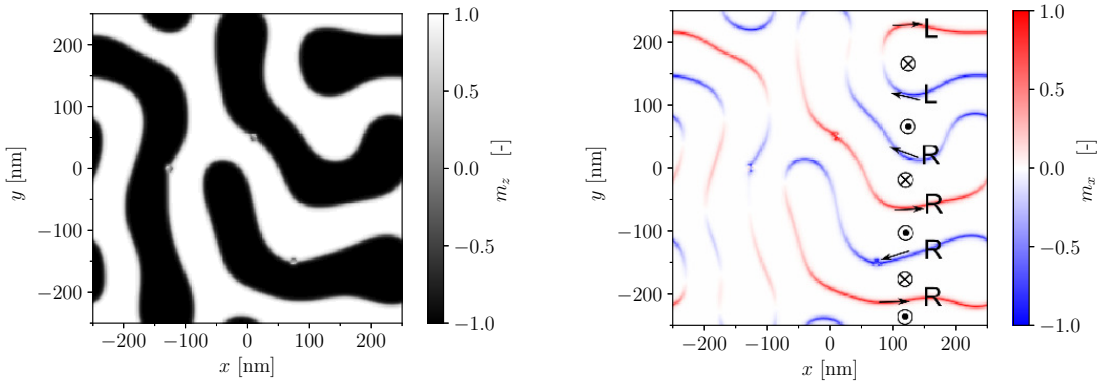

(a) m_z **(b)** m_x

Figure 6.11: Top view at mid-thickness of the sample with high PMA of Chapter 5 during the out-of-plane reversal, at remanence. (a) OOP component m_z with a gray color scale revealing the domains. (b) IP component m_x with a blue-white-red color scale revealing the domain walls (DWs). The direction of the magnetization in the domains and the walls is indicated in black. R, L: right and left-handed DWs.

The MSANS cross section for a neutron beam in the z direction with $\alpha = 0$ (*i.e.* $\mathbf{P} \parallel \hat{\mathbf{Z}} = -\hat{\mathbf{y}}$) are shown in Fig. 6.12. The m_y component having roughly a period of 250 nm gives rise to peaks at $q_Y = \pm 2\pi/250 \simeq \pm 0.025$ nm^{-1} for the NSF channels.

The m_z component having a period of 166.7 nm in the in-plane directions gives rise to a circle of radius $2\pi/166.7 \simeq 0.038$ nm^{-1} for the SF channels. Since the pattern is not perfectly isotropic, the circle has some peaks of higher intensities indicating the preferred directions.

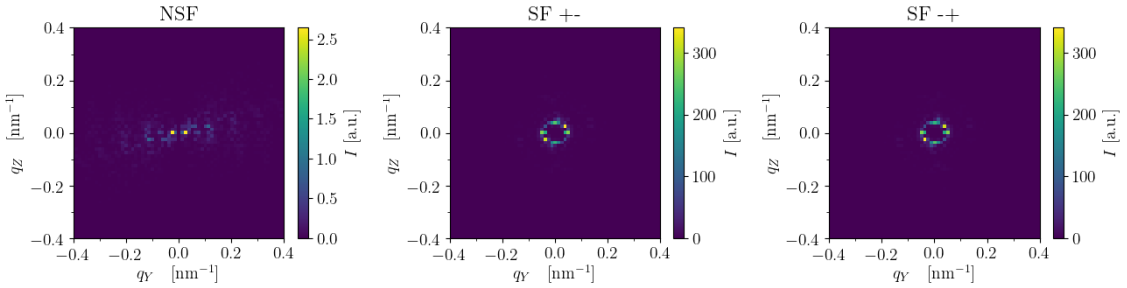

Figure 6.12: MSANS cross sections for the sample of Fig. 6.11 with a maze pattern for a beam in the z direction with $\alpha = 0$. (a) $\frac{d\Sigma^{\pm\pm}}{d\Omega}$, (b) $\frac{d\Sigma^{+-}}{d\Omega}$, (c) $\frac{d\Sigma^{-+}}{d\Omega}$.

The cross sections for a neutron beam in the x direction with $\alpha = 0$ (*i.e.* $\mathbf{P} \parallel \hat{\mathbf{Z}} = \hat{\mathbf{z}}$) are shown in Fig. 6.13, where the periodic and compact domain options for the z direction are compared. The OOP domains give rise to peaks at $q_Y = \pm 2\pi/166.7 \simeq \pm 0.038$ nm^{-1} for the NSF channels. For the SF channels, the pattern along the z direction of the in-plane components gives rise to peaks for $q_Z \neq 0$. There is an asymmetry in the q_Z direction, but not in the q_Y direction.

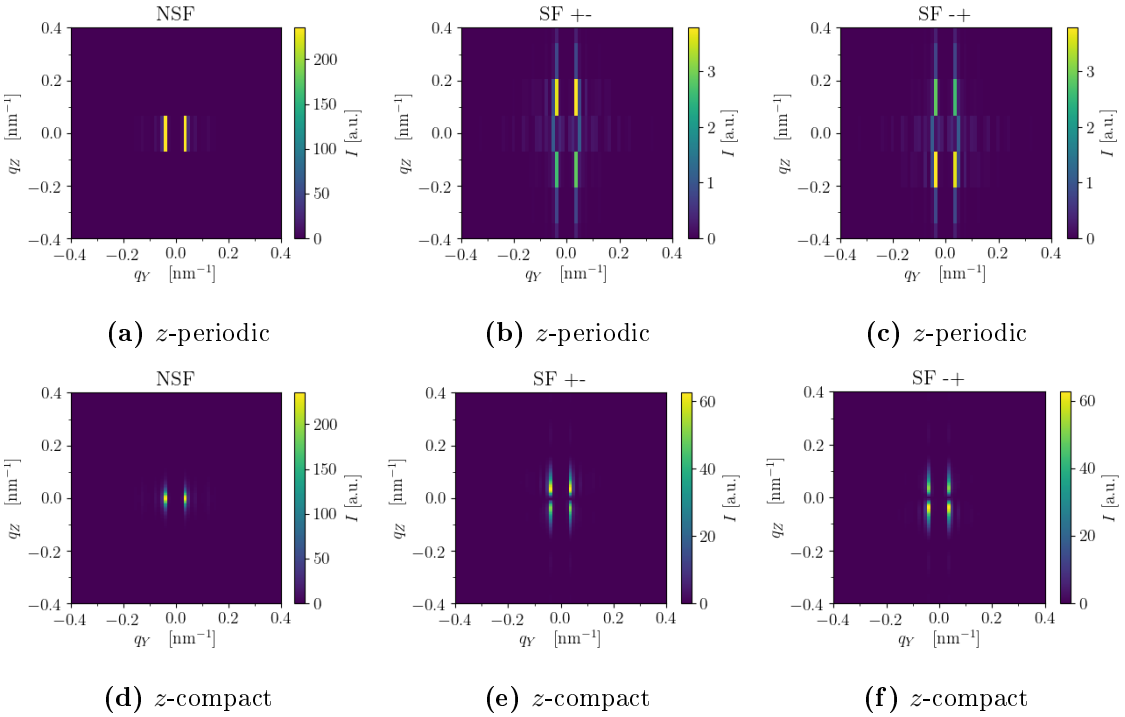

(a) z-periodic **(b)** z-periodic **(c)** z-periodic

(d) z-compact **(e)** z-compact **(f)** z-compact

Figure 6.13: MSANS cross sections for the sample of Fig. 6.11 with a maze pattern for a beam in the x direction with $\alpha = 0$. Top row: profile repeated along z. Bottom row: compact domain along z (zero-padding). (a,d) $\frac{d\Sigma^{\pm\pm}}{d\Omega}$, (b,e) $\frac{d\Sigma^{+-}}{d\Omega}$, (c,f) $\frac{d\Sigma^{-+}}{d\Omega}$.

In order to be sensitive to the chirality of the Bloch walls, it is needed to tilt the polarization in the Y direction. The results with $\alpha = 15°$ are shown in Fig. 6.14. As expected, an asymmetry between the peaks in the SF is observed whereas the peaks in the NSF are still symmetric. The asymmetry is in opposite directions for the "+-" and the "-+" channels. The same behavior is observed when considering a z-compact domain, but with the peaks on a line tilted by an angle α.

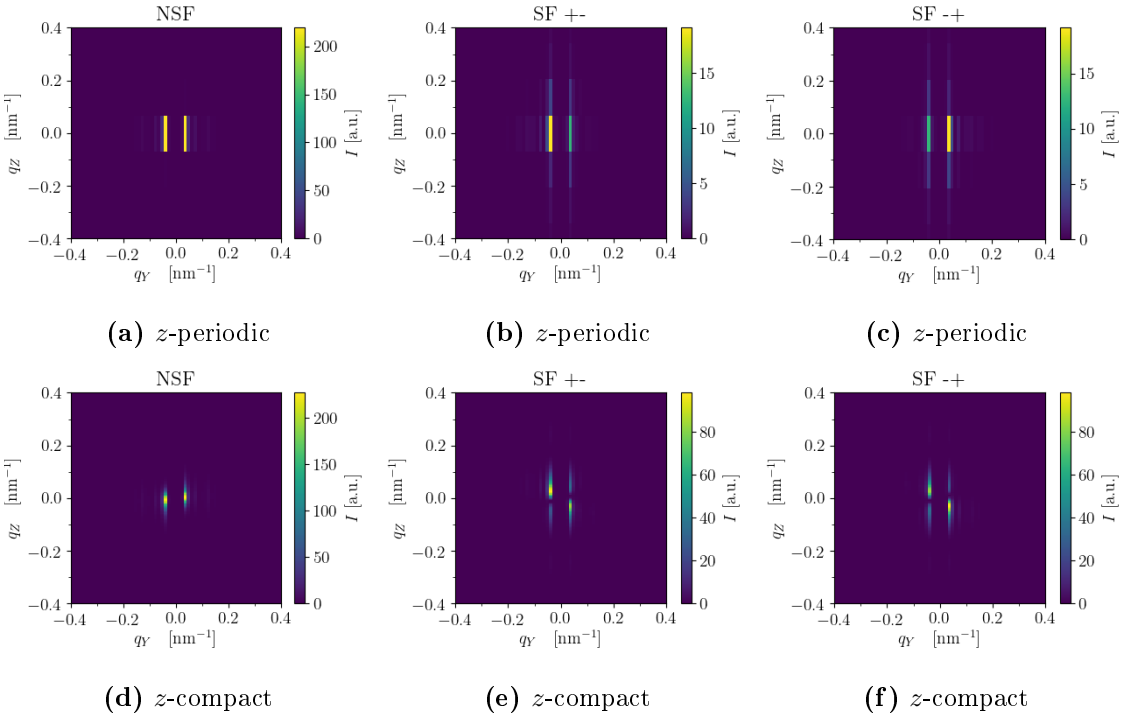

(a) z-periodic **(b)** z-periodic **(c)** z-periodic

(d) z-compact **(e)** z-compact **(f)** z-compact

Figure 6.14: MSANS cross sections for the sample of Fig. 6.11 with a maze pattern for a beam in the x direction with $\alpha = 15°$. Top row: profile repeated along z. Bottom row: compact domain along z (zero-padding). (a,d) $\frac{d\Sigma^{\pm\pm}}{d\Omega}$, (b,e) $\frac{d\Sigma^{+-}}{d\Omega}$, (c,f) $\frac{d\Sigma^{-+}}{d\Omega}$.

The asymmetry between the two peaks in the SF channels can be characterized by

$$C = \frac{I_1 - I_2}{I_1 + I_2} \tag{6.9}$$

where I_1 and I_2 are the intensities of the two peaks. In Fig. 6.15, the asymmetry is given as a function of the tilt α of the polarization axis. One can see that for $\alpha = 0$, there is no asymmetry. When α increases, C increases until reaches a maximum before converging to a smaller value at $\alpha = 90°$. This can be understood with Fig. 6.16, where the symmetric and antisymmetric parts of the SF cross section along the $q_Z = 0$ line are shown for 3 different values of α. For $\alpha = 0$, the antisymmetric part is zero. When α increases, the sensitivity to the chirality increases giving rise to an antisymmetric part. However, the symmetric part becomes more and more sensitive to the OOP component m_z. The amplitude of the symmetric part increases faster than the antisymmetric part, resulting in a maximum of the asymmetry for the total cross section for a certain value of α. Note that the maximum value of C and the angle α at that maximum depend on the exact pattern and the direction of the beam. The maximum C increases when the imbalance between left and right-handed DWs increases and when the number of domain walls aligned with the beam axis increases. Different patterns were obtained when the position of the three holes was changed.

For patterns where all the DWs have the same handedness, and where a large amount of DWs were aligned with the beam axis, asymmetries as high as $C = 0.98$ could be observed.

In the next two sections, two possible explanations for the asymmetry observed in the measurements of Fig. 6.3 are investigated.

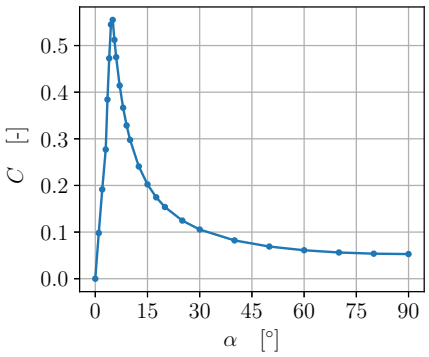

Figure 6.15: Asymmetry $C = (I_1 - I_2)/(I_1 + I_2)$ between the peaks in the SF channels as a function of the tilt α of the polarization axis. Example for a neutron beam in the x direction for the sample of Fig. 6.11 with a maze pattern.

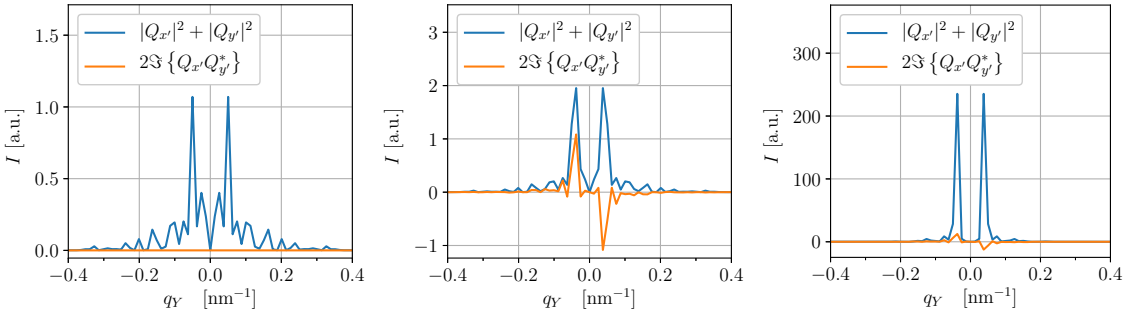

(a) $\alpha = 0°$ **(b)** $\alpha = 5°$ **(c)** $\alpha = 90°$

Figure 6.16: Symmetric part $|Q_{x'}|^2 + |Q_{y'}|^2$ and antisymmetric part $\Im\left\{Q_{x'}Q_{y'}^*\right\}$ of the cross section $\frac{\mathrm{d}\Sigma^{\pm\mp}}{\mathrm{d}\Omega}$ for the SF channels, for three values of the tilt α of the polarization axis. Example for a neutron beam in the x direction for the sample of Fig. 6.11 with a maze pattern.

6.4 Hypothesis 1: fluctuation of a non-chiral system

The first hypothesis to explain the asymmetry is a statistic fluctuation of a non-chiral system due to finite sampling. This hypothesis is supported by the notion of coherence volume. The coherence volume describes the maximum size of a structure that is observable by neutron scattering, as a consequence of the imperfect collimation and monochromatization of the beam. The collimation of the beam gives rise to coherence lengths in the two transverse directions, after which the waves are completely out of phase. The imperfect monochromatization gives rise to a spread of the wavelength, defining a longitudinal coherence length. Those three coherence lengths define a coherence volume from which the waves are scattered coherently and can interfere. The observed cross section is therefore not the one obtained from the whole sample considering an incoming plane wave. The resulting cross section is an independent sum of all the cross sections obtained from all the coherence volumes of the sample. This is called incoherent superposition.

If we consider a coherence volume with a relatively small number of reverse domains, the probability that the number of right-handed and left-handed walls are different is high. This was obvious in the previous section, where it was impossible to have the same amount of left and right-handed walls since there were only 3 reverse domains. This would give rise to spin-flip splitting for the scattering of one coherence volume. Incoherent superposition of the intensities of all the coherence volumes would decrease the asymmetry, but still a non-zero asymmetry could remain, even though the system is perfectly non-chiral with equal probabilities for left and right-handed walls.

To investigate this hypothesis, let us consider that the sample is composed of N independent coherence volumes. We suppose that for each coherence volume, the asymmetries can take the values $\pm C_0$ with equal probability. Approximating the incoherent superposition from all the possible coherence volumes by a sum on the N independent coherence volumes, the observed value of C is given by

$$C = C_0 \frac{1}{N} \sum_{n=1}^{N} \epsilon_n \tag{6.10}$$

where ϵ_n are independent random numbers taking values $+1$ or -1 with equal probability $1/2$. The average value of C is zero and its variance is

$$\left\langle C^2 \right\rangle = C_0^2/N. \tag{6.11}$$

For N large enough, one can rely on the central-limit theorem and assume that $C\sqrt{N}/C_0$ follows a normal distribution with zero mean and unit variance. The fluctuations of C therefore satisfy

$$\text{Prob}\left(\frac{C\sqrt{N}}{C_0} \in [-x, x]\right) = \text{erf}\left(\frac{x}{\sqrt{2}}\right) \tag{6.12}$$

$$\iff \text{Prob}\left(\frac{|C|\sqrt{N}}{C_0} > x\right) = 1 - \text{erf}\left(\frac{x}{\sqrt{2}}\right) \tag{6.13}$$

where erf is the error function.

The asymmetry in the measurements of Fig. 6.3 is $C = 0.076$. The sample size is 1 cm^2 and the neutron beam covers the whole sample. In GISANS, the typical resolution is such that $2\pi/q_X$ ranges from 1 to 20 μm and $2\pi/q_Y$ ranges from 1 to 300 nm. Neglecting the effect of the coherence along the thickness, the ratio N of irradiated sample volume to one coherence volume is approximated by

$$N \simeq \frac{1\text{cm}^2}{20\mu\text{m} \times 300\text{nm}} = \frac{10^8\mu\text{m}^2}{6\mu\text{m}^2} \simeq 10^7. \tag{6.14}$$

The number of coherence volumes in the sample is extremely large and the probability to observe the value $C = 0.076$ simply due to statistical fluctuations is extremely small. Even with $C_0 = 1.0$, the probability to obtain a value of C higher than 0.076 is much smaller than 10^{-16}. Even with $N = 10^4$, the probability is 10^{-14}. If the sample was made of $N = 1000$, the probability is 0.16 and this hypothesis could be considered. But still, since the coherence volume of 6 μm^2 is already large, the value of C_0 is expected to be much smaller than 1. And since $N \simeq 10^7$, the hypothesis that the spin-flip splitting results from a fluctuation of a non-chiral system, within the assumptions stated in this section, can be rejected.

6.5 Hypothesis 2: chiral interaction

A second hypothesis to explain the spin-flip splitting for a macroscopic sample is that there exists a chiral interaction that favors one handedness for the domain walls over the other. The Dzyaloshinskii-Moriya interaction (DMI) [12, 13] introduced in Chapter 2 with Eq. 2.15 is an example of antisymmetric interaction that favors magnetization rotations with a fixed chirality. This interaction originates from the combination of large spin-orbit coupling and a lack of symmetry. It exists in bulk materials lacking space inversion symmetry or at the interface between a magnetic layer and a high spin-orbit coupling adjacent layer (typically a heavy metal) where the symmetry breaking originates from the interface.

Interfacially-induced DMI for a stack of magnetic layers of thickness t_{FM} separated by non-magnetic layers of thickness t_{NM} has the form [45]

$$E_{\mathrm{DMI,ind}} = \sum_i \int\int \mathrm{d}x\mathrm{d}y \Big[\mathbf{D}_i^x \cdot (\mathbf{m}_i \times \partial_x \mathbf{m}_i) + \mathbf{D}_i^y \cdot (\mathbf{m}_i \times \partial_y \mathbf{m}_i) + \frac{1}{t_{\mathrm{FM}} + t_{\mathrm{NM}}} \mathbf{D}_i^z \cdot (\mathbf{m}_i \times \mathbf{m}_{i+1}) \Big] \tag{6.15}$$

where i is the layer index in the z direction and $\mathbf{D}_i^{x,y,z}$ are the DMI vectors. The first two terms of Eq. 6.15 describe intralayer coupling (*i.e.* inside a magnetic layer) whereas the third term describes interlayer coupling (*i.e.* between two magnetic layers). Both intralayer and interlayer coupling can create a favored chirality of the Bloch walls, as illustrated in Fig. 6.17. Considering a wall parallel to the yz-plane, intralayer coupling with $\mathbf{D}_i^x \parallel \hat{\mathbf{x}}$ favors one chirality for the Bloch wall. For the interlayer coupling, the effect of the demagnetizing field that induces Néel closure domains on the top and the bottom must be taken into account. The orientation of the magnetization in the Néel caps being fixed by the demagnetizing field, the third term with $\mathbf{D}_i^z \parallel \hat{\mathbf{z}}$ favors one chirality in the z direction. Consequently, one chirality for the Bloch wall in the x direction is also favored. Pollard *et al.* [45] showed that interlayer coupling for a stack of Co and Pd layers was the origin for a preferred Bloch wall chirality. The layers of Co and Pd could be compared to the layer of Fe and Pd of FePd in the $L1_0$ phase. However, the layers in [45] are several atoms thick, whereas the layers in the $L1_0$ phase are monoatomic.

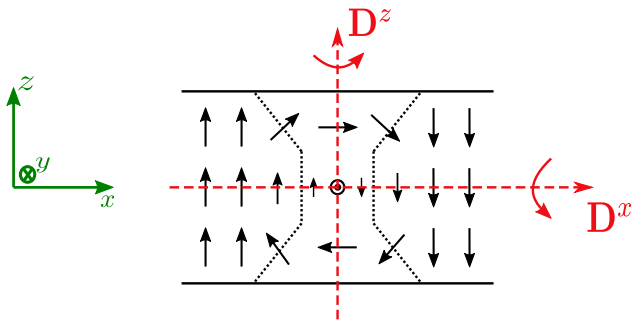

Figure 6.17: Illustration on how interfacially-induced DMI can favor one chirality for the Bloch wall. For intralayer coupling, if $\mathbf{D}^x$ lies in the x-direction, the handedness indicated with the curved arrow is favored. For interlayer coupling, if $\mathbf{D}^z$ lies in the z-direction, the rotation direction indicated by the curved arrow is favored. Since the magnetization direction in the Néel caps is preferentially in the flux-closure state, the preferred rotation direction along z induces a preferred handedness for the Bloch wall (in the x-direction).

Interfacially-induced DMI is implemented in *MuMax3* [16] with an energy density of the form [46]

$$\begin{aligned} e_{\text{DMI,ind,MuMax}} &= D_{\text{ind}} \left[m_z(\nabla \cdot \mathbf{m}) - (\mathbf{m} \cdot \nabla) m_z \right] \\ &= D_{\text{ind}} \left[m_z \frac{\partial m_x}{\partial x} + m_z \frac{\partial m_y}{\partial y} - m_x \frac{\partial m_z}{\partial x} - m_y \frac{\partial m_z}{\partial y} \right]. \end{aligned} \tag{6.16}$$

This expression contains only part of the terms of Eq. 6.15 and is equal to zero for a Bloch wall in the yz-plane. This expression is therefore unlikely to favor the chirality of the Bloch walls in our case.

Bulk DMI is implemented in *MuMax3* under the form

$$e_{\text{DMI,bulk,MuMax}} = D_{\text{bulk}} \left[\mathbf{m} \cdot (\nabla \times \mathbf{m}) \right]. \tag{6.17}$$

One can show that $-\mathbf{m} \cdot (\nabla \times \mathbf{m})$ corresponds to the helicity p (defined in Section 6.2) in the continuous case. Bulk DMI can therefore favor one chirality over another depending on the sign of D_{bulk}.

FePd in the $L1_0$ possesses inversion symmetry. Therefore it should not exhibit bulk DMI. Nevertheless, let us consider bulk DMI in order to see the effect of an antisymmetric interaction on the chirality of the domain walls. The results when bulk DMI is added to the sample of Fig. 6.11 are shown in Fig. 6.18. While typical values of D_{bulk} are of the order of 0.1 mJ/m^2 [47], one can see in Fig. 6.18 that the chirality of the Bloch walls can be controlled with interactions as weak as $D_{\text{bulk}} = 0.05$ mJ/m^2 (or even weaker), while the domain pattern remains unchanged. Without DMI, we observe left and right-handed DWs. For $D_{\text{bulk}} = +0.05$ mJ/m^2, all the DWs are right-handed whereas for $D_{\text{bulk}} = -0.05$ mJ/m^2, they are all left-handed. The corresponding results for the MSANS SF channels are also given in Fig. 6.18. The asymmetry is indeed increased when all the walls have the same chirality, and is in opposite directions for left and right-handed chiralities. This shows that a weak chiral interaction can favor one chirality for the DWs, without affecting the domain pattern. This results in an unbalance between the left and right-handed DWs and could explain the spin-flip splitting observe for macroscopic samples.

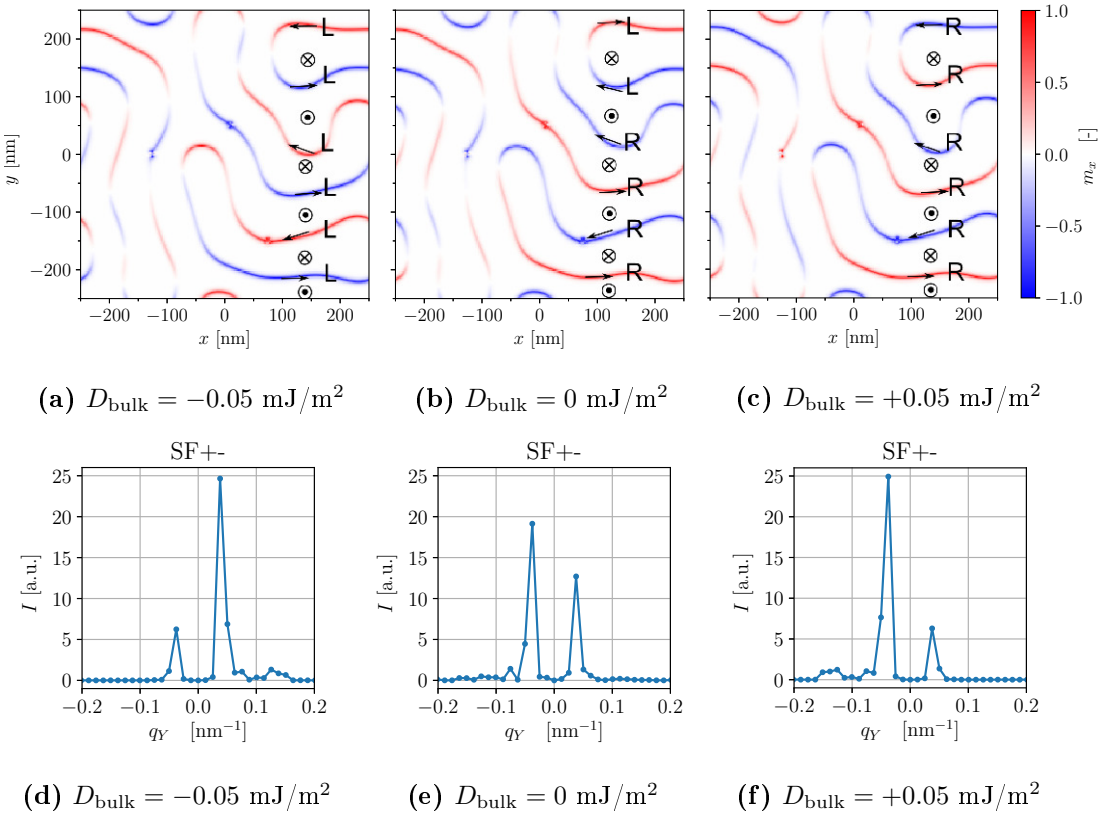

(a) $D_{\text{bulk}} = -0.05$ mJ/m^2 **(b)** $D_{\text{bulk}} = 0$ mJ/m^2 **(c)** $D_{\text{bulk}} = +0.05$ mJ/m^2

(d) $D_{\text{bulk}} = -0.05$ mJ/m^2 **(e)** $D_{\text{bulk}} = 0$ mJ/m^2 **(f)** $D_{\text{bulk}} = +0.05$ mJ/m^2

Figure 6.18: (a,b,c) Top view at mid-thickness of the sample with high PMA during the out-of-plane reversal, at remanence, for several values of the bulk DMI parameter D_{bulk}. IP component m_x with a blue-white-red color scale revealing the domain walls (DWs). The direction of the magnetization in the domains and the walls is indicated in black. R, L: right and left-handed DWs. (d,e,f) SF cross section $\frac{d\Sigma^{+-}}{d\Omega}$ for a neutron beam in the x direction with $\alpha = 15°$ corresponding to the samples of (a,b,c).

6.6 Conclusion

Neutron scattering with polarization analysis is a useful measurement technique to obtain information on the magnetic configuration in a sample. In GISANS, the neutron beam impinges the surface at a very small angle close to total reflection. When the polarization axis is perpendicular to the sample surface, the non-spin flip (NSF) channels are sensitive to the out-of-plane component of the magnetization. On the contrary, the spin-flip (SF) channels are sensitive to the component of the magnetization perpendicular to the polarization axis, which corresponding to the in-plane component. In experimental measurements performed on an FePd thin film with high PMA and exhibiting a maze pattern, an asymmetry between the two peaks in the SF channel is observed, called spin-flip splitting (SFS), is observed when the polarization is tilted. This indicates that the average chirality of the Bloch walls is nonzero.

In Magnetic Small-Angle Neutron Scattering (MSANS), the neutron beam is usually directed perpendicular to the sample surface. The formalism to compute the cross sections in MSANS is much simpler than for GISANS, since it is a combination of the Fourier transforms of the 3 components of the magnetization. This has been implemented in a *Python* code to compute the cross sections for the configurations obtained by micromagnetic simulations. The results for a stripe pattern and a maze pattern are analyzed, with a neutron beam at normal incidence, as well as in the plane of the sample. The latter is not feasible in practice, since it is unlikely that the neutrons can transmit through the whole width of the sample. Moreover, the assumption of a small scattering angle would not be valid in this case. Nevertheless, it remains interesting because spin-flip splitting is obtained in this case only when the average chirality is nonzero, meaning that there is an imbalance between the populations of left and right-handed walls. This supports the idea that the spin-flip splitting observed in the GISANS measurements is due to a nonzero chirality.

Finally, two hypotheses to explain the observed SFS are investigated. The first one, namely that it is a consequence of statistical fluctuations of an inherently non-chiral system, can be rejected because the neutron beam covers a very large area compared to the domains. The second one, namely that a weak chiral interaction can favor one handedness for the Bloch walls, is plausible. A weak antisymmetric interaction like the Dzyaloshinskii-Moriya interaction (DMI) can indeed create an unbalance between the left and right-handed walls, without perturbing the domain pattern. This is however not a proof that DMI exists in FePd thin films. Even if such a chiral interaction could be induced by the growth methods, by interfaces or by the defects, other physical sources of chirality in the system should be investigated. These questions about the physical origin of chirality suggest interesting research for the future.

Chapter 7

Conclusion and outlook

7.1 Conclusions

The emerging field of spintronics offers the prospect of lower power consumption and higher performances for future technologies. Extensive research is therefore carried out on magnetic materials. Materials with perpendicular magnetic anisotropy (PMA), like FePd, are used in spintronic devices for memory and logic applications. Research on this type of materials includes the study of the magnetic configuration in thin films, how it can be controlled and how it switches. Research must be carried out experimentally, in order to observe and understand how those materials behave in real life. In parallel, micromagnetic simulations enable one to support experimental results and to understand the physics underlying those results. For these reasons, the objective of this thesis was to study the domain-wall structure and the reversal mechanisms in FePd thin films, by means of micromagnetic simulations. The simulations performed in this thesis also provide support and explanations to experimental results obtained in Annika Stellhorn's PhD thesis [8]. The three main goals of this thesis are reminded below, together with a summary of the important conclusions.

Goal 1: study of the domain-wall structure.

Below a critical thickness d_c, the equilibrium magnetization configuration lies in the plane of the film due to the magnetostatic interaction between the bottom and top surfaces. d_c is a function of the anisotropy quality factor $Q = K_u/(\frac{1}{2}\mu_0 M_s^2)$ where K_u is the anisotropy constant and M_s the saturation magnetization. The critical thickness diverges to infinity when Q tends to zero. When Q increases, d_c decreases and is zero for high anisotropies ($Q > 1$).

For thicknesses above d_c, out-of-plane magnetic domains are formed, with alternating up and down magnetization, separated by domain walls (DWs). The DWs are of

Bloch type in the middle of the thickness and Néel closure domains are present at the top and bottom surfaces. The width of the DWs is nearly independent of the thickness of the film, but decreases when the strength of the anisotropy increases.

Goal 2: understand the hysteresis and reversal mechanisms.

The reversal mechanisms for an in-plane (IP) and an out-of-plane (OOP) applied field have been studied.

For an IP field, starting from saturation, a stripe pattern with alternating up and down magnetization is gradually formed when the field decreases. All the Bloch walls are in the direction of the previous saturated state, giving rise to a remanent magnetization when the applied field is zero. Increasing the field in the opposite direction, the Bloch walls switch and a saturated state is gradually obtained. This results in some hysteresis around zero applied field and no hysteresis at higher fields where the magnetization changes gradually. The smaller the degree of PMA, the steeper the slope, since in-plane magnetization is energetically favorable.

For an OOP field, starting from saturation, cylindrical domains in the reverse direction nucleate when the field decreases. They then grow until they form a maze pattern. When the field increases in the opposite direction, the domains in the previous saturated direction shrink, until they are separated into cylindrical domains and finally disappear. This results in some hysteresis at high fields, and less hysteresis around zero applied field.

Interestingly, for both the IP and OOP cases, the hysteresis curve depends critically on the defects in the sample. Defects are central to enable the nucleation of domains and must therefore be included in the simulations.

Goal 3: interpret neutron scattering measurements in terms of chirality of the domain walls.

Neutron scattering with polarization analysis is a useful measurement technique to obtain information on the domain pattern and even the structure of the domain walls. Grazing-Incidence Small-Angle Neutron Scattering (GISANS) measurements have been performed on a real sample in [8], during the out-of-plane reversal. When the polarization axis in tilted in the in-plane direction, an asymmetry is observed between the peaks in the spin-flip (SF) channels, termed spin-flip splitting (SFS). This suggests that the population numbers of left-handed and right-handed domain walls are unequal, leading to a nonzero average chirality.

A *Python* code has been written to compute the result of Magnetic Small-Angle Neutron Scattering (MSANS) for the configurations obtained by micromagnetic simulations. Spin-flip splitting is also observed when there exists a nonzero average chirality, confirming the explanation for the real measurements.

The hypothesis that the nonzero average chirality is a result of statistical fluctuations of an inherently non-chiral system can be rejected due to the large number of domain walls in a sample. This suggests that there exists a physical source of chirality in the system. An example could be a chiral interaction like the Dzyaloshinkii-Moriya interaction (DMI). By changing the sign of this interaction, the handedness of the domain walls can be changed, without affecting the domain pattern.

7.2 Outlook

Future possible works include the following topics.

A more extensive study of the types of defects present in FePd thin films as a function of the growth method and the effect on the reversal mechanisms should be carried out. Defects are indeed central in the reversal mechanisms, and different types of defects may allow one to tune the material's magnetic behavior.

Software exists to simulate the cross sections for GISANS measurements using different models for the magnetic configuration as input [48, 43, 49]. One could implement the option to compute the cross sections directly for the configurations obtained by micromagnetic simulations, using the Distorted Wave Born Approximation (DWBA). This would provide a direct comparison between the results obtained experimentally and by simulation.

The physical origin of the chirality observed in FePd thin films should be investigated. It could be induced by a special type of defect, by the growth method, or by coupling effects with adjacent layers.

Appendix A

CGS and SI units

In magnetism, two main systems of units are currently used: the Centimeter-Gram-Second System of Units (CGS) and the International System of Units (SI) (meter-kg-second-Ampère). The first one is used a lot in textbooks and scientific literature because it simplifies the writing of the equations. However, only the SI is used throughout this thesis for two reasons. First, because it is an international convention, also used in all the other branches of physics. Second, since the magnetic permeability of vacuum μ_0 is much small than one in the SI (on the contrary to the CGS in which it is one), the **B** and **H** have very different values and units, preventing any confusion between those different fields.

A conversion table between the CGS and SI units for the physical quantities relevant in this thesis is given in Table A.1.

Physical quantity or constant	**Symbol**	**CGS**	**SI**
Magnetic field	H	1 Oersted	$10^3/4\pi$ A m^{-1}
Magnetic flux density	B	1 Gauss	10^{-4} T
Magnetization	M	1 emu cm^{-3}	10^3 A m^{-1}
Magnetic moment	μ	1 emu	10^{-3} A m^2
Exchange constant	A	1 erg cm^{-1}	10^{-5} J m^{-1}
Anisotropy constant	K_u	1 erg cm^{-3}	10^{-1} J m^{-3}
Length	d	1 cm	10^{-2} m
Energy per unit volume	e	1 erg cm^{-3}	10^{-1} J m^{-3}
Vacuum permeability	μ_0	1 [-]	$4\pi\ 10^{-7}$ T m A^{-1}

Table A.1: Conversion table between the CGS and SI units for the quantities relevant in this thesis. Inspired from [26].

Bibliography

[1] A. Hirohata, K. Yamada, Y. Nakatani, I.-L. Prejbeanu, B. Diény, P. Pirro, and B. Hillebrands. "Review on spintronics: Principles and device applications". *Journal of Magnetism and Magnetic Materials*, **509**, p. 166711, 2020. DOI: 10.1016/j.jmmm.2020.166711.

[2] M. Julliere. "Tunneling between ferromagnetic films". *Physics Letters A*, **54**(3), pp. 225–226, 1975. DOI: 10.1016/0375-9601(75)90174-7.

[3] M. N. Baibich, J. M. Broto, A. Fert, F. Nguyen Van Dau, F. Petroff, P. Etienne, G. Creuzet, A. Friederich, and J. Chazelas. "Giant Magnetoresistance of (001)Fe/(001)Cr Magnetic Superlattices". *Physical Review Letters*, **61**(21), pp. 2472–2475, 1988. DOI: 10.1103/physrevlett.61.2472.

[4] G. Binasch, P. Grünberg, F. Saurenbach, and W. Zinn. "Enhanced magnetoresistance in layered magnetic structures with antiferromagnetic interlayer exchange". *Physical Review B*, **39**(7), pp. 4828–4830, 1989. DOI: 10.1103/physrevb.39.4828.

[5] D.-L. Zhang, C. Sun, Y. Lv, K. B. Schliep, Z. Zhao, J.-Y. Chen, P. M. Voyles, and J.-P. Wang. "L10 Fe-Pd Synthetic Antiferromagnet through an fcc Ru Spacer Utilized for Perpendicular Magnetic Tunnel Junctions". *Physical Review Applied*, **9**(4), 2018. DOI: 10.1103/physrevapplied.9.044028.

[6] M. Viret, Y. Samson, P. Warin, A. Marty, F. Ott, E. Søndergård, O. Klein, and C. Fermon. "Anisotropy of Domain Wall Resistance". *Physical Review Letters*, **85**(18), pp. 3962–3965, 2000. DOI: 10.1103/physrevlett.85.3962.

[7] A. Stellhorn, A. Sarkar, E. Kentzinger, J. Barthel, A. Di Bernardo, S. Nandi, P. Zakalek, J. Schubert, and T. Brückel. "Tailoring superconducting states in superconductor-ferromagnet hybrids". *New Journal of Physics*, **22**(9), p. 093001, 2020. DOI: 10.1088/1367-2630/abaa02.

[8] A. Stellhorn. "Interplay of proximity effects in superconductor/ferromagnet heterostructures", PhD thesis, RWTH Aachen University, 2020.

[9] C. Kittel. *Introduction to Solid State Physics*. Global Edition. Wiley, 2018.

[10] J. M. D. Coey. *Magnetism and Magnetic Materials*. Cambridge University Press, 2009.

[11] R. Eisberg and R. Resnick. *Quantum physics of atoms, molecules, solids, nuclei, and particles*. Second Edition. Wiley, 1985.

[12] I. Dzyaloshinsky. "A thermodynamic theory of "weak" ferromagnetism of antiferromagnetics". *Journal of Physics and Chemistry of Solids*, **4**(4), pp. 241–255, 1958. DOI: 10.1016/0022-3697(58)90076-3.

[13] T. Moriya. "Anisotropic Superexchange Interaction and Weak Ferromagnetism". *Physical Review*, **120**(1), pp. 91–98, 1960. DOI: 10.1103/physrev.120.91.

[14] L. Exl, D. Suess, and T. Schref. *Micromagnetism*. URL: https://homepage.univie.ac.at/lukas.exl/files/mic_intro.pdf. (accessed on 16/05/2021).

[15] M.J. Donahue and D.G. Porter. *OOMMF User's Guide, Version 1.0*. URL: http://math.nist.gov/oommf. Interagency Report NISTIR 6376, National Institute of Standards and Technology, Gaithersburg, MD (Sept 1999).

[16] A. Vansteenkiste, J. Leliaert, M. Dvornik, M. Helsen, F. Garcia-Sanchez, and B. Van Waeyenberge. "The design and verification of MuMax3". *AIP Advances*, **4**(10), p. 107133, 2014. DOI: 10.1063/1.4899186.

[17] M.-A Bisotti, D. Cortés-Ortuño, R. Pepper, W. Wang, M. Beg, T. Kluyver, and H. Fangohr. "Fidimag – A Finite Difference Atomistic and Micromagnetic Simulation Package". *Journal of Open Research Software*, **6**(1), p. 22, 2018. DOI: 10.5334/jors.223.

[18] W. Scholz, J. Fidler, T. Schrefl, D. Suess, R. Dittrich, H. Forster, and V. Tsiantos. "Scalable parallel micromagnetic solvers for magnetic nanostructures". *Computational Materials Science*, **28**(2), pp. 366–383, 2003. DOI: 10.1016/s0927-0256(03)00119-8.

[19] T. Fischbacher, M. Franchin, G. Bordignon, and H. Fangohr. "A Systematic Approach to Multiphysics Extensions of Finite-Element-Based Micromagnetic Simulations: Nmag". *IEEE Transactions on Magnetics*, **43**(6), pp. 2896–2898, 2007. DOI: 10.1109/tmag.2007.893843.

[20] C. Abert, L. Exl, F. Bruckner, A. Drews, and D. Suess. "magnum.fe: A micromagnetic finite-element simulation code based on FEniCS". *Journal of Magnetism and Magnetic Materials*, **345**, pp. 29–35, 2013. DOI: 10.1016/j.jmmm.2013.05.051.

[21] R. Chang, S. Li, M. V. Lubarda, B. Livshitz, and V. Lomakin. "FastMag: Fast micromagnetic simulator for complex magnetic structures (invited)". *Journal of Applied Physics*, **109**(7), p. 07D358, 2011. DOI: 10.1063/1.3563081.

[22] J. Miltat and M.J. Donahue. "Numerical Micromagnetics: Finite Difference Methods". *Handbook of magnetism and advanced magnetic materials*, **2**, pp. 742–764, 2007. DOI: 10.1002/9780470022184.hmm202.

[23] H. Kronmüller. *General Micromagnetic Theory and Applications*. 2019. DOI: 10.1002/9783527603978.mst0460.

[24] Jülich Supercomputing Centre. "JUWELS: Modular Tier-0/1 Supercomputer at the Jülich Supercomputing Centre". *Journal of large-scale research facilities*, **5**(A135), 2019. DOI: 10.17815/jlsrf-5-171.

[25] A. Hubert and R. Schäfer. *Magnetic domains : the analysis of magnetic microstructures*. Springer, 1998. ISBN: 978-3-540-64108-7.

[26] V. Gehanno. "Perpendicular magnetic anisotropy in epitaxial thin films of FePd ordered alloys", PhD thesis, Université Joseph-Fourier - Grenoble 1, 1997.

[27] O. Ersen, V. Parasote, V. Pierron-Bohnes, M. C. Cadeville, and C. Ulhaq-Bouillet. "Growth conditions to optimize chemical order and magnetic properties in molecular-beam-epitaxy-grown CoPt/MgO(001) thin films". *Journal of Applied Physics*, **93**(5), pp. 2987–2995, 2003. DOI: 10.1063/1.1538319.

[28] T. Ichitsubo and K. Tanaka. "Single-crystal elastic constants of disordered and ordered FePd". *Journal of Applied Physics*, **96**, pp. 6220–6223, 2004. DOI: https://doi.org/10.1063/1.1809775.

[29] D. E. Laughlin, K. Srinivasan, M. Tanase, and L. Wang. "Crystallographic aspects of $L1_0$ magnetic materials". *Scripta Materialia*, **53**, pp. 383–388, 2005. DOI: 10.1016/j.scriptamat.2005.04.039.

[30] P. R. Aitchison, J. N. Chapman, V. Gehanno, I. S. Weir, M. R. Scheinfein, S. McVitie, and A. Marty. "High resolution measurement and modelling of magnetic domain structures in epitaxial FePd (0 0 1) L10 films with perpendicular magnetisation". *Journal of Magnetism and Magnetic Materials*, **223**, pp. 138–146, 2001. DOI: 10.1016/S0304-8853(00)00524-2.

[31] F. Virot, L. Favre, R. Hayn, and M. D. Kuz'min. "Theory of magnetic domains in uniaxial thin films". *Journal of Physics D: Applied Physics*, **45**(40), p. 405003, 2012. DOI: 10.1088/0022-3727/45/40/405003.

[32] M. W. Muller. "Distribution of the Magnetization in a Ferromagnet". *Physical Review*, **122**(5), pp. 1485–1489, 1961. DOI: 10.1103/physrev.122.1485.

[33] G. van der Laan, K. Chesnel, M. Belakhovsky, A. Marty, F. Livet, S.P. Collins, E. Dudzik, A. Haznar, and J.P. Attané. "Magnetic anisotropy of aligned magnetic stripe domains in FePd studied by soft x-ray resonant magnetic scattering, magnetic force microscopy and micromagnetic modeling". *Superlattices and Microstructures*, **34**(1-2), pp. 107–126, 2003. DOI: 10.1016/j.spmi.2004.01.005.

[34] D. Navas, C. Redondo, G. A. Badini Confalonieri, F. Batallan, A. Devishvili, Ó. Iglesias-Freire, A. Asenjo, C. A. Ross, and B. P. Toperverg. "Domain-wall structure in thin films with perpendicular anisotropy: Magnetic force microscopy and polarized neutron reflectometry study". *Physical Review B*, **90**(5), 2014. DOI: 10.1103/physrevb.90.054425.

[35] C. Kooy and U. Enz. "Experimental and theoretical study of the domain configuration in thin layers of BaFe12O19". *Philips Reasearch Reports*, **15**, pp. 7–29, 1960.

[36] Y. Murayama. "Micromagnetics on Stripe Domain Films. I. Critical Cases". *Journal of the Physical Society of Japan*, **21**(11), pp. 2253–2266, 1966. DOI: 10.1143/jpsj.21.2253.

[37] L. Fallarino, O. Hovorka, and A. Berger. "Field orientation dependence of magnetization reversal in thin films with perpendicular magnetic anisotropy". *Physical Review B*, **94**(6), 2016. DOI: 10.1103/physrevb.94.064408.

[38] J. Leliaert, B. Van de Wiele, A. Vansteenkiste, L. Laurson, G. Durin, L. Dupré, and B. Van Waeyenberge. "Current-driven domain wall mobility in polycrystalline Permalloy nanowires: A numerical study". *Journal of Applied Physics*, **115**(23), p. 233903, 2014. DOI: 10.1063/1.4883297.

[39] J.W. Lau, R.D. McMichael, and M.J. Donahue. "Implementation of Two-Dimensional Polycrystalline Grains in Object Oriented Micromagnetic Framework". *Journal of Research of the National Institute of Standards and Technology*, **114**(1), p. 57, 2009. DOI: 10.6028/jres.114.005.

[40] S. Disch, E. Wetterskog, R. P. Hermann, G. Salazar-Alvarez, P. Busch, T. Brückel, L. Bergström, and S. Kamali. "Shape Induced Symmetry in Self-Assembled Mesocrystals of Iron Oxide Nanocubes". *Nano Letters*, **11**, pp. 1651–1656, 2011. DOI: 10.1021/nl200126v.

[41] S. V. Maleyev. "Investigation of Spin Chirality by Polarized Neutrons". *Physical Review Letters*, **75**(25), pp. 4682–4685, 1995. DOI: 10.1103/physrevlett.75.4682.

[42] S. V. Grigoriev, Yu. O. Chetverikov, D. Lott, and A. Schreyer. "Field Induced Chirality in the Helix Structure Dy/Y Multilayer Films and Experimental Evidence for Dzyaloshinskii-Moriya Interaction on the Interfaces". *Physical Review Letters*, **100**(19), 2008. DOI: 10.1103/physrevlett.100.197203.

[43] D. Korolkov, P. Busch, L. Willner, E. Kentzinger, U. Rücker, A. Paul, H. Frielinghaus, and T. Brückel. "Analysis of randomly oriented structures by grazing-incidence small-angle neutron scattering". *Journal of Applied Crystallography*, **45**(2), pp. 245–254, 2012. DOI: 10.1107/s0021889812002324.

[44] S. Mühlbauer, D. Honecker, É. A. Périgo, F. Bergner, S. Disch, A. Heinemann, S. Erokhin, D. Berkov, C. Leighton, M. R. Eskildsen, and A. Michels. "Magnetic small-angle neutron scattering". *Reviews of Modern Physics*, **91**(1), 2019. DOI: 10.1103/revmodphys.91.015004.

[45] S. D. Pollard, J. A. Garlow, K.-W. Kim, S. Cheng, K. Cai, Y. Zhu, and H. Yang. "Bloch Chirality Induced by an Interlayer Dzyaloshinskii-Moriya Interaction in Ferromagnetic Multilayers". *Physical Review Letters*, **125**(22), 2020. DOI: 10.1103/physrevlett.125.227203.

[46] S. Rohart and A. Thiaville. "Skyrmion confinement in ultrathin film nanostructures in the presence of Dzyaloshinskii-Moriya interaction". *Physical Review B*, **88**(18), 2013. DOI: 10.1103/physrevb.88.184422.

[47] D.-H. Kim, M. Haruta, H.-W. Ko, G. Go, H.-J. Park, T. Nishimura, D.-Y. Kim, T. Okuno, Y. Hirata, Y. Futakawa, H. Yoshikawa, W. Ham, S. Kim, H. Kurata, A. Tsukamoto, Y. Shiota, T. Moriyama, S.-B. Choe, K.-J. Lee, and T. Ono. "Bulk Dzyaloshinskii–Moriya interaction in amorphous ferrimagnetic alloys". *Nature Materials*, **18**(7), pp. 685–690, 2019. DOI: 10.1038/s41563-019-0380-x.

[48] E. Kentzinger, U. Rücker, B. Toperverg, F. Ott, and T. Brückel. "Depth-resolved investigation of the lateral magnetic correlations in a gradient nanocrystalline multilayer". *Physical Review B*, **77**(10), 2008. DOI: 10.1103/physrevb.77.104435.

[49] G. Pospelov, W. Van Herck, J. Burle, J. M. Carmona Loaiza, C. Durniak, J. M. Fisher, M. Ganeva, D. Yurov, and J. Wuttke. "BornAgain: software for simulating and fitting grazing-incidence small-angle scattering". *Journal of Applied Crystallography*, **53**(1), pp. 262–276, 2020. DOI: 10.1107/s1600576719016789.

Acronyms

AFM Atomic Force Microscopy.

CCW Counterclockwise.

CGS Centimeter-Gram-Second System of Units.

CPU Central Processing Unit.

CW Clockwise.

DMI Dzyaloshinskii–Moriya Interaction.

DW Domain Wall.

DWBA Distorted Wave Born Approximation.

DWMR Domain-Wall Magnetoresistance.

EBV Electron Beam Evaporator.

FCC Face-Centered Cubic.

FT Fourier Transform.

GISANS Grazing-Incidence Small-Angle Neutron Scattering.

GISAXS Grazing-Incidence Small-Angle X-ray Scattering.

GMR Giant Magnetoresistance.

GPU Graphics Processing Unit.

HDD Hard Disk Drive.

IP In-Plane.

JCNS-2 Jülich Center for Neutron Science 2.

JSC Jülich Supercomputing Center.

JUSUF Jülich Support for Fenix.

JUWELS Jülich Wizard for European Leadership Science.

LLG Landau-Lifshitz-Gilbert.

MBE Molecular Beam Epitaxy.

MFM Magnetic Force Microscopy.

MRAM Magnetoresistive Random Access Memory.

MSANS Magnetic Small-Angle Neutron Scattering.

MTJ Magnetic Tunnel Junction.

NIST National Institute of Standards and Technology.

NSF Non-Spin-Flip.

OOP Out-Of-Plane.

PMA Perpendicular Magnetic Anisotropy.

SF Spin-Flip.

SFS Spin-Flip Splitting.

SI International System of Units.

SWM Sinewave Wall Model.

TMR Tunneling Magnetoresistance.

List of Symbols

Symbol	Name	Units
a, b, c	Lattice parameters of the unit cell	m
α	LLG damping coefficient	–
α	Tilt angle of the polarization axis	–
α_i	Incident neutron angle	–
α_f, θ	Scattered neutron angles	–
A	Exchange stiffness	$\mathrm{J\,m^{-1}}$
$\mathbf{B}$	Magnetic flux density	T
$\mathbf{c}$	Chirality vector	$\mathrm{m^{-1}}$
C	Asymmetry factor of the SF peaks	–
γ_0	Gyromagnetic ratio	$\mathrm{T^{-1}\,s^{-1}}$
$\mathbf{\Gamma}$	Torque	$\mathrm{N\,m}$
d	Film thickness	m
d_c	Critical thickness	m
$d_{\mathrm{c},1}$	First critical thickness	m
$d_{\mathrm{c},2}$	Second critical thickness	m
δ_B	Width of the Bloch wall	m
δ_N	Width of the Néel closure domain	m
δ_w	Bloch wall characteristic width	m
$\Delta x, \Delta y, \Delta z$	Cell size in the x, y and z-directions	m
$\mathbf{D}$	Electric displacement	$\mathrm{C\,m^{-2}}$
D_bulk	Bulk DMI strength	$\mathrm{J\,m^{-2}}$
D_holes	Diameter of the holes	m
$\mathbf{D}_{ij}$	DMI vector for lattice sites i and j	J

Symbol	Name	Units
D_{ind}	Interfacially-induced DMI strength	$\mathrm{J\,m^{-2}}$
$\mathbf{D}_i^{x,y,z}$	Interfacially-induced DMI vector for layer i	$\mathrm{J\,m^{-1}}$
$\frac{\mathrm{d}\Sigma}{\mathrm{d}\Omega}$, $\frac{\mathrm{d}\Sigma^{\pm\pm}}{\mathrm{d}\Omega}$, $\frac{\mathrm{d}\Sigma^{\pm\mp}}{\mathrm{d}\Omega}$	Scattering cross sections	$\mathrm{m^2}$
e	Volume energy density	$\mathrm{J\,m^{-3}}$
e^{ip}	Volume energy density in the IP saturated state	$\mathrm{J\,m^{-3}}$
e^{oop}	Volume energy density in the OOP saturated state	$\mathrm{J\,m^{-3}}$
$e_{\mathrm{DMI,ind,MuMax}}$	Interfacially-induced DMI energy density in *MuMax3*	$\mathrm{J\,m^{-3}}$
$e_{\mathrm{DMI,bulk,MuMax}}$	Bulk DMI energy density in *MuMax3*	$\mathrm{J\,m^{-3}}$
$\mathbf{e}_{\mathrm{n}}$	Outside normal	–
$\mathbf{e}_{\mathrm{u}}$	Easy magnetization axis	–
η	Angle between the easy axis and the z-axis	–
$\mathbf{E}$	Electric field	$\mathrm{V\,m^{-1}}$
E_{a}	Magnetocrystalline anisotropy energy	J
E_{d}	Demagnetizing energy	J
$E_{\mathrm{DMI,ind}}$	Interfacially-induced DMI energy	J
E_{ex}	Exchange energy	J
E_{tot}	Total micromagnetic energy	J
E_{Z}	Zeeman energy	J
$\mathbf{H}$	Magnetic field	$\mathrm{A\,m^{-1}}$
$\mathbf{H}_0$	Guide field	$\mathrm{A\,m^{-1}}$
H_{c}	Coercivity	$\mathrm{A\,m^{-1}}$
$\mathbf{H}_{\mathrm{c}}$	Current contribution to $\mathbf{H}$	$\mathrm{A\,m^{-1}}$
$\mathbf{H}_{\mathrm{d}}$	Demagnetizing field	$\mathrm{A\,m^{-1}}$
$\mathbf{H}_{\mathrm{eff}}$	Effective field	$\mathrm{A\,m^{-1}}$
$\mathbf{H}_{\mathrm{ext}}$	External applied magnetic field	$\mathrm{A\,m^{-1}}$
$\mathbf{H}_{\mathrm{m}}$	Magnetization contribution to $\mathbf{H}$	$\mathrm{A\,m^{-1}}$
H_{n}	Nucleation field	$\mathrm{A\,m^{-1}}$
$\mathbf{I}$	Identity tensor	–
I_1, I_2	Intensities of the 2 SF peaks	a.u.
$\mathbf{j}$	Current density	$\mathrm{A\,m^{-2}}$

Symbol	Name	Units
J_{ij}	Exchange integral between lattice sites i and j	J
$\mathbf{k}_f$	Scattered neutron wavevector	m^{-1}
$\mathbf{k}_i$	Incident neutron wavevector	m^{-1}
K_u	Anisotropy constant	$\mathrm{J\,m}^{-3}$
$l_{\mathrm{ex},K}$	Magnetocrystalline exchange length	m
$l_{\mathrm{ex},M_\mathrm{s}}$	Magnetostatic exchange length	m
$\mathbf{m}$	Unit magnetization vector	–
μ	Magnetic moment	$\mathrm{A\,m}^2$
μ_0	Vacuum permeability	$4\pi\ 10^{-7}\ \mathrm{T\,m\,A}^{-1}$
$\mathbf{M}$	Magnetization	$\mathrm{A\,m}^{-1}$
$\tilde{\mathbf{M}}$	Fourier transform of $\mathbf{M}$	$\mathrm{A\,m}^2$
M_r	Remanent magnetization	$\mathrm{A\,m}^{-1}$
M_s	Saturation magnetization	$\mathrm{A\,m}^{-1}$
$\mathbf{M}^{\parallel}$	Magnetization parallel to the guide field	$\mathrm{A\,m}^{-1}$
$\mathbf{M}^{\perp}$	Magnetization perpendicular to the guide field	$\mathrm{A\,m}^{-1}$
N	Ratio of irradiated sample to coherence volume	–
n_holes	Number of holes in the simulation box	–
n_L	Left-handed domain walls population number	–
n_R	Right-handed domain walls population number	–
N_x, N_y, N_z	Number of cells in the x, y and z-directions	–
$\boldsymbol{\mathcal{N}}$	Demagnetizing tensor	–
p	Helicity	m^{-1}
P	Domain period	m
$\mathbf{P}$	Polarization axis	–
$\mathbf{q}$	Scattering vector	m^{-1}
$\hat{\mathbf{q}}$	Unit scattering vector	–
Q	Anisotropy quality factor	–
$\mathbf{Q}$	Magnetic-interaction vector	$\mathrm{A\,m}^2$
$\mathbf{r}$	Position vector	m
r_g	Grain size	m

Symbol	Name	Units
ρ_f	Free electric charge density	$\mathrm{C\,m^{-3}}$
ρ_m	Volume magnetic charge density	$\mathrm{A\,m^{-2}}$
R	Area between IP and OOP magnetization curves	$\mathrm{J\,m^{-3}}$
s	Spin number	–
$\mathbf{S}$	Spin	–
$\sigma_{\mathbf{e}_\mathrm{u}}$	Standard deviation of η	–
σ_{K_u}	Relative standard deviation of K_u	–
σ_m	Surface magnetic charge density	$\mathrm{A\,m^{-1}}$
σ_rms	Root mean square surface roughness	m
σ_w	Bloch wall energy per unit area	$\mathrm{J\,m^{-2}}$
t	Time	s
t_B	Height of the Bloch wall	m
t_FM	Magnetic layer thickness	m
t_NM	Non-magnetic layer thickness	m
θ, ϕ, γ	Angles to describe a domain wall	–
θ	Angle between $\mathbf{q}$ and the z' axis	–
T	Temperature	K
T_s	Substrate temperature	K
T_C	Curie temperature	K
$\mathbf{u}_{12}$	Vector between lattice sites 1 and 2	m
V	Volume	$\mathrm{m^3}$
w	Domain width	m
W	Width of the simulation box	m
$\hat{\mathbf{x}}, \hat{\mathbf{y}}, \hat{\mathbf{z}}$	Basis vectors of the (x, y, z) coordinate system	–
$\hat{\mathbf{X}}, \hat{\mathbf{Y}}, \hat{\mathbf{Z}}$	Basis vectors of the (X, Y, Z) coordinate system	–
$\hat{\mathbf{x}}', \hat{\mathbf{y}}', \hat{\mathbf{z}}'$	Basis vectors of the (x', y', z') coordinate system	–

List of Figures

List of Tables